Northumbria Research Link

Northumbria Research Link

Retinal Image Analysis for Eye Disease Detection and Classification

Mohamed Albashir Omar

A thesis submitted in partial fulfilment of the requirements of the University of Northumbria at Newcastle for the degree of Doctor of Philosophy

Research undertaken in the Faculty of Engineering and Environment

September 2018

ABSTRACT

Diabetes is a chronic disease affecting over 2% of the population in the UK (Shaw et al., 2010). Diabetes of all types can lead to complications in many parts of the body, including the retina of the eye where it can lead to vision loss. In the retina, diabetes can lead to diseases called diabetic retinopathy (DR), diabetic macular edema (DME) and age-related macular degeneration (AMD) which are among the major causes of blindness in the working population of industrialised countries. Fortunately, diagnosing it in its early stages is useful for effective treatment and it is usually treatable. DR or DME are mainly characterised by red spots, namely microaneurysms and bright lesions, specifically exudates, whereas AMD is mostly identified by white or tiny yellow deposits known as drusen lesion. Since exudates might be the only early signs of DR, there is an increased demand for automatic DR diagnosis. Exudates and drusen may share a similar appearance; hence discriminating between them is of interest in enhancing diagnostic performance. However, due to the increased demand for automatic diagnosis from retinal lesion images, computerized systems have nowadays become essential. Although the process of diagnosis and decision-making is challenging for ophthalmologists when analysing retinal lesion images, it needs to be time-efficient. This thesis is concerned with an investigation of novel image processing techniques in the diagnosis of diabetes with different types of diseases such as DR, DME and AMD. The thesis focuses on feature extraction in image processing and proposes diagnostic techniques based on state-of-the-art technology. The first contribution of the thesis is the use of a new LBP-based feature extraction technique after dividing the image into number of patches instead of using the whole image in the analysis. The extracted features have been applied with both the radial basis function neural network (RBF-ANN) and k-nearest neighbour (k-NN) classifiers for training and testing purposes. The second contribution involves a novel technique used to propose a multi-label machine learning model for classification problem combining the diagnosis of diabetic macular edema (DME) with other factors such as patient age and LBP-based feature extraction being applied for classification. The third and main contribution of this thesis is to demonstrate that colour vector angles (CVAs) and local binary patterns (LBPs) are more suitable for the analysis and classification of retinal images and their use leads to high classification performance as compared to other textural and colour features. A codebook is generated using a bagged combination of local

binary pattern (LBPs) and colour vector angles (CVAs) features to exploit colour and textural information.

The overall system has been assessed through intensive experiments using different classifiers with a dataset of 352 retinal images collected from various datasets, namely: DIARETDB0 (Kauppi et al., 2006), DIARETDB1 (Kälviäinen and Uusitalo, 2007), HEI-MED (Giancardo et al., 2012), STARE (Hoover and Goldbaum, 2003), and MESSIDOR (Decencière et al., 2014). Correct classification is reported with an average sensitivity of 99.51%, specificity of 99.60% and accuracy of 99.63% and an overall average area under the curve of 98.59%. This represents the best performance achieved so far when compared to existing state-of-the-art systems for the diagnosis of retinal lesions.

DECLARATION

I declare that the work contained in this thesis has not been submitted for any other award
and that it is all my own work. I also confirm that this work fully acknowledges opinions,
ideas and contributions from the work of others.

Name: Mohamed Albashir Omar.

Signature:

Date: 12/09/2018

ACKNOWLEDGEMENTS

CONTENTS

LIST OF TABLES

LIST OF FIGURES

LIST OF ABBREVIATIONS AND ACRONYMS

Acc	Accuracy
AUC	Area Under the Curve
ANN	Artificial Neural Networks
AMD	Age-related Macular Degeneration
BoF	Bag of Features
CAD	Computer Aided Detection
CHD	Coronary Heart Disease
CVA	Colour Vector Angle
DM	Diabetes Mellitus
DME	Diabetic Macular Edema
DR	Diabetic Retinopathy
ELVD	Elliptical Local Vessel Density
FCM	Fuzzy C-Means
FN	False Negative
FoV	Field of View
FP	False Positive
LBP	Local Binary Patterns
MLL	Multi-Label Learning
NPDR	Non-proliferative Diabetic Retinopathy
OCT	Optical Coherence Tomography
OD	Optic Disc
PDR	Proliferative Retinopathy
ROI	Region of Interest

RI	Rotation Invariant
SE	Structural Element
Sen	Sensitivity
Spec	Specificity
TCM	Traditional Chinese Medicine
TN	True Negative
TP	True Positive

1. INTRODUCTION

Medical diagnostic imaging has existed since the first decade of the 1900s after the discovery of X-rays and new image modalities including ultrasound and magnetic resonance imaging (MRI) have combined to an explosion of research into medical image analysis (Doi, 2007). In medical imaging an accurate diagnosis is dependent on two factors. The first factor is the successful acquisition of the image; the second factor is the successful interpretation of the image. Diagnostic imaging has enabled the non-invasive visualisation of a variety of biological systems, such as the brain, heart, lungs and eyes. Medical diagnosis based on images obtained by ultrasound, computer tomography (CT), digital x-rays and digital fundus cameras (see Figure 1.1) is now commonplace and has significantly improved the medical care available to patients. With increased medical imaging capabilities, screening programs for the early detection of harmful lesions from diseases such as diabetes have also been applied nationwide.

Figure 1.1. Canon CR6-45NM retinal camera with digital camera upgrade installed (Cheng et al., 2017)

CHAPTER 1: INTRODUCTION

As indicated by the World Health Organization (WHO), diabetes mellitus (DM) is a lifelong disorder, which develops when the pancreas does not produce sufficient insulin (type 1 diabetes) or when the body cannot adequately benefit from the insulin, it produces (type 2 diabetes). Insulin is a hormone produced in the pancreas by beta cells that controls blood levels of glucose. Increased levels of sugar causes serious harm to the body's systems, including diabetic retinopathy. The most significant reasons for the spread of diabetes are increasing rates of obesity, ageing, and sedentary way of life. During the first two decades of the disease, many patients with type 1 diabetes and over 60% of those with type 2 diabetes develop retinopathy (Fong et al., 2004). The predominance of diabetes is predicted to increase from 2.8% to 4.4% in the period between $2000 - 2030$. The total number of individual cases is anticipated to increase from 171 million in 2000 to 360 million in 2030 (Organization, 2016). Severe visual loss in diabetic patients can be prevented by their attendance or regular diabetic eye screening programme and better treatment (Yen and Leong, 2008).

Diabetic retinopathy (DR), diabetic macular edema (DME) and age-related macular degeneration (AMD) are among the leading causes of visual impairment worldwide. DR and DME occur most frequently in adults aged $20 - 74$ years, and is characterised by the existence of red lesions (microaneurysms) and bright lesions (exudates) which appear as small white or yellowish white deposits with sharp margins and variable shapes located in the outer layer of the retina. Their detection is essential for DR and DME screening systems.
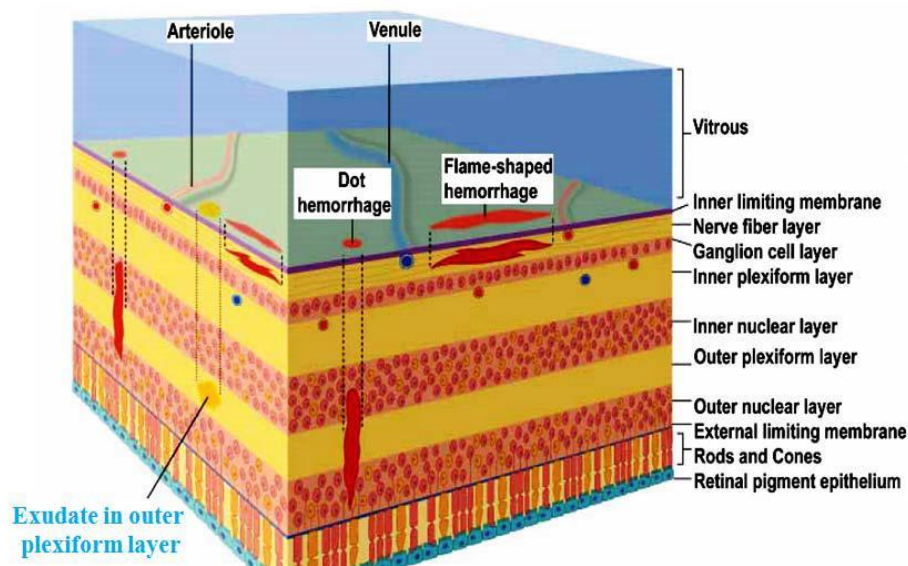
Figure 1.2. An example of exudate in the outer layer of the retina (Yen and Leong, 2008).

AMD generally affects people over 50 years of age. It is caused by damage to the macula, which is the small sensitive area of the retina that provides central vision, which called drusen, whichever tiny yellow or white deposits in the layer of the retina called Bruch's membrane. The severity of AMD can be characterised in early, intermediate, and advanced stages as discussed in chapter 2. Two examples of an exudate and drusen in a human retina are shown in Figure 1.2 and Figure 1.3 respectively.

For some patients, bright lesions such as retinal exudates can be the only appearance of early DR. Thus, computer-aided detection (CAD) systems have been proposed in order to detect exudates. However, these bright lesions must be distinguished from drusen because they are shared with common characteristics (Niemeijer et al., 2007b). This represents a challenge or CAD-based screening systems designed for DR, DME or AMD diagnosis. Consequently, developing a CAD system for the analysis of retinal images and can reduce the false negative rates which may occur when ophthalmologists usually interpret these images.
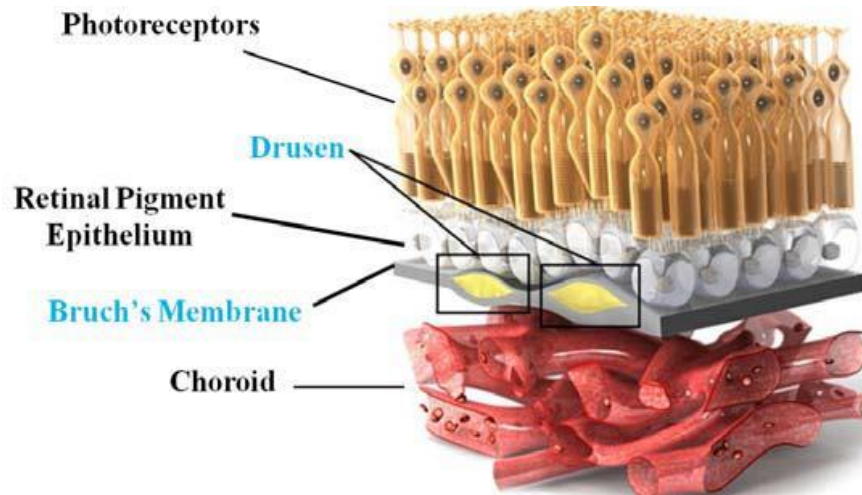
Figure 1.3. An example of drusen within Bruch's membrane (Klein et al., 2005).

Therefore, a computer-aided diagnosis system for the early detection of lesions in retinal images is nowadays thought to be essential. Several researchers have proposed such systems using image processing and classification techniques to diagnose DR, DME or AMD using retinoscopy images in order to support the decisions of ophthalmologist. In general, image processing techniques are used to segment the region of interest (lesion), and then image features are extracted to train a classifier. These features can be categorised as texture and colour features.

Features that represent the spatial organization of intensity in an image, such as local binary patterns, granulometry and streaks, can be characterised as textural features, whereas colour features describe the distribution of colour in the image of the retina (Aly et al., 2009, Garcia et al., 2014).

1.1 Reasons for Retinal Image Diagnosis

DR is a common complication of diabetes and a leading cause of blindness and visual loss. After 15 years of diabetes, over 95% of type 1 and 77% of type 2 patients develop retinopathy (Klein et al., 1984a, 1984b). The severity of the retinopathy varies with the age of onset, disease duration and the blood glucose control. Therefore, an approximately 2% of patients become blind and 10% will be severely visually handicapped (Organization, 2004).

Though, most existing algorithms in this field are designed to detect a specific type of lesion in retinal images, although different lesions might be present in a single image

indicating the stage of the disease. Moreover, lesions can appear to be very similar while in fact being signs of different diseases. For instance, DR and DME are characterised in the early stages by red lesions (microaneurysms) and bright lesions (exudates) which appear as small white or yellowish deposits with sharp edges in retinal images. On the other hand, variably sized yellowish deposits in the retina, called drusens mainly characterize age-related macular degeneration (AMD) which causes a gradual loss of central vision. Therefore, discriminating between different types of lesions is of great importance for decision making in an automatic CAD system. Fortunately early diagnosis and timely treatment have been shown to prevent visual loss and blindness in patients with diabetes (Group, 1991, Bresnick et al., 2000). For a better understanding of the structure of the eye, it is essential to know more about diseases of the human eye. Information related to eye disease is discussed in the next chapter.

1.2 Aims and Objectives

The aim of this work is to develop a set of tools for screening the retinas of diabetes patients using colour fundus images. During the present research, four objectives were set:

1. To investigate existing state-of-the-art image processing techniques and to critically evaluate their performance in distinguishing different types of retinal lesions.

2. To propose efficient systems to support decision making that automatically diagnose retinal lesions, and to exploit image analysis tools and methods to provide high efficiency.

3. To evaluate the efficiency of the proposed systems by comparing the results obtained with those of previous studies.

4. To propose a multi-label model for multiple labels such as DME disease diagnosis and patient age.

5. To disseminate the study's findings in relevant refereed conferences and journals and to write up a PhD thesis.

1.3 Scope of Research and Timeliness of Research Topic

The present research uses efficient image processing algorithms and classification techniques related to the detection of retinal lesions in order to achieve the effective diagnosis of retinal disease in its early stages, to ensure high accuracy and to support decision making and to counter the rapidly increasing incidence rate of this type of disease.

1.4 Contributions of the Thesis

In this work, several techniques are proposed for the automated detection of lesions in retinal images in order to improve the accuracy of the early diagnosis of DR, DME and AMD. The main contributions of this thesis can be summarised as follows:

1. Retinal segmented images are classified as abnormal or normal by extracting region-based textural characteristics. Then, multi-scale local binary patterns (LBPs) are adopted for textural feature extraction within the region of interest (ROI) of colour retinal images.

2. A multi-label learning model (ML-kNN) is proposed for DME disease and patient age to achieve DR diagnosis from retinal image.

3. An automatic approach for the detection and classification of lesions in retinal images is proposed that discriminates between images containing different bright lesions using bagged colour vector angles to exploit the colour information concatenated with local binary patterns as textural features, and a codebook is generated.

1.5 Thesis Structure

This thesis is structured as follows:

Chapter 1 introduces medical diagnostic imaging and DR, DME and AMD diseases.

Chapter 2 then provides the medical background of the human eye, its structure, and explains state-of-the-art systems for the analysis of retinal lesions and abnormalities.

Chapter 3 is devoted to an overview of the latest state-of-the-art imaging techniques used in the computerized analysis of retinal images, and in chapter 4 the proposed automated

system of the detection and classification of exudates in retinal fundus images is discussed using a region-based multi-scale LBP texture method.

In chapter 5, a multi-label learning algorithm (ML-kNN) is applied to construct an automatic model for the classification of lesions for the purpose of diagnosis of DR from retinal images. This extends previous work concerned with disease classification from two-class problem to a multi-label learning classification problem by combining the detection of the diabetic macular edema (DME) with other factors such as patient age.

Chapter 6 then describes a new automatic retinal diagnostic system that combines colour vector angles used as colour features with LBP textural features. The superiority of the proposed system is demonstrated with five different datasets, namely the DIARETDB0, DIARETDB1, HEI-MED, STARE and MESSIDOR datasets, for the efficient and accurate detection of the retinal lesion.

Finally, chapter 7 provides the conclusions of the study and suggests future research directions in the light of the obtained results.

2. MEDICAL BACKGROUND ON THE STRUCTURE OF THE EYE AND STATE-OF-THE-ART RETINAL ANALYSIS

2.1 Introduction

This chapter introduces the medical background and the state-of-the-art retinal image techniques in order to explain the significance of fundus image analysis in diabetic retinopathy (DR) and age-related macular degeneration (AMD). Medical image processing has recently altercated notable attention within the research community. Due to the non-invasive nature of techniques, the analysis of medical images represents an excellent option in achieving the diagnosis and control of diseases. With the availability of new methods to acquire medical images and the creation of new techniques to process them, the analysis of medical images has revolutionised the field of medicine.

Diabetes is a chronic disease affecting over 2% of the population in the UK (Shaw et al. (2010). Diabetes can manifest itself in different systems in the body, causing long-term complications to the heart, kidneys, nerves, blood vessels and eyes. In the eye, diabetes can affect various ocular structures such as the lens and the retina. In the retina, diabetes can lead to an eye disease called diabetic retinopathy, which has been recognised as one of the principal causes of vision loss in the working populations of developed countries. People with diabetes are 29 times more likely to become blind compared to those who do not have the disease (Control and Prevention, 2011b).

As the initial phase of the disease is typically asymptomatic, individuals are not usually conscious of the risk of developing sight-threatening retinopathy and, as a result, vision loss, until it is too late. It is therefore crucial that regular retinal examinations are carried out in order to detect the initial onset of the disease before noticeable visual loss occurs.

Early treatment by laser photocoagulation has been shown to significantly reduce the incidence of visual loss (Ding and Wong, 2012). Diabetic retinopathy can be detected by either clinical examination using different methods, such as direct ophthalmoscopy, indirect ophthalmoscopy and biomicroscopy, or retinal photography using instant fundus Polaroid photographs, colour fundus 35-mm slides or digital imaging. The UK National

CHAPTER 2: MEDICAL BACKGROUND ON THE STRUCTURE OF THE EYE AND
STATE-OF-THE-ART RETINAL ANALYSIS

Screening Committee has suggested that annual screening by digital colour fundal photography is the preferred medium (Szabó et al., 2015). With 20,000 - 30,000 diabetic patients per million of the population, manual diagnosis from retinal images is a time-consuming and costly process requiring highly skilled staff, and is also susceptible to subjective variation and error (Bolster et al., 2016). Furthermore, age-related macular degeneration (AMD) is another retinal disease that is a leading cause of adult blindness in the UK (Nowozin et al., 2007). AMD typically affects persons who are aged 50 years and above. In 2020, it is expected that this age group will comprise a population at risk of 25 million people in the UK, and more than 7% of them will probably be affected (Nowozin et al., 2007). There are new treatments that may stem its onset if detected in the early stages (Loewenstein, 2007). At the moment, what causes AMD is unknown but it is conjectured to be related to risk factors such as older age, a history of smoking, the female gender, lighter pigmentation, a high-fat diet and a genetic component (Rapantzikos et al., 2003). The diagnosis of AMD is typically undertaken through the careful inspection of the macula by trained clinicians. In most cases, the first indicator of AMD is the presence of drusen, yellowish-white sub-retinal deposits, which are identified by examining the patient's retinal images.

This chapter begins with a brief description of the anatomy of the eye, followed by a discussion of the medical aspects of the retina. Lesions and abnormalities of the retina are then described, followed by diabetic eye diseases such as DR and AMD. Then, retinal imaging techniques are described.

2.2 Eye Anatomy

The camera is similar to the human eye and responsible for visible light detection in the part of the electromagnetic spectrum with wavelengths ranging between approximately 400 and 700 nm, as shown in Figure 2.1. The colour of visible light depends on its wavelength. For instance, violet and red have wavelength of 400 nm and 700 nm respectively (Endler, 1993).
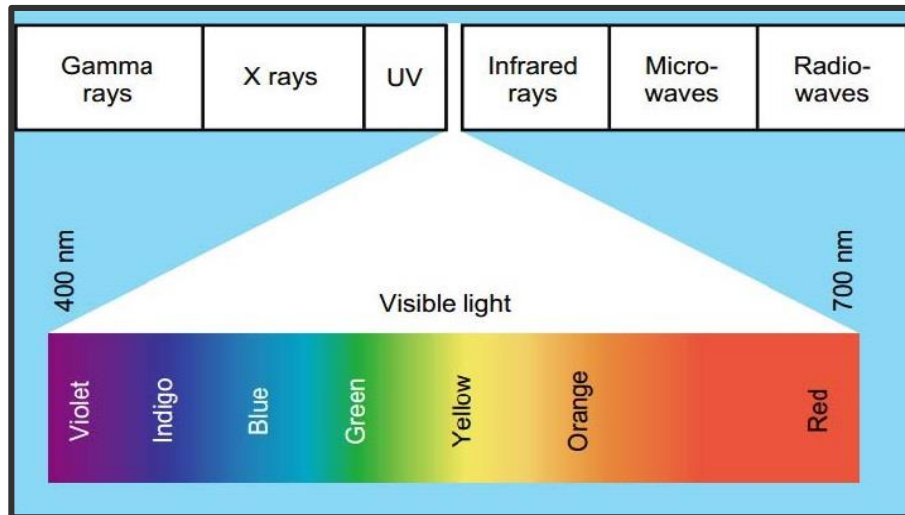
Figure 2.1. Electromagnetic spectrum (Tortora and Derrickson, 2008).

Most people would agree that vision is much more valuable than other senses present in our body, because we use our eyes in almost all daily activities we perform. The similarities between the human eye and the camera are striking. For instance, when we record an image using the eye, the camera and film are not used but the image is absorbed on to the retina.

In addition, the shutter in the camera and pupil at the centre of the iris alter the amount of light that is acquired over the lens (Smith, 1997).
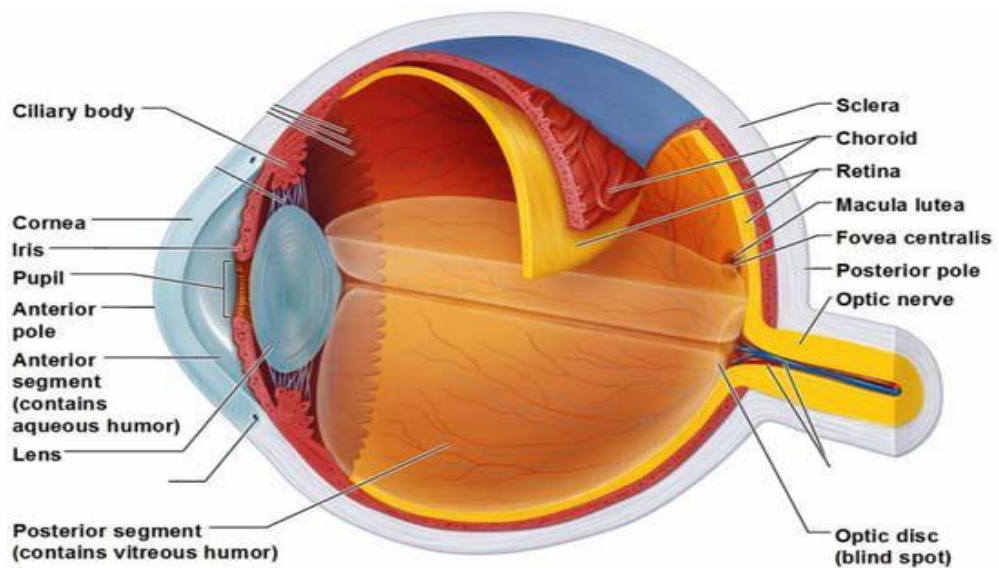
Figure 2.2. Cross-section of human eye anatomy (Sadek et al., 2015).

CHAPTER 2: MEDICAL BACKGROUND ON THE STRUCTURE OF THE EYE AND STATE-OF-THE-ART RETINAL ANALYSIS

Figure 2.2 shows the human eye's anatomy in cross-section. When light enters the eye, it initially strikes the cornea. The cornea refracts and filters the light, allowing the image to converge on the iris and pupil inside the eye. The iris will constrict or dilate to adjust the size of the pupil, and as a result, variable amounts of light may reach the eye. The shape of the lens can change due to the action of the auxiliary muscles to bring objects into focus. (Snell and Lemp, 2013). The structures of the retina is the most relevant in the present study compared to other ocular structures; hence, it is elaborated in depth in next section.

2.2.1 Retina

The retina is the innermost membrane that covers the interior surface of the eye. The lens and cornea focus light rays on to the retina. The lens and cornea behave like the lens of camera, while the retina is analogous to the picture. Thus, if the image is not focused accurately, the retina obtains blurred images. Usually, the retina consists of two main photoreceptors; rods and cones (Stein et al., 2012). Table 2.1 describes the different characteristics of rods and cones.

Table 2.1 Characteristics of cones and rods in the human retina.

Rods	Cones
Require a very low level of light to generate signals.	Require a higher level of light to generate signals.
Approximately 125 million photoreceptors.	Approximately 6 million photoreceptors.
Specialized for low light vision.	Mediate daylight and colour vision.
Distributed in the periphery of the retina.	Concentrated in the fovea, which lies in the macula at the centre.

The retina can be divided into many distinguishable layers as shown in Figure 2.3.

The retina's different layers are organized as follows (Snell and Lemp, 2013).

CHAPTER 2: MEDICAL BACKGROUND ON THE STRUCTURE OF THE EYE AND STATE-OF-THE-ART RETINAL ANALYSIS

1. Internal limiting membrane is at the border between the retina and vitreous body.

2. Ganglion cell layer cover the body of the ganglion cells.

3. Inner plexiform layer contains the axons of the amacrine and bipolar cells.

4. Inner nuclear layer contains the cell bodies of the bipolar and horizontal cells.

5. Outer plexiform layer (external plexiform layer) contains a layer of neuronal synapses in the retina and dendrites of the horizontal cells.
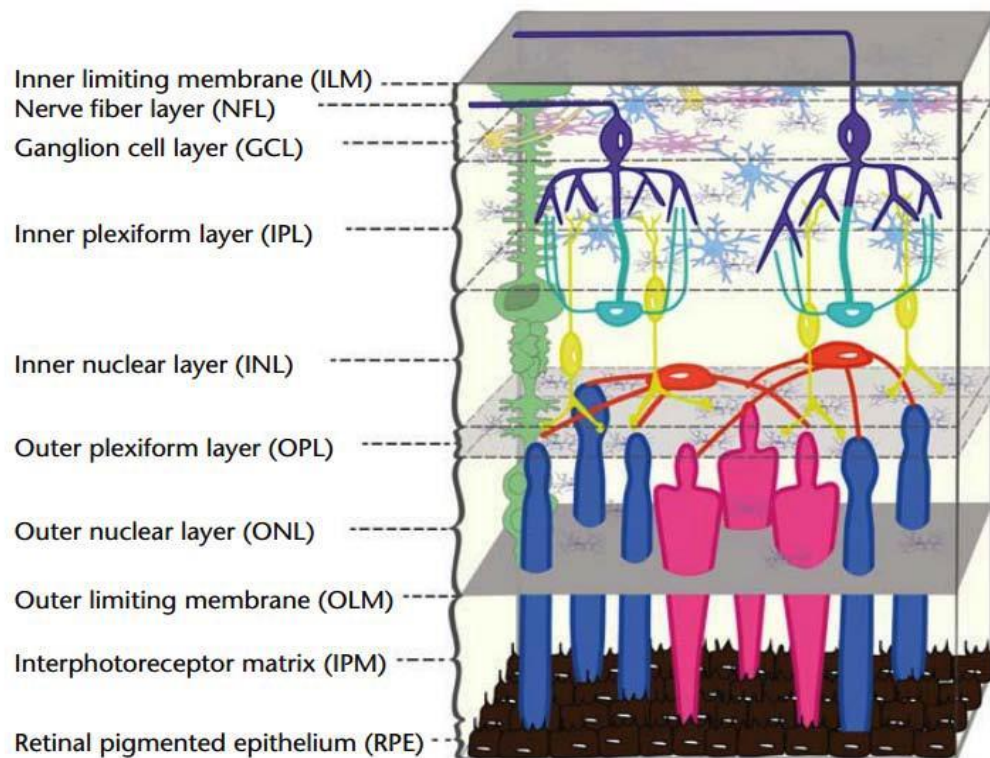
Figure 2.3. Schematic view of retina layers (Caprette et al., 2004).

6. Outer nuclear layer is the body of photoreceptor cells.

7. Outer limiting membrane (or external limiting membrane) is one of the ten separate layers of the retina.

8. Photoreceptor layer contains the inner and outer segments of cone and rod photoreceptors.

9. The pigment epithelium is the last layer of the retina that may contains various different pigments (colours). Thus, it protects the photoreceptors from damaging levels of light. The pigment epithelium cells provide nutritional substances such as glucose and essential ions to the photoreceptors as shown.

The ganglion cells are a type of neuron receiving visual information from photoreceptors through intermediate horizontal, and amacrine neurons. The horizontal cells are interconnecting neurons, which help to integrate and regulate the input from multiple photoreceptor cells.

2.2.2 Retina Lesions and Abnormalities

In this section, two groups of retinal lesions are discussed: yellow white spots, and red spots. The former include cotton wool spots, exudates, and drusen. The latter consist of microaneurysms and haemorrhages (Bucca, van Ginneken and Novak, 2012).
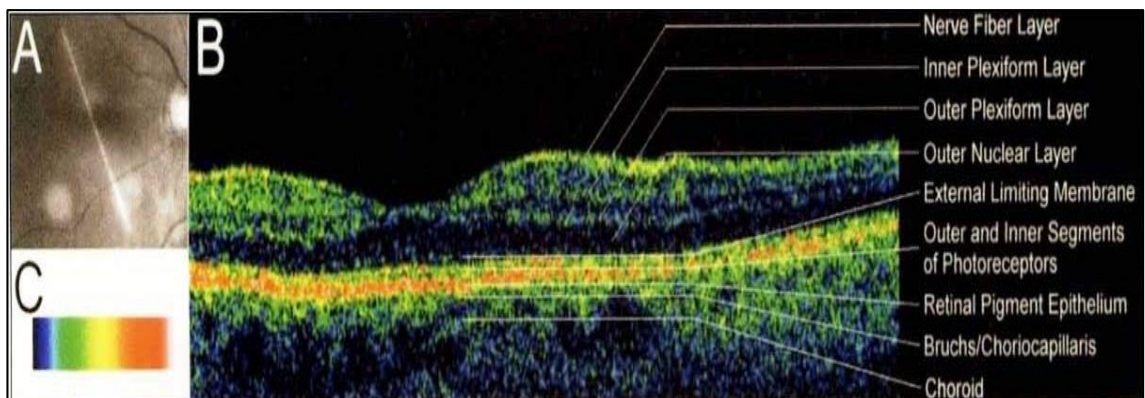
Figure 2.4. An optical coherence tomography (OCT) scan of a normal human macula (a) a frame captured at the start of the scan assists in location; (b) an OCT of the specified scan location; (c) colour map representing the log function of the reflectivity encountered by the probe beam (Broecker and Dunbar, 2005).

2.2.2.1   Cotton wool spots or soft exudates

Cotton wool spots or soft exudates appear as white, feathery spots with fuzzy borders. They physically correspond to small retinal closures (infarcts) and swellings of the retinal nerve fibre layer due to microvascular disease. They are located in the superficial inner retina, and so they may obscure nearby vessels. Figure 2.5(b) shows an example of such lesions.

2.2.2.2   Hard exudates

Hard exudates are lipoprotein and other kinds of protein originating from leaking microaneurysms. Hard exudates appear as small white or yellowish-white deposits with sharp edges, irregular shapes, and variable size as presented in Figure 2.5(c). The physical locations of these lesions are deeper in the retina than cotton wool spots.

2.2.2.3   Drusen

Drusen are variably sized yellowish lipoproteinaceous deposits that form between the Bruch membrane and retinal pigment epithelium (RPE). Usually, drusen alone do not contribute to vision loss. However, an increase in the size or number of such lesions are the earliest signs of age-related macular degeneration (AMD). Figure 2.5(d) shows an example.

2.2.2.4   Microaneurysms

Microaneurysms are among the earliest noticeable indications of retinal damage. They are round, small and dark red dots on the surface of the retina that have sharp margins. By definition, their sizes are less than the main optic veins as they cross the optic disc. They caused by the physical dilations (weakening) of the capillary walls, which stimulate leakages. Figure 2.5(e) shows examples of two microaneurysms lesions.

2.2.2.5   Hemorrhages

Hemorrhages happen due to leakage from weak capillaries leading to bleeding under the conjunctiva, which is the outermost protective layer of the eyeball. Generally, they may have several shapes such as dots, blots, and flames. Hemorrhages are described as red spots with uneven or indistinct edges and colouring. They are larger than microaneurysms; as shown in Figure 2.5(f).
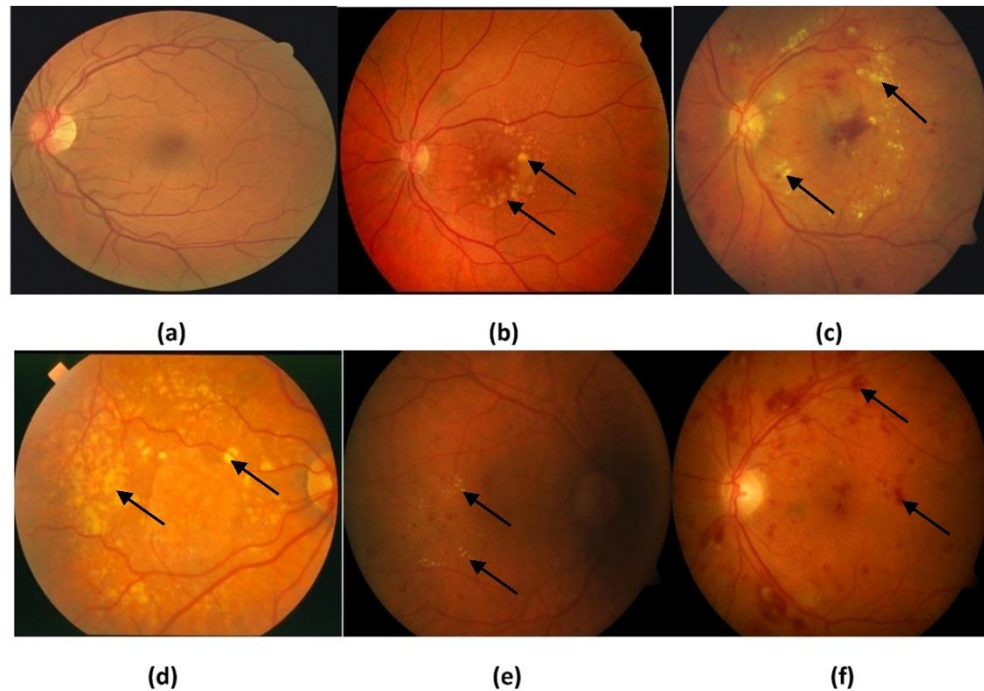
Figure 2.5. Typical fundus images: (a) normal; (b) soft exudates; (c) hard exudates; (d) drusen; (e) microaneurysms; and (f) hemorrhages.

2.3 Diabetic Eye Diseases

Diabetes mellitus (DM) is the most medically problematic form worldwide that can be identified as a chronic condition connected with the impaired metabolism of glucose because of insulin deficiency or resistance to it. Diabetes causes various difficulties that can affect the nervous system and eyes, kidneys, heart, blood vessels and other organs (Alghadyan, 2011).

Diabetes is the primary causes of vision loss in middle-aged adults between 20 to 74 years old. The US Center for Disease Control and Prevention (Control and Prevention, 2011b) indicates that 25.8 million people presently have DM in the United States. The World Diabetes Foundation reports also that over 439 million people will have diabetes by 2030 across the world (Mookiah et al., 2013). Diabetic macular edema and diabetic retinopathy are the most two well-known retinal diseases that are directly affected by diabetes.

2.3.1 Diabetic Retinopathy (DR)

DR is a microvascular problem that causes damage to the retina. DR is a leading effect of blindness in people with diabetes if not properly treated (Cade, 2008). Usually, it damages the retinas in both eyes. However, early diagnosis and proper treatment can minimize vision loss. Figure 2.6 (a) and (b) show two different scenes viewed by a normal person and a person suffering from diabetic retinopathy respectively. DR can be graded in four stages as follows (Csaky et al., 2017):

Figure 2.6. Scenes view types: (a) normal vision view; (b) scene viewed by a person with diabetic retinopathy (Ljubimov, 2017).

2.3.1.1   Mild Nonproliferative Retinopathy

The features of mild nonproliferative retinopathy are some of the earliest signs of diabetic retinopathy. At this point, microaneurysms occur along with hemorrhages and cotton wool spots. It is worth pointing out that not all patients will notice a change in their vision yet (Joussen et al., 2007).

2.3.1.2   Moderate Nonproliferative Retinopathy

As the disease processes, several more microaneurysms, hemorrhages, and cotton wool spots start to appear, In addition there is further damage to retinal blood vessels. Subsequently, the blood flow to the surrounding retinal tissue is reduced, giving rise to vision loss (Joussen et al., 2007).

2.3.1.3 Severe Nonproliferative Retinopathy

At this stage, large areas of the retina are deprived of blood flow. As a result, these regions of the retina send signals by means of vascular endothelial growth factor (VEGF) proteins in order to produce new neovascularization to enhance nourishment (Joussen et al., 2007).

2.3.1.4 Proliferative Retinopathy (PDR)

Proliferative retinopathy is the more advanced mode of diabetic retinopathy. At this point of disease progression, neovascularization starts to reach the vitreous humour, as the retina sends signal to the body for enhancements in nourishment. These new neovascularisations are fragile and abnormal and develop the retina. Nevertheless, their walls are fragile and thin, and whenever they leak blood severe blindness and even permanent vision loss can result (Joussen et al., 2007).

Based on the riskiness of the leakage, ophthalmologists grade the disease on scale from 1 to 4. Neovascularization can grow rapidly and remain relatively stable.

2.3.1.5 Diabetic Macular Edema

Diabetic macular edema (DME) corresponds to protein and fluid growth within the retina, specifically at the inner nuclear and outer plexiform layers, as a non-distinct response to the blood vessels of the retinal barriers. DME is a complication of DR. In DME, the macula swells with fluid leaked from the damaged blood vessels. DME is also the main reason for central blindness in patients with diabetes mellitus and following intraocular operations (Spaeth et al., 2011). According to Cohen and Gardner (2015) the DME occurs if one of the resulting conditions is fulfilled:

1. There exists swelling/thickening of the retina including the centre of the retina (macula) or the area within 500 µ of it.
2. Hard exudates are present at or within 500 µ of the centre of the retina with swelling next to the retina.
3. If there are areas or zones of retinal swelling/thickening 1 disk zone or bigger in size, and any such area is measured within 1 disk distance of the macula centre.

2.4 Age-related Macular Degeneration (AMD)

AMD is a common eye disease that generally afflicts elderly adult and causes vision loss in the macula owing to damage of the retina. A blurred zone near the macula is a frequent manifestation. In the long run, this blurred area may become larger, or blank spots may develop in central vision. AMD occurs in three different forms depending on the number and size of drusen under the retina.

1. Early AMD: Generally, people with early AMD do not experience vision loss, and medium-sized drusen are common signs.
2. Intermediate AMD: Intermediate AMD may cause some vision loss. Large drusen, pigment changes in the retina or both are typically found in people affected.
3. Late AMD: Late AMD has two forms: dry and wet AMD. The former (geographic atrophy), is progressive damage of the light-sensitive cells in the macula which may lead to central vision loss. The latter (neovascular) form is characterised by the growth of abnormal blood vessels underneath the retina that can leak fluid and blood, blurring or distorting central vision.

2.5 Retinal Imaging Techniques

Retinal imaging techniques are developed in order to capture images of the retina morphology effectively and to model changes over time. Fundus photography, optical coherence tomography (OCT) and fluorescein angiography are retinal imaging techniques that are widely used for the detection of diabetic retinopathy (Lavinsky et al., 2017).

2.5.1 Retinal Imaging Tools and Acquisition

Retinal images are acquired by a highly specialized camera called the fundus camera. In fact, retinal images play an important role in diagnosing several eye disease; for instance, diabetic retinopathy (DR) and age-related macular degeneration (AMD). For many years in ophthalmoscopy, fundus photography, fluorescein angiography, and diagnostic ultrasound have been considered the only retinal imaging modalities.

CHAPTER 2: MEDICAL BACKGROUND ON THE STRUCTURE OF THE EYE AND STATE-OF-THE-ART RETINAL ANALYSIS

Recently, different techniques have been introduced, including indocyanine angiography, scanning laser ophthalmoscopy (SLO), optical coherence tomography (OCT), and infrared imaging. Additionally, digital technology permits easy data processing and storage as well as enabling the exchange of images worldwide (Heimann et al., 2006).
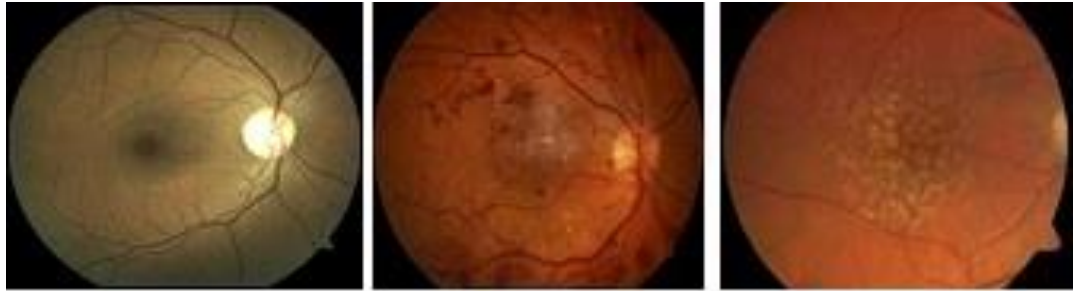
Figure 2.7. Examples of retinal images: (a) healthy; (b) diabetic retinopathy; (c) age-related macular degeneration

Typically, ophthalmoscopy, or fundoscopy, is used to determine the health status of retina and vitreous humor. There are two forms of ophthalmoscope: direct and indirect. The first type is a measurement device the size of a minor flashlight with several lenses that have an amplification up to 15 periods. The second type is provided with a light attached to a head, which can provide a wider view of the inside of the eye. Fundus photography is frequently used to create a picture of the eye's internal surface, involving the retinal, macula, and optic disc, through the dilated pupil of the patient to enhance image quality. It helps transfer images via networks for remote viewing by specialists or trained medical professionals. In addition, it allows for large-scale screening programme, which are a key tool in preventing diabetic retinopathy and deterioration in induced vision that can lead to blindness.

Usually, the fundus camera is a low-slung effect optical microscope with camera attached, which provides an upright magnified fundus view. A fundus with an angle of 30° is considered the typical view angle, creating $2.5x$ magnification. A fundus camera with a wide-angle lens can capture images from 45° to 140° and deliver a smaller degree of magnification. Meanwhile, narrower angle fundus cameras have viewing angles of 20° or less (Saine and Tyler, 2002). Figure 2.7 shows different examples of retinal fundus

images. Figure 2.8 shows an OCT scan containing different colour-coded layers of the
retina.
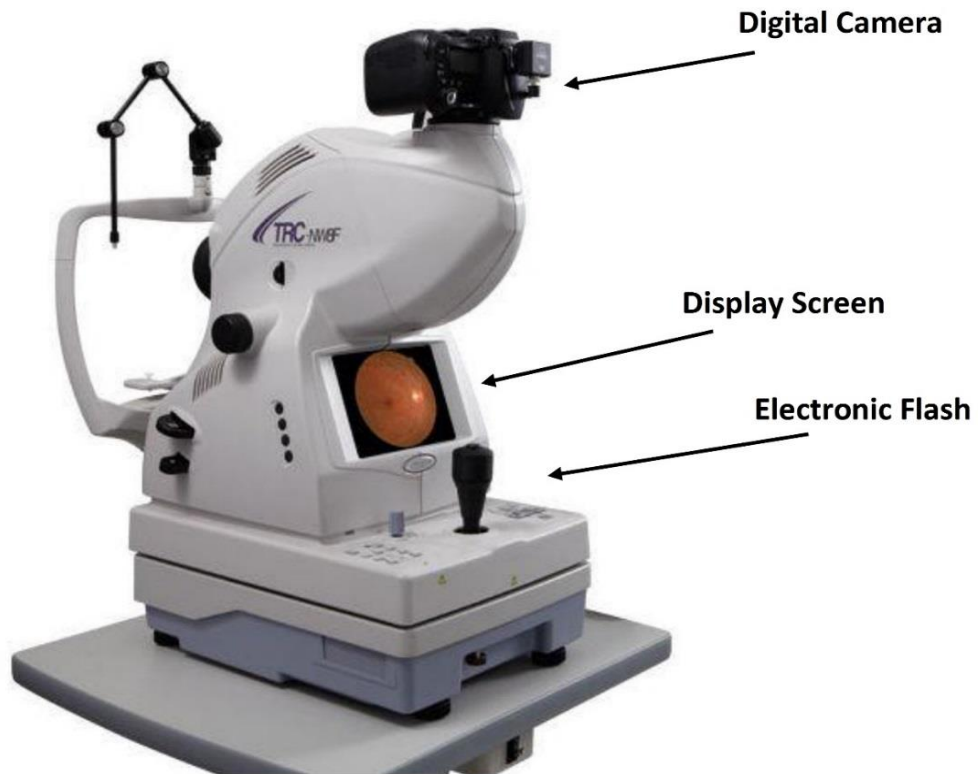
Figure 2.8. A fundus camera taken from Topcon Medical. The display screen shows the
captured retinogram. The electronic flash generates and focuses light (Stringa et al., 2017).

According to Abràmoff et al. (2010), fundus imaging can be defined as any process
involving a 2D demonstration of the 3D retinal structures estimated in the image channel
and acquired using light reflection, such that the intensities of the image can represent the
total amount of light reflected. Furthermore, various techniques and modalities belonging
to the fundus-imaging category are grouped together as discussed in Table 2.2 Different
fundus imaging modalities (Abràmoff et al., 2010).

CHAPTER 2: MEDICAL BACKGROUND ON THE STRUCTURE OF THE EYE AND
STATE-OF-THE-ART RETINAL ANALYSIS

Table 2.2 Different fundus imaging modalities (Abràmoff et al., 2010).

Name	Description
Fundus photography	At a specific wavelength, image intensities correspond to the amount of reflected light. This includes red-free, where the red colour is filtered out from the imaging light, enhancing the contrast of vessels and other structures.
Colour Fundus Photography	The retina is fully examined in colour by means of white light illumination. Subsequently, image intensities represent the amount of reflected red, green, and blue wavebands.
Stereo fundus photography	Allows depth estimation by exploiting two or more different view angles.
Hyperspectral imaging	Produces multiple specific wavelength bands. Potential diseases may be indicated by monitoring oxygen consumption in the retina.
Scanning laser ophthalmoscopy (SLO)	Provides sharp retinal images by a single-wavelength laser light obtained sequentially in time which can reach the surface of the retina and record its surface details.
Adaptive optics scanning laser ophthalmoscopy (AOSLO)	Optical light is corrected by modelling the deviation in its wavefront.
Fluorescein angiography	Image intensities constitute the amounts of photons emitted from photosensitive materials, i.e. fluorescein or indocyanine green fluorophore injected into the patient's bloodstream.

Ophthalmic ultrasound becomes increasingly important when doctors cannot see the
retina due to bleeding inside the eye, severe cataracts, or corneal scarring. This technique

is similar to the typical ultrasound used to scan different organs of human body, where sound waves are sent from a probe placed on the eye to provide sonar images of the inside of the eye (Nowozin et al., 2007). Essentially, optical coherence tomography (OCT) is an emerging technique that provides depth resolved, high-resolution images of biological tissue in real time and demonstrates great potential for imaging. Furthermore, the OCT is based on the fundamentals of low coherence interferometry, in order to measure the echo time delay of back-scattered light in the sample in the same manner as A-Scan ultrasound acquisition. A temporally and spatially low coherent beam of light (generated from a laser diode) is split into two disjoint paths. One is directed into the sample, whereas the other is directed into a reference mirror (at a known but variable distance from the source). Light from both beams is then reflected and overlaps within a fibre-optic interferometer (Broecker and Dunbar, 2005). Figure 2.4 shows an example of an OCT image of a normal human macula.

In conclusion, this chapter has summarised the anatomy of the eye as well as the overall arrangement of retinal layers. It has also discussed retinal imaging modalities, clinical lesions of the retina, and diabetic diseases. Then, retinal imaging techniques have been discussed. The next chapter reviews the literature regarding the retinal imaging diagnosis diseases used to discriminate between exudates and drusen lesions.

3. LITERATURE REVIEW OF RETINAL IMAGE ANALYSIS FOR DISEASE DIAGNOSIS

3.1 Introduction

Retinal image data is not always of the best quality, due to unwanted features such as colour variations, noise and lighting effects (Russ, 2016). Therefore, an image pre-processing stage is an essential step to enhance images prior to the application of testing techniques such as data mining methods. The quality of retinal images might be affected by a number of factors that are difficult to control, namely: (i) the subject's eye movement during the image acquisition process; (ii) pupil dilation; (iii) the presence of other retinal pathologies such as cataracts that block the light from reaching the retina; and (iv) photographer's skill and tiredness.

If any of these factors affect the quality of the images, the most common defects in retinal images are non-uniform illumination and colour variations. Colour variation within retinal images causes problems in distinguishing exudates from retinal backgrounds where in some cases the exudates may appear darker than or a similar colour to the retinal background as opposed to the more normal lighter colouring associated with exudates (Foracchia et al., 2005, Osareh, 2004). Therefore, images where exudates are present may be incorrectly classified as normal images, and vice versa.

3.2 Retinal Image Processing Techniques

This chapter describes a number of image processing techniques that have been applied to retinal images, which are relevant to the work described in this thesis. The aim of such techniques is to enhance the retinal image as well as to remove unwanted features from the images. This chapter explains how the image defects caused by the factors mentioned above can be corrected, and this includes four operations, namely: (i) image pre-processing, which includes image enhancement and noise removal; (ii) optic disc elimination; (iii) feature extraction; and (iv) exudate detection.

CHAPTER 3: LITERATURE REVIEW OF RETINAL IMAGE ANALYSIS FOR DISEASE DIAGNOSIS

3.2.1 Image Pre-processing

The human retina has three main sections. The optic disc (OD) is the point of exit of the optic nerve and there are no light receptors in this area, so it is also known as the blind spot. The fovea defines the centre of the retina and is located in the centre of the macula, which is the region of highest visual acuity, and exudates are bright yellow spots on the surface of the retina (Welfer et al., 2010).

Morphological and reconstruction operations are well-known technique tools to differentiate images of exudates into different types. Moreover, these operations are also capable of distinguishing between extremely complex images with overlapping or extracted components (Srisukkham et al., 2013, Omar et al., 2014), and they have been used in many research fields such as medicine, biomedicine, industry, computer vision, remote sensing, computer aided design, video coding and many more (Sun and Luo, 2009). Although extensive research has been conducted on exudate segmentation, this process of segmentation focus on various challenges such as the presence of noise, textured regions, low contrast, overlapping, and the size and intensity of the images (Gonzalez and Ballarin, 2009).

In particular, the optic disc and exudates show great similarities and high levels of variation in the intensity band of colour fundus images. Thus, the detection of exudates is a challenging task but is also very important in the diagnosis of diabetic retinopathy (Omar et al., 2016).

Youssef et al. (2010) proposed a method to detect areas of higher intensities, yellow colour, high contrast and contours. At first, they eliminated the blood vessels and the optic disc from images via edge detection, which gave an initial estimate of the exudates. Youssef et al. (2010) then used also a morphological reconstruction algorithm to achieve a final estimate of the exudates. In the work of Sánchez et al. (2009), Sánchez et al. (2010) the optic disc was automatically localized and masked out based on a regional maxima algorithm and the Hough transform. Morphological operations were then applied to segment the exudates.

Retinal image acquisition using a low-cost fundus camera is the most widely used method. However, the segmentation of bright lesions and subsequent follow–up

operations are not easy. This is due to the presence of anatomical structures with highly correlated pixels from the lesion, illumination variability, and the movement of the eye during the examination of the patient (Omar et al., 2014).

Omar et al. (2014) proposed a fast and efficient algorithm to extract exudates in colour fundus images. The proposed method is based on mathematical morphology and reconstruction operations and has two phases: (1) the elimination of blood vessels and the extraction of exudates; and (2) the detection of the optic disc, which is used to differentiate it from exudates (Omar et al., 2014). At this current stage of the work, exudates are detected using mathematical morphology and reconstruction techniques. An important step in the extraction process is to remove prominent structures in the retina, such as blood vessels and the optic disc (Acharya et al., 2009). This stage can be separated into three sub-stages, namely: pre-processing, optic disc elimination and exudate detection, which are explained in detail in the next sections. In the pre-processing phase, the RGB image in the original fundus image is converted in to HSI colour space. Then, the median filter is applied to the intensity band (I-band) of the image in order to suppress noise (Kirchner and Fridrich, 2010). Next, contrast-limited adaptive histogram equalization is applied so as to enhance contrast in order to prevent the over-saturation of homogeneous areas in the retinal image (Vij and Singh, 2009). The Gaussian function is also applied to remove noise (Jayakumari and Santhanam, 2007). In image processing, a Gaussian blur (also known as Gaussian smoothing) is the result of blurring an image by a Gaussian function. It is a widely used effect in image processing, typically to reduce image noise and reduce detail. After that, the colour fundus image is transformed into an HSI image and its intensity band is used for further processing (Sopharak et al., 2009, Sopharak et al., 2010). The results of these pre-processing operations are shown in Figure 3.1. Since the optic disc and exudates exhibit similarities and show high intensity values in the intensity band, therefore the optic disc needs to be eliminated. Also it is well-known that the object with the largest circular shape in a fundus image will be the optic disc (Sopharak et al., 2008, Kavitha and Duraiswamy, 2011).
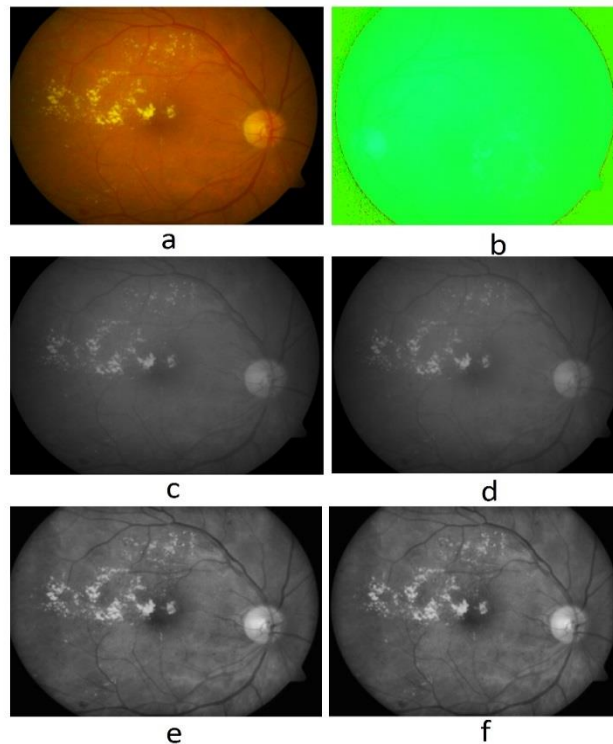
Figure 3.1. Images from the pre-processing phase (I1): a. RGB image; b. HSI space; c. image of intensity band; d. image after a median filter is applied; e. adaptive histogram equalisation technique; f. Gaussian function.

3.2.2 Optic Disc Elimination

At first, the closing operator with a flat disc shape structuring element is applied to the preprocessed image (Maragos and Schafer, 1990). The image obtained is converted in to binary format using a thresholding technique. Thresholding can be used to represent gray-level images by binary images, where the white background region could be represented by 0 and the shaded foreground could be represented by 1.

With this algorithm, the optic disc is eliminated before exudate detection, since both types of objects are of similar colour and intensity. The image is obtained after applying the morphological closing operator with a flat disc to eliminate high contrast blood vessels. Then, the optic disc can be extracted as it is the largest circular object in the fundus image. A weighting of 1.6 is used in Nilblack's method for thresholding. The region containing the optic disc is brighter than other regions in the retinal image.

Nilblack's method and the regionprops function are used to obtain the binary format. The largest connected object which provides a value of high density from these two methods is considered to be the optic disc. The image obtained after applying Nilblack's method shows high compactness in the large circular object (Omar et al., 2014).

Although the Hough transformation technique can also be used to isolate the optic disc in retinal images, the results are not always accurate when its shape is not circular (e.g. oval). (Sekhar et al., 2008). Thus, the Hough transform is not a reliable technique in detecting the optic disc since not all retinal images include circular optic discs. Therefore, the optic disc is detected and localized with the assist of once the modified regionprops function by combining the object's area and perimeter to isolate it as shown in Figure 3.2 (Omar et al., 2014).
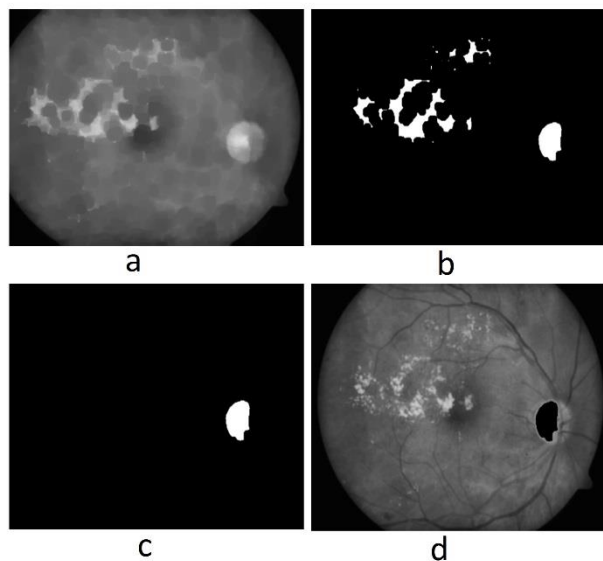
Figure 3.2. Images obtained during optic disc elimination (I2); a. closing operation technique; b. Nilblack's technique is used for image thresholding; c. large circular object is detected using the modified regionprops function; d. results obtained from the pre-processed image after the optic disc is isolated.

Sopharak et al. (2010) also proposed an algorithm based on the enhancement of contrast in the histogram equalization of the RGB image. A morphological closing operator was used to remove the vessels. Then an entropy feature was used to find and remove the optic

disc area. Morphological reconstruction based on a dilation operation was applied in order
to segment exudates.

3.2.3 Feature Extraction

Applications to extract texture and colour features have many potential uses in the field
of biomedical image analysis. A set of texture and colour features can be analyzed for the
purpose of the more accurate detection of drusens and exudates in the identification of
the presence and classification of DR and AMD disease patterns from retinal lesions.
These features are described as follows.

3.2.3.1   Granulometry morphological features (Gran):

Granulometry characterizes and measures the size distribution of image objects (Ifeachor
and Jervis, 2002). This approach is based on sequences of different sizes of morphology
opening operations. In this method, the difference between the original image and the
opening image is estimated, and the total of pixels are kept as one bin histogram.

In order to create the size distribution histogram, opening operations with in structural
element (SE) of a disk shape with different radius pixels are used. By using this method
with the green plane of the image. For this reason, the similar step is used to the green
plane however, in this example for each resultant image the mean value of the intensity
is estimated after masking it. This granulometry method is applied to the area open
operation (Acton et al., 2008) as an alternative of the opening operator convention.
Furthermore, the granulometry technique has the ability to discriminate the drusen lesion
in AMD disease from non-lesion.

3.2.3.2   Histogram of oriented gradient (HOG):

The HOG was first presented by Dalal and Triggs (2005) in the context of person
detection in images to extract shape information. According to their approach, the HOG
aims to describe the image by splitting it into patches and computing histograms of
oriented gradients for each patch and then all histograms are merged. This method has
been adopted in this work to extract new features from local patches. The calculation of
descriptors is conducted in the following steps:

1. Calculate vertical G_V and horizontal G_H image gradient by filtering with $[-1\ 0\ 1]$

2. Calculate both the orientation and norm of the gradient:

$$N_G\,(x,y) = \sqrt{G_H(x,y)^2 + G_V(x,y)^2} \qquad\qquad 3.1$$

$$O_G(x,y) = ata\,n\left(\frac{G_H(x,y)}{G_V(x,y)}\right) \qquad\qquad 3.2$$

3. Divide image by the number of cells.
4. Calculate a histogram for each cell.
5. All histograms within a block of cells are normalised.

Finally, the desired descriptor is acquired by grouping histograms that are normalised to a single vector. On the other hand, there are still some limitations to this method. For example, the computational complexity of over-size dimensions and the deprived global information of descriptors.

3.2.4 Exudate Detection

After the optic disc has been eliminated, the next step is to extract exudates. The morphological closing operator with a flat disc shape structuring element is applied to remove blood vessels, as both these and exudates display high contrast. A morphological closing operator with a flat disc shape structuring element of a radius of 10 pixels is applied to eliminate the high contrast blood vessels in the fundus images before applying thresholding techniques. This protects objects shaped like the optic disc, since it may not appear as a circular object in some retinal images (Gregory, 2015),(Omar et al., 2014).

The triangle method (Coudray et al., 2007) is used to obtain the thresholded image after enhancing the local contrast. Since the detection of exudates can be confused by the borders of both the optic disc and the images of certain other objects, the closing and opening operators are also used to remove image borders from the thresholded image in order to obtain closely distributed exudates. After that, flood filling is applied to all holes. Since, in some retinal images, the optic disc is close to the borders, and in others this is not the case, the modified regionprops function technique is used to isolate the optic disc.

CHAPTER 3: LITERATURE REVIEW OF RETINAL IMAGE ANALYSIS FOR DISEASE DIAGNOSIS

Next, a marker image mask is applied for morphological reconstruction (Gonzalez et al., 2008, Vincent, 1992). During morphological reconstruction, the peaks in the marker image are dilated and eroded until the contour of the marker image fits under the mask image. The difference between the image obtained in the previous step and the intensity band of the original image is taken for thresholding. The thresholded image obtained is superimposed on the original fundus image to extract the exudate, as shown in Figure 3.3 (Omar et al., 2014). The proposed method was tested on images from the DIARETDB1 database in order to evaluate the system (Kauppi et al., 2007). The performance of the algorithm was evaluated by comparing the resulting extraction with ground truth images. To evaluate the performance of the classifier, a measurement of sensitivity is used which is the proportion of the real exudate pixels that are detected.
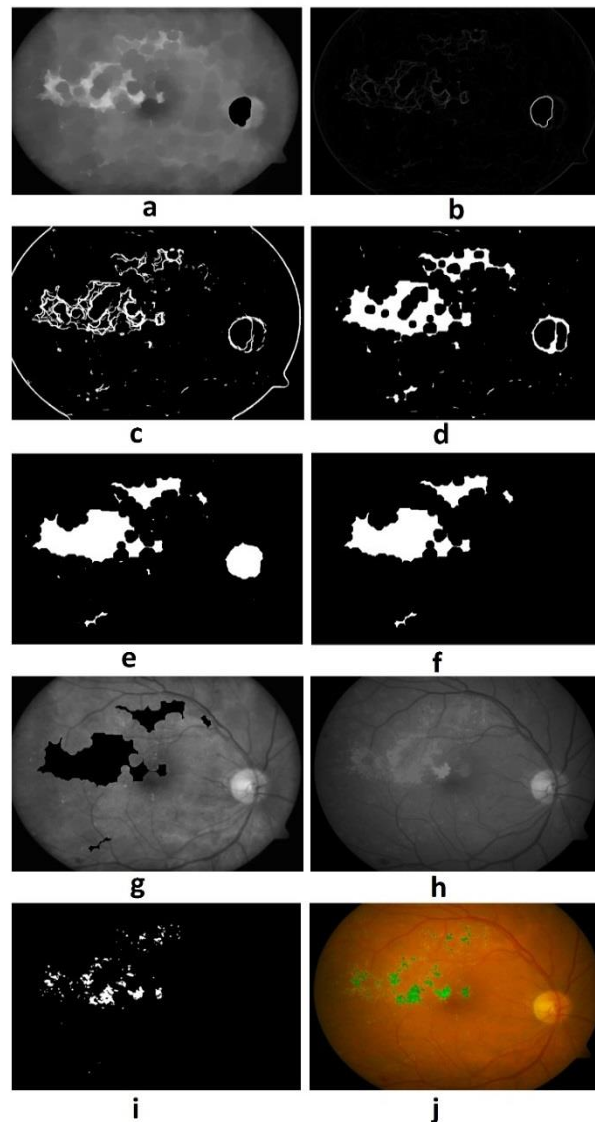
Figure 3.3. Images obtained during exudate detection (I3): a. closing operation technique; b. technique of standard deviation; c. triangle method for thresholded image; d. borders removed using closing operator; e. holes are filled; f. OD eliminated using modified regionprops techniques; g. mask of marker image; h. reconstructed morphological image; i. thresholded image; j. exudates obtained superimposed on original image and marked in green.

In comparison to previously published techniques, the proposed method achieved an average sensitivity of 85.39% (Omar et al., 2014), whereas the average sensitivity of other methods ranged from 43.48% (Sopharak et al., 2010), to 70.48% (Welfer et al., 2010) and 78.28% (Eadgahi and Pourreza, 2012). This shows that exudate detection using the

proposed method has significantly improved upon the results achieved using other methods in terms of sensitivity.

Welfer et al. (2010) applied mathematical morphology using the lightness, L, of the perceptually uniform LUV colour space where intensity fluctuations in the L channel were smaller than those in RGB. They applied a morphological contrast enhancement method using top-hat morphological techniques and a regional minima operation and thresholding for the detection of exudates. Eadgahi et al. (Eadgahi and Pourreza, 2012) proposed a method based on morphological operations. The green component was firstly taken from retinal images in a pre-processing stage. Then, the optic disc and blood vessels were eliminated from the image. Finally, the exudates were segmented by a combination of morphological operations such as top-hat, bottom-hat and reconstruction operations.

In the work of Ravishankar et al. (2009) and Kumari et al. (2010), blood vessels of different thickness were extracted using opening and closing morphological operations. Exudates were detected using the opening and closing operations with different sizes of structuring elements (SEs). The optic disc was obtained by subtracting the blood vessel image from the image of the detected exudates. Since both the exudates and the optic disc have similar features such as high gray levels and shapes, the optic disc is eliminated in most methods in order to reduce false positive rates.

Although the techniques previously presented have provided methods to identify exudates, these authors did not state clearly how optic discs are eliminated when in different locations. However, research has shown that exudate segmentation is a challenging problem due to the variability of illumination (Omar et al., 2014). Therefore, a bag of features (BoF) technique is used to overcome these problems and details of this approach are explained in chapter 6.

3.2.5 Equality Measurement

As a simple baseline for comparison, the performance for each parameter is measured by comparing the detection results with ophthalmologists' hand-drawn ground truth. Nine performance measurements, namely true positives (TPs, the number of lesion pixels correctly detected), false positives (FPs, a number of non-lesion pixels detected wrongly

as lesion pixels), false negatives (FNs, the number of lesion pixels that are not detected), true negatives (TNs, the number of non-lesion pixels which are correctly identified as non-lesion pixels), sensitivity (Sen), specificity (Spec), accuracy (Acc) and area under curve (AUC) are calculated (Attia, 2003, Kallergi, 2005). Equations 3-6 show the computation of the parameters of sensitivity, specificity, accuracy and area under curve respectively:

$$Sen = \frac{TP}{TP + FN} \qquad\qquad 3.3$$

$$Spec = \frac{TN}{TN + FP} \qquad\qquad 3.4$$

$$Acc = \frac{TP + TN}{TP + TN + FP + FN} \qquad\qquad 3.5$$

$$AUC = \frac{1}{2}\left(\frac{TP}{TP + FN} + \frac{TN}{TN + FP}\right) \qquad\qquad 3.6$$

3.3 Automatic Detection and Classification of Lesions

The growing prevalence of diabetes worldwide increases the total of cases that essential to be investigated by ophthalmologists. Additionally, the lack of professional experts and the high cost of physical examination prevent many people from receiving adequate treatment. Computer-aided detection (CAD) systems for retinal lesions associated with diabetes can offer various interesting benefits in terms of both diagnosis and clinical effort. Such systems give the opportunity to investigate a large number of images, and, typical examination costs can also be reduced as a consequence of reducing the workload of trained graders. Previous work describes three main important stages in the detection of retinal lesions and features in a wide variety of CAD systems. The first phase is pre-processing to compensate for the great variability of retinal images. The most preferred choice is to consider the green band of images because it provides a high contrast between different structures and retinal lesions. Extracting retinal lesions is the second phase, and feature selection techniques are the process most commonly performed to eliminate undesirable features. The last phase is to classify retinal lesions as healthy or non-healthy retinal images. Table 3.1 summarizes the different approaches used to classify retinal

lesions in terms of pre-processing, methodology, features, classification, the size of the dataset, and performance measurements such as accuracy, sensitivity, specificity, and area under the curve.

3.3.1 Automatic Detection and Classification of Exudates

A study by García et al. (2009) was based on the use of a neural network to extract hard exudates from retinal fundus images. The proposed technique consisted of pre-possessing and segmentation, and then neural network classifiers were used in the classification stage which consisted of the radial basis function (RBF), support vector machine (SVM) and multilayer perceptron (MLP). Luminosity and contrast normalization were performed on the green channel as a pre-processing step. Next, the enhanced image is subjected to a combination of local and global adaptive histogram thresholding in order to detect exudate regions to be classified later. Due to the similarity of the optic disk and exudate lesions in intensity, the optic disk has to be removed prior to classification. A total of 117 images were used, and the training set consisted of 50 images. After segmentation, a number of regions were extracted which were given labels by experts as exudates or non-exudates. Beside these, the ground truth of the dataset label is created to train with these 50 retinal images using the classifier. The test contains 67 retinal images (27 normal retinal images and 40 diabetic retinopathy patients). Eighteen features were selected including No's 1-6 where the values of mean and standard deviation (STD) of the colour fundus images were inside the region, No's 7-12 where the mean and STD of the colour fundus images had pixels values that belong to a rectangular part near to the region (with a distance of 5 pixels), No's 13-15 were colour fundus images values of the region, No's 16 was region of size. Finally, Prewitt operator was used in the perimeter of the region for the average of edge values.

To test the capability of the neural network, tenfold cross-validation was conducted. The tests obtained a mean positive predictive value (PPV) of 80.72% and a mean sensitivity (SE) of 88.14% using a lesion-based criterion and MLP classifier. Values of 88.49% sensitivity and 77.41% of positive predictive value were achieved using the RBF classifier, whereas 87.61% sensitivity and 83.51% positive predictive value resulted from using the SVM. Values of 100% sensitivity, 81.48% specificity and 92.54% accuracy

were achieved using the RBF neural network classifier. The overall results of 100% sensitivity, 77.78% specificity and 91.04% accuracy were achieved using the SVM classifier.

Deepak and Sivaswamy (2012) introduced a detection and classification approach to assess diabetic macular edema (DME) severity. Here, hard exudates were considered as a standard manifestation to assess DME, and the severity rate was assessed based on the proximity of the HE to the macula. Detection was achieved with normal retinal images using a supervised learning technique, where any deviation from the characteristics of a healthy retinal image might be a sign of a non-healthy retina. After that, the macula centre was detected automatically, and then the region of interest (ROI) extracted using the appropriate circle inside the fundus mask at the centre of the macula, and the optic disc was isolated. A method was proposed to generate motion patterns within the ROI, since HE may cause a bright smear pattern; however, the textural features of the background are smoothed. In order to create a motion pattern image (MPI), rotated versions of a given input image are generated, and then these are rotated images are combined using a mean or a maximum function to fuse all intensities at each pixel location. Radon-based features are extracted from the image MPI at different angles and the wanted feature vector is then constructed by concatenating them from different orientations. Subsequently, using a single class classifier, each image can be classified as normal or abnormal hard exudate image. The severity of the disease is measured via the metric of rotational asymmetry, such that in normal cases the macula is comparatively darker than other regions and is characterised by rotational symmetry. However, abnormal cases show asymmetric characteristics around the macula. Eight angular samples of the ROI were applied to generate eight patches and 10-bin histogram is created for each patch, which is called the symmetry measure. Finally, at a given threshold, each ROI can be measured for the risk of DME as in the moderate or severe stages. The retinal images were used from four different widely used databases: Diaretdb01, Diaretdb12, HEI-MED3, and MESSIDOR4. In total, 644 images were used and 367 are of healthy retinal images and 277 are non-healthy retinal images. In order to ensure the reliability of the result of DME evaluation, ten-fold cross-validation was used. As a result, the detection sensitivity was 100% values of specificity ranged between 74% and 90%. Immediate referral cases were detected with

100% sensitivity and 97% specificity. The accuracy of the severity classification was 81% for the moderate stages and 100% for severe.

Osareh (2006) proposed a method for the automatic identification of retinal HE in colour fundus images. The pre-processing in the proposed method combines two steps of retinal image normalization via histogram specification and local contrast enhancement. The idea is to select a reference image, and then the values of each image are adjusted such that its frequency histogram matches the distribution in the reference image. Next, in order to distribute the values of pixels around the local mean, local contrast enhancement is applied. This operation is performed on the intensity channel after converting RGB images into HSI colour space. The fuzzy C-means (FCM) clustering algorithm is used after the pre-processed images are segmented. A total of 18 features are extracted in the same manner as in García et al. (2009) study, but with different colour spaces. In the final stage, a perceptron neural network with three layers is used for classification purposes, with 18 input nodes (selected feature space), a single output node and 15 hidden units. A set of 75 colour images were used for training, of which 25 were normal retinal images and 50 were abnormal.

The segmentation results contained a number of exudate and non-exudate regions which were labelled by medical experts to obtain a fully labelled training dataset. The 67 colour fundus images were used in order to investigate the diagnostic performance of the system. The proposed system was able to achieve levels of sensitivity of 95.0%, specificity of 88.9% for image-based classification with a sensitivity of 93.0%, and a specificity of 94.1% for lesion-based classification.

Giancardo et al. (2012) proposed a method based on the classification of a single feature vector for each image to diagnose DME disease. The single feature vector consists of three steps in the analysis: the exudate probability map, colour analysis, and wavelet analysis. In the first type, the green channel as well as the intensity band from the HSI colour space were used. The retinal images are resized to a predefined height maintaining the height/width ratio, and then a large median filter whose size is approximately 1/30 the height of the fundus image is used after the background image is estimated. The normalization is enhanced with morphological reconstruction in order to improve the

removal of the nerve fibre layer and the edges of the optic nerve structures. The exudate probability map is obtained by hard thresholding. The field of view (the black area in the retinal image) is applied using a region growing approach with four seeds located at the angles of a down sampled version of the image; and the optic disk is removed as is common to all approaches in previous work. The Kirsch compass kernel technique is used with the probability map to select exudate candidates, each of which is assigned a score. In the second type of analysis, the colours of a new input image are equalized to a reference image by taking into account the scalar mean and standard deviation of that image. In the final stage, the second level of stationary Haar wavelet analysis is implemented with the intensity band of the HSI colour space. Colour and shape features such as Avg, Std, Max, Min and Med are extracted from different colour spaces via two different approaches. The exudate probability map is transformed in to two binary masks which are superimposed on the colour analysis and wavelet analysis results. The map of exudate probability is then applied to weigh the analysis results based pixel level.

Four different classifiers are used to evaluate system performance, and the results indicate that the SVM with a linear kernel achieves the best performance. The authors stated a new accessible database (HIE-MED) which consists of 169 images of patients from several ethnic groups and DME levels. By applying the proposed method to this database and two other widely available databases (DIARETDB1and MESSIDOR) they were able to achieve values of the area under curve (AUC) between 0.88 and 0.94 depending on the features and dataset used.

3.3.2 Automatic Detection and Classification of Drusen

Hijazi et al. (2011b) proposed a method to classify retinal images as either age-related macular degeneration (AMD) or non-AMD by adopting a case-based reasoning (CBR) approach. The CBR consists of three stages, which are image pre-processing; spatial histogram generation and feature selection. The first stage includes two steps of the enhancement of the image and retinal segmentation. In the first step, colour normalization is used to increase the visibility of the main retinal anatomy, and contrast enhancement technique is applied as well. In the second step, 2D Gabor wavelet filters are applied to

identify the pixel, which is classified either as vessel or non-vessel using a Bayesian classifier.

Usually, the colour histogram is used as a simple way to represent an image for the purposes of object identification. In this approach, the number of colours per image is quantized (reduced) to reduce computational complexity, and then the retinal image is divided in to different regions of the same size. Subsequently, spatial histograms that retain the colour and spatial information from the image are computed for each region. These histograms are then concatenated into a single-feature histogram. Each retinal image is thus characterised as a histogram sequences, with each encapsulated as a time-sequence curve where the x-axis signifies the histogram bins and the y-axis the number of pixels contained in each bin (Hijazi et al., 2011b). The feature selection process subsequently reduces the number of features by removing irrelevant (redundant) features, using a class reparability based method (the Kullback-Leibler distance measure). Finally, new cases are categorised according to the case base (CB) in terms of the similarity of cases, since the histogram in the CB can be represented as a time-series curve and a similarity measure can be achieved via dynamic time-wrapping (DTW). In order to measure system performance, a tenfold cross-validation method is applied, in and addition, two parameters are introduced which are the T parameter (number of selected features) and the number of bins. The best results were obtained with a T parameter of five and a small number of 32 colour bins where values of specificity, sensitivity, and accuracy achieved were 74%, 79%, and 77% respectively for a total of 144 retinal images described as 86 AMD and 58 non-AMD (Hijazi et al., 2011b).

Akram et al. (2013b) suggested a method to segment drusen lesions automatically in retinal images to diagnose AMD. The proposed algorithm incorporates three steps. Firstly, dark regions are eliminated using morphological closing, and after that image, intensity enhancement is performed using the adaptive histogram equalization technique. Secondly, Gabor kernel-based filter banks are used in order to find all possible bright lesions in candidate selection. The optic disk is eliminated using the Hough transform. Finally, various features are computed, such as average boundary intensity, area, minimum boundary intensity, compactness, maximum boundary intensity, mean hue, mean saturation, mean intensity value, and mean gradient magnitude. For classification

performance, the least-square support vector machine is adopted. Images were used from the STARE dataset, which includes 400 images 58 of which contain drusen. The levels of accuracy, sensitivity, and specificity achieved were 97%, 95% and 98.4% respectively. The proposed system was compared with ground truth data and these parameters computed. The system achieved 100% accuracy in finding drusen at image level.

Zheng et al. (2013a) introduced a system which combines a set of pattern recognition, computer vision, and machine learning algorithms. Image pre-processing incorporates image denoising (non-local mean filtering), retina mask generation (image thresholding and morphological erosion), illumination correction, and colour transfer to return all test images in similar colours. The detection strategy follows two consecutive procedures of pixel-wise and then group-wise classification. The idea of the former is to detect whether or not a pixel is a drusen using colour image descriptors (Hessian features) and multi-scale local descriptors (total variation features). Ada-boost was used for feature selection and the least-square support vector machine for classification. The false positive components from pixel-wise classification are removed using the group-wise classification and least square support vector machine classifier. The system's validation compares the results using drusen segmentation on a pixel-by-pixel basis. Two different datasets were used as follows: 50 images from CAPT7 and 88 from AMISH. Accuracy levels between 80% and 86%, sensitivity between 82% and 87%, and specificity between 71% and 78% were achieved based on this dataset.

Hijazi et al. (2011a) proposed another approach which relies on image circular and angular decomposition. The result of the decomposition stage is a set of images represented as trees. To determine the most frequently occurring sub-trees, a weighted frequent sub-tree mining approach is used. The training input data is adjusted in a vector representation form (with one vector per image) through a linear support vector machine to reduce the dimensionality of the selected features, and the weighted most frequent sub-trees are then employed. In the final classification stage, a support vector machine and naive Bayes are then used as two classifiers. Two different publicly available databases, ARIA5 and STARE6, a total of 258 images including 160 AMD and 98 normal were used. The classifier's performance was evaluated through class classification using

tenfold cross-validation. An accuracy level of 100% was achieved with the SVM and similar results of 95% accuracy with the naive Bayes classifier.

3.3.3 Automatic Detection and Discrimination of Drusen and Exudates

van Grinsven et al. (2013) designed an algorithm to discriminate between exudates and drusen automatically. The algorithm starts by partitioning the retinal image, after the mean subtraction of the colour channels, into a fixed number of squared patches. The first feature sets appropriate for discriminating between healthy and non-healthy images are as follows: RGB; YCbCr and HSV colour space as colour histogram features. Additionally, histogram of oriented gradients (HOG) descriptor, local binary pattern (LBP) and granulometry with different scales; histogram of laplacian of gaussian features were used. The second feature sets that is suitable to distinguish between drusen and exudates, and the colour histogram features are obtained from the green and blue channels; Y, H, S channels, V, LBP and HoG features. The two features sets are reduced to 24 and 32 dimensional feature vectors using the Ada-Boost technique at the features selection stage. By using class validation with 5-fold cross-validation, the features are selected empirically. The images are then retrieved and classified by adopting the bag of features approach. To retrieve images, similarity measures are applied; for instance, L1-norm, L2-norm and squared chord. The best results are obtained using the weighted squared chord; however, classification is achieved using the weighted nearest neighbour method using distance as a similarity metric. Several datasets were employed, including STARE, EUGENDA8, and MESSIDOR, with a total of 415 images. Two datasets were constructed which were called Set A and Set B and each set was then partitioned into a training and testing sets. In this way, the test set contains only images from different people and how well the system generalizes can be tested. For image retrieval and classification, the accuracy and AUC levels achieved were 0.76 and 0.9 respectively.

Niemeijer et al. (2007b) developed an algorithm that can automatically detect bright lesions in retinal fundus images as well as discriminating between exudates, drusen, and cotton wool spots. One hundred and thirty images containing bright lesions are used to build the training set. Retinal specialists segment all pixels in these images to be either

CHAPTER 3: LITERATURE REVIEW OF RETINAL IMAGE ANALYSIS FOR DISEASE DIAGNOSIS

exudates, drusen, cotton wool spots or retinal image background. Optic discs, vessels, and red lesions are enhanced and considered as part of the retinal image background. Three hundred retinal images were used to perform diagnostic validation (100 images containing lesions and 200 images with no lesions). The overall methodology is composed of four stages: probability map generation, bright lesion pixel clusters, bright lesion detection, and bright lesion classification. Firstly, the green channel is converted using a set of 14 digital filters, so that the bright lesion filter responses are different from the filter responses for non-lesion pixels. Secondly, in order to classify the pixels based on filter responses, the k-nearest neighbour (k-NN) classifier is used such that pixels with a probability higher than a predetermined threshold are grouped into bright lesion pixel clusters. Each bright lesion pixel cluster is usually referred to as a potential lesion. Thirdly, a set of potential lesion samples are extracted from the training set so as to discard false positive bright lesion clusters by training the second k-NN classifier. Each bright lesion pixel cluster is allocated a probability that the pixel cluster is a true bright lesion based on a number of features such as cluster contrast in the RGB colour space. The system achieved results for area under the curve, sensitivity, and specificity of 95%, 95%, and 88% respectively for the detection of any type of bright lesion, and $95\%-86\%$, $77\%-88\%$, and $70\%-93\%$ for the detection of exudates, drusen, and cotton-wool spots respectively.

Deepak et al. (2013) proposed a framework for the detection of bright lesions including hard exudates and drusen using visual saliency. In order to enhance local contrast, the top-hat filtering technique is applied with a disk-shaped structural element for the given image of the green plane. Then, the background of the image is estimated using median filtering and is subtracted from the enhanced image to reduce the uneven illumination defection. Contrast stretching is performed as a final step in pre-processing prior to saliency calculation. In order to detect perceptual objects such as hard exudates and drusen, a spectral residual (SR) model is employed for saliency computation. Using the generalized motion patterns (GMP) proposed by Cree et al. (2005). Feature extraction is performed on the saliency map using GMP by extracting radon features with orientations between $0° - 180°$ with a step of $3°$ and 256 bins. In this stage, retinal images are classified as healthy image or those having lesions using a k-nearest neighbour (k-NN) classifier.

CHAPTER 3: LITERATURE REVIEW OF RETINAL IMAGE ANALYSIS FOR DISEASE DIAGNOSIS

Valuable information on the locations of abnormalities in retinal images is provided using the saliency map to differentiate either hard exudates or drusen. The saliency image is split into a number of square patches of fixed size. If its value of saliency is greater than a predetermined threshold, the patch is identified as having lesions. The LBP texture features are extracted from the green band of all patches with lesions and each abnormal retinal image can be classified as having an HE or drusen lesion using an SVM classifier with an RBF kernel function. Five publicly available datasets were used (HEI-MED, Diaretdb, MESSIDOR, ARIA, STARE), and values of lesion discrimination and detection accuracy are ranged from 0.93 to 0.96 with an area under the curve between 0.88 and 0.98 depending on the dataset used.

So far, the different techniques used in the literature to classify retinal images with bright lesions such as exudates and drusen have been summarised as shown in Table 3.1. The proposed methodology is elaborated in depth in chapter 6.

Table 3.1 Summary of methods used to discriminate exudates and drusen. This table shows results for image-based criteria. However, * represents a lesion-based criterion. State: the paper uses more than one dataset, L: length of feature, EX: exudates, Dru: drusen, SE: mean sensitivity, SP: mean specificity, AC: mean accuracy, AUC: area under the curve, FCV: fold cross-validation, LOOCV: leave-one-out cross-validation, NNs: neural networks, k-NN: k-nearest neighbour, SVM: support vector machine, LS: least square, LDA: linear discriminant analysis, DTW: dynamic time wrapping, GMP: generalized motion pattern, LBP: local binary pattern.

Authors	Les-ions	Pre-processing	Methodology [State]	Features {L}	Classifi-cation	Dataset		Results			
						Train	Test	SE%	SP%	AC%	AUC
García et al. (2009)	EX	Luminosity normalization and contrast enhancement	Global and local histogram thresholding [x]	Colour and shape features (Broecker and Dunbar)	NNs (10 FCV)	50	67	100	92.59	97.01	…
Deepak and Sivaswamy (2012)	EX	Not necessary	Create motion patterns of a circular ROI [✓]	Radon-based features {36}	PCA (10 FCV)	367	277	…	…	…	0.92
Osareh (2006)	EX	Histogram specification and contrast enhancement	FCM clustering [x]	Colour and shape features {18}	NNs	75	25	93	94.1	…	…

Giancardo et al. (2012)	EX	Image normalization	Colour wavelet decomposition [✓]	Statistical features (Avg, Std, Max, Min, Med) {48}	SVM (LOOCV)	169	. . .	…	…	…	0.94
Omar et al. (2016)*	EX	Image normalization	Multiscale LBP texture approach [x]	Combination of texture features	k-NN and RBF-NN (FCV)	1506	800	98.68	94.81	96.73	…
Hijazi et al. (2011b)	Dru	Luminosity normalization and contrast enhancement	2D Gabor wavelet filters [x]	Spatial histograms {160}	DTW (10 FCV)	144	. . .	79	74	77	…
Hijazi et al. (2011a)	Dru	Luminosity normalization and contrast enhancement	Angular and circular decomposition [✓]	Weighted frequent sub-graph mining approach {3671}	SVM (10 FCV)	258	. . .	100	100	100	…
Akram et al. (2013a)*	Dru	Morphological closing and histogram equalization	Gabor filter banks [x]	Colour and shape features {10}	LS-SVM	400	. . .	95	98.4	97	…

Zheng et al. (2013a)*	Dru	Mean filtering, retinal mask generation and illumination correction	Pixel and group based classification [✓]	Hessian and total variation features	LS-SVM	88	. . .	87	78	86	…
Niemeijer et al. (2007b)	Dru & EX	Convolution with 14 digital filters	Bright lesion clustering k-NN [x]	Shape, colour, contrast, and position {83}	LDA	130	300	95	88	…	0.95
van Grinsven et al. (2013)	Dru & EX	Mean subtraction	Bag of words approach [✓]	Histograms, LOG, HOG, LBP, and granulometry {58 × no of patches}	k-NN (5 FCV)	225/ 379	36	…	…	…	0.9
Deepak et al. (2013)	Dru & EX	Top hat filtering, in addition to contrast stretching	Visual saliency map and GMP [✓]	LBP {256 × no of patches }	SVM (10 FCV)	388	. . .	…	…	…	0.96

45

3.4 Summary and Conclusion

As discussed above, a variety of methods have been used for lesion segmentation, but many of these have serious limitations. For example, the low quality of images affects the separation results for dark and bright lesions using segmentation and thresholding techniques, whereas other classification methods are concerted on computing power for classification and training (Srisukkham et al., 2013). Research has also shown that exudate segmentation is a challenging problem due to the variability of illumination. In particular, the optic disc and exudates show great similarities in terms of high levels of variation in the intensity band of colour fundus images. Thus, the segmentation of exudates and the optic disc is a challenging task in DR diagnosis (Omar et al., 2014).

In attempting to develop automatic computer-aided diagnosis (CAD) systems for diabetic retinopathy several methods have been proposed, but the precision achieved in detecting bright lesions in retinal images is still a challenge. It has been widely used in previous studies and concern on the analysis of vessels measurements for retinal fundus images (Omar et al., 2016). For example, reports of existing techniques do not clearly state how exudates are extracted when a segmentation process is used. Due to its shape, the fundus image exhibits high illumination in its area, whereas the boundaries are dark. Uneven brightness, small lesions, low contrast and the existence of other objects in the retina with comparable characteristics, for instance the optic disc, make it difficult to identify exudates accurately (Singh and Tripathi, 2010).

Exudates are signs of DR and are not easy to detect due to other normal retinal characteristics with similar features such as contrast, intensity levels, colour and shape. When digital fundus images are captured using cameras with uneven illumination, the detection problem becomes even more difficult. However, it has been revealed that LBP texture features (Omar et al., 2016) and the BoF approach offers an efficient solution to overcome these issues and this is discussed in more detail in chapter 6.

In conclusion, this chapter has summarised image processing techniques. It also discussed an automatic detection and classification of lesions. This chapter also reviewed the literature regarding different methods used to discriminate between drusen and exudates and has concluded with a chapter summary. As the main goal of this thesis is to render the automatic

detection of exudates and drusen in fundus images more suitable for the detection of diabetic retinopathy and AMD disease, multiple algorithms are proposed in the relevant domains to improve efficiency by either reducing resource (computational) usage or by improving the overall accuracy of the proposed algorithms.

This thesis mainly focuses on improvements in the detection of exudates and drusen by developing novel methods for feature extraction that can be easily used in DR and AMD diseases diagnosis. As the detection of exudates and drusen extends into many areas of computer science, such as medical image processing, optimization, and machine learning are the variety of improvements could be possible in each domain, resulting in better outcomes in image retinal analysis in terms of computational cost and the accuracy of the abnormalities detection. The methods proposed in each key stage are discussed in the subsequent chapters in this thesis.

4. DETECTION AND CLASSIFICATION OF RETINAL FUNDUS IMAGE EXUDATES USING REGION BASED MULTISCALE LBP TEXTURE APPROACH

4.1 Introduction

As mentioned earlier in chapter 2, DR is a primary cause of impaired vision and blindness in people of working age in industrial countries. DR is a long-term condition affecting the blood vessels in the eye which occurs when high blood sugar levels damage cells in the retina which lines the back of the eye. Signs of diabetic retinopathy are found in approximately 33% of people with diabetes is 1.8 million of the 37 million cases of blindness globally (Shah, 2008). There are two forms of DR: non-proliferative (NPDR) and proliferative diabetic retinopathy (PDR). In NPDR, the blood vessels are damaged and more liquid leaks into the eye, leading to exudate formation in the retina. In PDR, the blood breaks running in the vessels of the eye. The presence of exudates is one of the most significant signs and a primary indication of DR. Figure 4.1 shows images of a normal retina and one with exudates.

The retina contains sensitive soft tissue and ophthalmologists usually examine retinal images, which are also known as digital fundus images, taken with a digital retinal camera for diagnostic purposes.
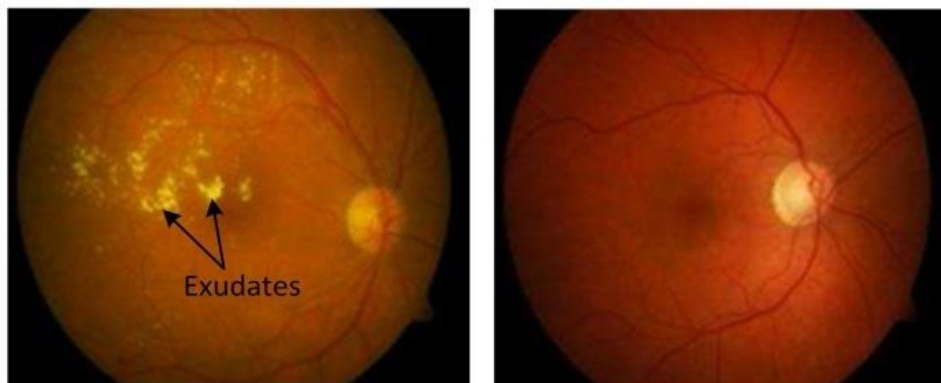
Figure 4.1. (a) Retinal image with exudates and (b) normal retinal image.

Exudate is locative positions of random whitish or yellowish patches, varying in shape and size. These are the most visible sign of DR and are the most important reason for visual loss in the non-proliferative form of DR. Retinal segmented images are classified as abnormal or normal by extracting regions based textural characteristics (Li et al., 2014). It is proposed in

this chapter that local binary pattern (LBP) texture features can be used for exudate detection. LBPs are applied for the textural features of regions of interest (ROIs) in colour retinal images. Artificial neural networks (ANNs) are generally used in several fields to overcome the problem of non-linear relationships and predictions (Shamshirband et al., 2014a, 2014b, 2014c). The ROIs are identified as exudate or non-exudate based on neural networks using the radial basis function (RBF) and k-nearest neighbours (k-NNs) classifiers. The proposed technique is then evaluated in terms of its sensitivity, specificity and accuracy.

This chapter is organized as follows. Section 4.2 discusses related work followed by a description of the materials and methodology used in Section 4.3. The results are presented in Section 4.4, and section 4.5 concludes the chapter.

4.2 Related Work

A good number of methods have been proposed for the detection of exudates in the diagnosis of DR using high-quality retinal fundus images whereas this work has been implemented with different retinal image quality. . Abramoff et al. (2010) proposed an approach to the identification of exudates by combining edge detection with the region growing technique. Other researchers (Walter et al., 2002) have identified exudates from the green colour channel according to gray-level variation in retinal images. Sopharak et al. (2010) suggested an automatic technique to classify exudate lesions using the naive Bayes classifier, while Karegowda et al. (2011) reported that exudates could be detected in retinal images using the back propagation learning technique with a neural network classifier. Here the decision tree technique was used to identify important features and the Hough transform and canny edge detection methods were also used for optic disk isolation, with mathematical morphological operations developed for blood vessel removal. Retinal images have also been classified as exudates or non-exudates using a Bayesian classifier (Ege et al., 2000).

Osareh et al. (2009a) proposed a technique to segment fundus retinal images using the fuzzy c-means (FCM) clustering method. Features are extracted and rated using a genetic technique and identified by applying a neural network classifier. It has been reported that the green channel of retinal fundus images gives high contrast values and provides important information for detecting exudates (Youssef et al., 2010), and morphological operations and texture analysis methods have been applied to retinal images to detect different stages of DR (Singh and

CHAPTER 4: DETECTION AND CLASSIFICATION OF RETINAL FUNDUS IMAGE
EXUDATES USING REGION BASED MULTISCALE LBP TEXTURE APPROACH

Tripathi, 2010, Youssef et al., 2010). Exudate detection has also been investigated in colour retinal images using morphological operations and the modified region-props function (Omar et al., 2014), whereas Niemeijer et al. (2007b) used a method to discriminate bright lesions, including exudates, drusen and cotton wool spots, from retinal colour images.

As discussed above, a variety of methods have been used for the detection of exudates, but many of these have serious limitations due to the quality of the retinal images. Consequently, the quality of fundus images is usually verified by the photographer in the acquisition moment. Fundus images should be retaken if the image quality can impair an adequate assessment of key features in retina. To capture a high quality fundus image, proper camera-to-eye distance should be maintained to avoid haziness and artifacts. As a result, the low quality of images affects the separation results for dark and bright lesions using segmentation and thresholding techniques thus avoiding any loss of valuable details and information in the regions of interest (ROIs) containing exudates, whereas some of them are concentrated on power computation for training and testing classification and. Therefore, a texture feature-based region method has been adopted in this research. The ROIs are converted from RGB to the green channel, which provides the highest contrast in digital fundus images (Saine, 1984).

In attempting to develop automatic computer-aided diagnosis (CAD) systems for DR, several techniques have been proposed (Ege et al., 2000, Walter et al., 2002, Rema and Pradeepa, 2007, Niemeijer et al., 2007b, Osareh et al., 2009a, Singh and Tripathi, 2010, Abramoff et al., 2010, Sopharak et al., 2010, Karegowda et al., 2011, Omar et al., 2014). However, precision in detecting bright lesions in retinal images is still a challenge. For instance, reports of existing methods do not clearly state how exudates are extracted when a segmentation process is used. Due to its shape, the fundus image exhibits high illumination in its central area, whereas the boundaries are dark. Uneven brightness, small lesions, low contrast and the existence of other objects in the retina with comparable characteristics, for instance the optic disc, make it difficult to identify exudates accurately (Singh and Tripathi, 2010).

This chapter proposes a system for automatic exudate detection which can be used for diagnosis of DR in its early stages (Omar et al., 2016). This is achieved via the analysis of the texture feature patterns in ROIs, which are uncertain regions in a retina. It is worth noting that local binary patterns (LBPs) have been used for the segmentation of ROIs in retinal images (Fathi and Naghsh-Nilchi, 2013). In this chapter, ROIs are classified into healthy and non-healthy

(i.e. containing exudates) states by conducting experiments with two different classifiers: a neural network based on the radial basis function (RBF-NN), and the k-nearest neighbour (k-NN) method.

4.2.1 Materials and Methodology

This section provides details of the proposed technique for exudate detection using retinal images. Figure 4.2 shows the framework for this method and its different components are described below.

4.2.2 Database Used for Validation

Retinal fundus images used for the experiments were collected from the publically available benchmark DIARETDB0 database (Kauppi et al., 2006). The dataset consists of 130 RGB retinal images captured at 500 field of view (FoV) and marked by four specialists whereas 110 RGB retinal images are abnormal and 20 RGB retinal images are normal. The fundus retinal images are stored in png format at a resolutions of 1500×1152 and the regions of interest (ROIs) of size 32×32 pixels were used for experiments. These RGB fundus images contain different lesions; for example, microaneursysms, haemorrhages and exudates. The database also contains the ground truth images, which were used to test the proposed algorithm.

4.2.3 Image Pre-processing

A fundus image always needs to be enhanced during a pre-processing stage due to the colour profile and non-uniform illumination (Akram et al., 2013a). All ROIs have been extracted and the green channel is selected from RGB image, which provides the highest contrast (Akram et al., 2013a). However, a segmentation process is not needed, thus avoiding any loss of valuable information in the regions of interest (ROIs) containing exudates (Omar et al., 2016).
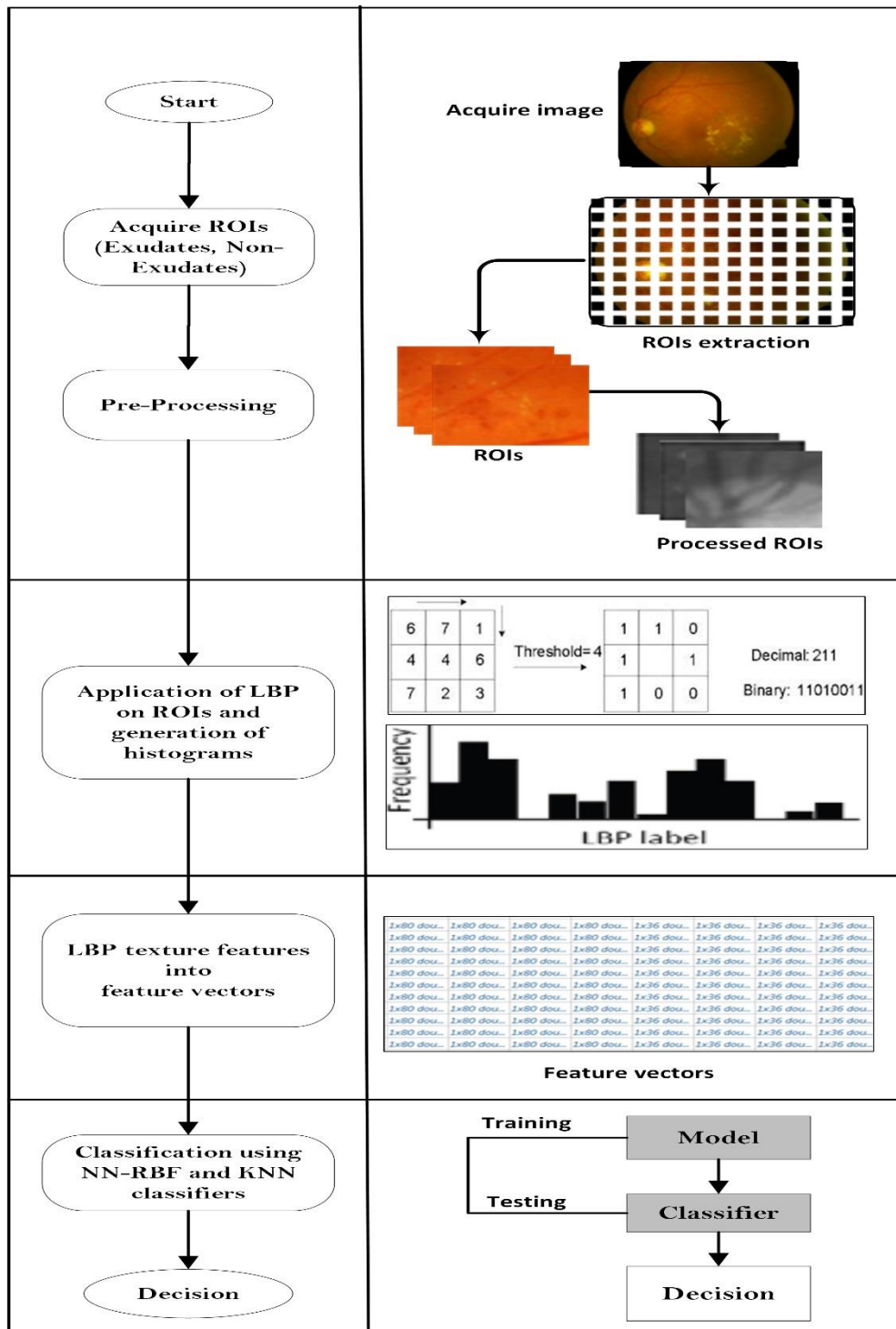
Figure 4.2. Proposed methodology architecture.

4.2.4 Acquisition of ROIs

Each image is divided into regions of interest (ROIs) of size 32×32 pixels. There are two types of ROIs, the first being normal fundus images which have not been screened by optometrists and the second are abnormal fundus images that have, with exudates marked by four optometrists. One thousand healthy and 1306 non-healthy regions were collected manually for the experiments and for the validation of the proposed method. This gives a total of 2306 sub-images used in the experiments.

4.2.5 Region Texture Feature Extraction Using Multi-scale Local Binary Patterns

Texture is one of the most significant features of an image, and the proposed technique for the texture extraction features of combines LBP multi-scale features with multiple windows of different sizes and versions. By varying the sampling radius, R and combining the LBP images, a multiresolution representation based on LBP, called multi-scale local binary patterns (Ojala et al., 2002) can be obtained. This representation has been suggested for texture classification and the results reported for this application show that its accuracy is better than that of the single scale local binary pattern method. The standard LBP operator is not very robust against local changes in the texture such as changes in viewpoint or illumination of retinal images. As a result, local features computed in a 3×3 neighbourhood cannot capture large scale structures that may be the only relevant texture features. In order to solve this problem, it is important to extend this idea to a multi resolution LBP operator (Huang et al., 2009). The new idea is to use a set of points equally spaced on a circle centred at a pixel to be labelled. Thus, this permits any radius and number of sampling points. If a sampling point doesn't fall in the centre of a pixel, bilinear interpolation is used.

Another extension using uniform patterns is proposed, which can be applied in order to reduce the length of the feature vector while keeping its discriminative power. A LBP pattern is called uniform if the binary pattern encompasses maximum two bitwise transitions from $0-1$ or from $1-0$. For instance, the patterns (00000000) (no transitions), (01110000) (two transitions) are uniform, whereas (11001001) (4 transitions) and (01010010) (6 transitions) are not uniform. This constraint reduces the number of the LBP patterns from 256 to 58 for eight points (Luo, 2012).

The local binary patterns (LBPs) are used to extract features at different multi-scales. The texture descriptor of the LBP is used to extract features of ROIs (Pietikäinen et al., 2011). Different versions of LBP have been suggested, including uniform (u2), rotation invariant (ri) and rotation invariant uniform (riu2) and the LBP descriptors size was used of the $LBP_{8,1}^{u2}$ combined with $LBP_{16,1}^{riu2}$ and $LBP_{16,2}^{riu2}$ (Ojala et al., 2002). The first step in the LBP is to produce a label for each pixel in the image, where the label is found based on the local neighbourhood of the pixel which is defined by a radius, R, and a number of points, P. The neighbouring pixels are thresholded with respect to the gray value of the central pixel of the neighbourhood, generating a binary pattern. The value of an LBP label is obtained for every pixel by summing the binary pattern weighted with powers of 2 as follows:

(a)   (b)
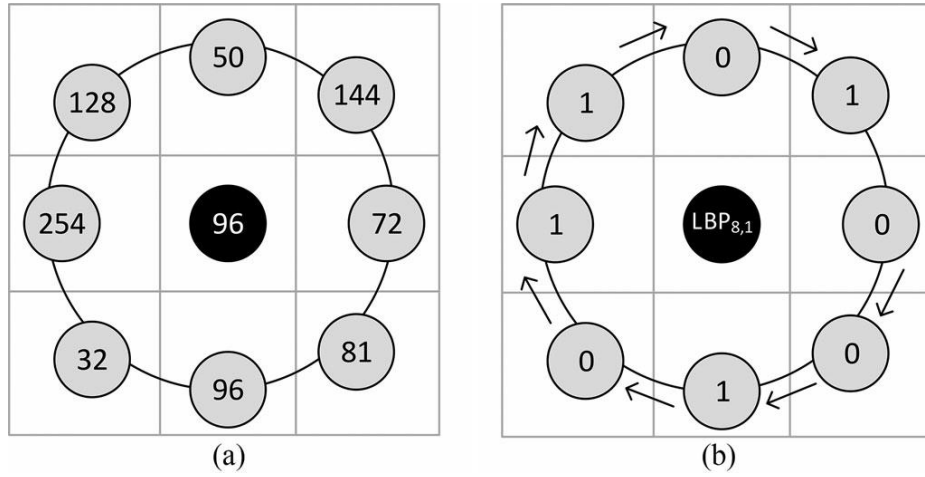
Figure 4.3. LBP computation: (a) gray values of a circular neighbourhood of radius 1 and 8 samples; (b) thresholding between the gray value of the neighbourhood and the central pixel. The rotation invariant LBP generated is 00101101 (the arrows indicate the order in which the pattern is formed). Specifically, the LBP label is obtained as follows: $LBP_{8,1} = 0 \times 2^0 + 0 \times 2^1 + 1 \times 2^2 + 0 \times 2^3 + 1 \times 2^4 + 1 \times 2^5 + 0 \times 2^6 + 1 \times 2^7 = 180$

$$LBP_{P,R} = \sum_{p=0}^{P-1} s(g_{p-}g_c) . 2^p \quad , s(x) = \begin{cases} 1, & if \ x \geq 0 \\ 0, & if \ x < 0 \end{cases} \qquad 4.1$$

where g_P and g_C are the gray values of the neighbourhood and central pixel respectively and P represents the number of samples in the symmetric circular neighbourhood of radius R. The g_P values are interpolated to fit with a given R and P. The values of the labels depend on the size of the neighbourhood (P). 2^P different binary patterns can be generated in each neighbourhood. However, the bits of these patterns must be rotated to the minimum value to achieve a rotation-invariant pattern. In the case of $P = 8$, only 36 of the 2^P possible patterns

are rotation-invariant, so that $LBP_{8,R}$ can have 36 different values. Figure 4.3 shows how LBP are calculated for a circular neighbourhood of radius 1 ($R = 1$) and 8 samples ($P = 8$).

LBP operators are easy to use and computationally efficient in terms of execution time. The advantage of the LBP is its economy of memory use and suitability for real-time applications. Moreover, it is powerful against gray-level intensity monotonic changes caused by varying illumination and high contrast, hence making it appropriate in the analysis of retinal images. The LBP effectively captures small-scale differences in texture and is appropriate for detecting exudates (Fathi and Naghsh-Nilchi, 2013). Experiments were contacted using various neighbourhoods and radii, and it was found that the $LBP_{8,1}^{u2}$ combined with $LBP_{16,1}^{riu2}$ and $LBP_{16,2}^{riu2}$ gave good results. The histogram of LBP codes is computed to serves as the feature vector for the ROIs after calculating the LBP codes.

4.2.6 Texture Region Classification

The next stage of the proposed method is region classification, where all features obtained in texture feature extraction are fed to the classifier. Classifying these segmented regions into abnormal and normal regions is a two-class classification problem. An RBF neural network and k-NN classifiers are used at the classification stage. RBF neural networks with linear output are often used in pattern classification because appropriate parameters for the basic functions can be conveniently chosen using an unsupervised technique (Turnbull and Elkan, 2005). The extracted textural features using the LBP technique and LBP histograms were applied to serve for RBF neural networks in classifying ROIs into normal and non-healthy regions. The input information is used to decide which of the two classes each ROI belongs to.

A radial basis function (RBF) network is embedded into a neural network, where each hidden unit implements a radial activated function. The output units implement a weighted sum of hidden unit outputs. The input into an RBF neural network is non-linear, while the output is linear. Generally, the RBF neural network is a three-layer, feed-forward network that consists of one input layer, one hidden layer, and one output layer. Various functions have been tested as activation functions for RBF neural networks such as the Gaussian activation function shown in the following equation:

$$\emptyset_j \ (X) = \exp\left[-\frac{\|X - \mu_j\|^2}{2\sigma_j^2}\right] \qquad\qquad 4.2$$

For $j = 1, \dots, L$ where X is the input selected $1 -$ dimensional feature vector, L is the number of hidden units, μ_j and σ_j are the mean and the standard deviation respectively of the jth Gaussian activation function. The norm is Euclidean. The output layer implements a weighted sum of hidden-unit outputs:

$$\Psi_k \ (X) = \sum_{j=1}^{L} \lambda_{jk} \ \phi_j \ (X) \qquad\qquad 4.3$$

For $k = 1, \dots, M$, where λ_{jk} are the output weights each corresponding to the connection between a hidden unit and an output unit and M represent the number of output units. The weights λ_{jk} show the contribution of a hidden unit to the respective output unit. Furthermore, the output of the radial basis function is usually limited to the interval $(0, 1)$ using the sigmoidal function:

$$Y_k \ (X) = \frac{1}{1 + \exp[-\Psi_k \ (X)]} \ , k = 1, \dots, M \qquad\qquad 4.4$$

A training set is an m labelled pair $\{X_i \ , d_i\}$ that represents the association of the given mapping between texture feature vectors and their desired output. The training mechanism is used to minimize the sum of squared error between the desired outputs d_i and the actual outputs $Y_k(X)$. The gradient-descent method is used in this chapter to train the parameters, and thus, μ_j, σ_j and λ_{jk} is updated as follows:

$$\Delta\mu_j = - \rho_\mu \nabla \mu_j \ E \qquad\qquad 4.5$$

$$\Delta\sigma_j = -\rho_\sigma \frac{\partial E}{\partial\sigma_j} \qquad\qquad 4.6$$

$$\Delta\lambda_{jk} = -\rho_\lambda \, \frac{\partial E}{\partial \lambda_{jk}} \qquad\qquad 4.7$$

where ρ_μ , ρ_σ and ρ_λ are small positive constants.

Neural networks based on the radial basis function (RBF) have the advantage of fast learning rates, and they have been proven to provide the same level of discrimination as multi-layer back propagation (MLP) algorithms in many applications.

A 3-dimensional texture feature vector which represents the selected texture features of size 38 feature vector was computed for the 1306 exudate and 1000 non-healthy regions in the dataset (Kubat, 1999). Ten-fold cross-validation was also used to train and test the generalization ability of the NNs, as this gives an estimation of the prediction risk (Moody, 1994). However, the k-nearest neighbour (k-NN) classifier was also tested in the experiments.

4.3 Results and Discussion

The performance of the proposed technique has been tested and evaluated on the DIARETDB0 dataset (Kauppi et al., 2006). The dataset consists of 1306 abnormal and 1000 normal regions. The experiment was conducted using 10-fold cross-validation for both the RBF neural network and k-NN classifiers.

The usual method employed to evaluate the performance of algorithms in image processing is by determining the ability to make decisions compared with the ground truth data. The proposed system was evaluated using the commonly used measurements of sensitivity (Sen), specificity (Spec), positive predictive value (PPV). These parameters were computed using the following equations:

$$Sen = \frac{TP}{TP + FN} \qquad\qquad 4.8$$

$$Spec = \frac{TN}{TN + FP} \qquad\qquad 4.9$$

$$PPV = \frac{TP}{TP + FP} \qquad\qquad 4.10$$

where:

TP (true positive) is an exudate region correctly classified by the classifier.

FP (false positive) is a non-exudate region wrongly classified as an exudate region by the classifier.

TN (true negative) is a non-exudate region correctly classified by the classifier.

FN (false negative) is an exudate region wrongly classified as a non-exudate region by the classifier.

The first set of experiments has been conducted with different LBP variants by varying the number of samples in the neighbourhood taken with different of values radius. Then, the LBP codes were computed from the exudate and non-exudate regions so that the code of the LBP histogram was computed to work as an ROI feature vector. These feature vectors were then allocated the class labels A and N as vectors calculated from the ROIs and identified as being exudates or normal with no sign of DR.

The feature vectors were then used as input for the RBF neural network and k-NN classifiers for the classification of ROIs into normal or abnormal (with signs of exudates) regions. A comparison of the results obtained in experiments using different versions of LBPs at different radii with the k-NN and RBF neural network classifiers are presented in

Table 4.1 and Table 4.2, whereas the values of sensitivity, specificity and accuracy for the LBP are illustrated in Figure 4.4 andFigure 4.5.

It is observed from Table 4.2 that the $LBP_{8,1}^{u2}$ combined with $LBP_{16,1}^{riu2}$ and $LBP_{16,2}^{riu2}$ give better mean values of sensitivity, specificity, PPV and accuracy than other versions of the LBPs. These LBPs were computed from 8 neighbouring pixels lying at a radius of 1 from the pixel centre, and by taking u2-based histogram bins combined with riu2 uniform with 16 samples at radii of 1 and 2. It is also shown that accuracy in different parameters is also decreased in the riu2 and u2 variants of LBP when the radius is increased from 1 to 4. Hence, the choice of pixels lying at a smaller radius produces better results and achieves minimum values when the radius is 1 or 2. If the radius is increased even further, then accuracy is reduced. Great care must be taken when increasing the radius in LBP computation. Thus, by increasing the value of the radius, then the size of the ROIs will be reduced considerably.

Table 4.1 Experimental results of k-NN classifier

LBP Version	Sen (%)	Spec (%)	FNR (%)	FPR (%)	PPV (%)	Acc (%)
ri-(8,1)	89.23%	82.00%	10.77%	18.00%	86.57%	86.09%
ri-(8,2)	88.46%	86.00%	11.54%	14.00%	89.15%	87.39%
ri-(8,3)	87.69%	86.00%	12.31%	14.00%	89.06%	86.96%
ri-(8,4)	82.31%	86.00%	17.69%	14.00%	88.43%	83.91%
u2-(8,1)	90.77%	94.00%	9.23%	6.00%	95.16%	92.17%
u2-(8,2)	91.54%	89.00%	8.46%	11.00%	91.54%	90.43%
u2-(8,3)	89.23%	87.00%	10.77%	13.00%	89.92%	88.26%
u2-(8,4)	83.08%	88.00%	16.92%	12.00%	90.00%	85.22%
riu2-(8,1)	90.00%	86.00%	10.00%	14.00%	89.31%	88.26%
riu2-(8,2)	88.46%	87.00%	11.54%	13.00%	89.84%	87.83%
riu2-(8,3)	87.69%	85.00%	12.31%	15.00%	88.37%	86.52%
riu2-(8,4)	82.31%	84.00%	17.69%	16.00%	86.99%	83.04%
riu2-(16,1)	90.77%	85.00%	9.23%	15.00%	88.72%	88.26%
riu2-(16,2)	88.46%	86.00%	11.54%	14.00%	89.15%	87.39%
riu2-(16,1-2)	91.54%	94.00%	8.46%	6.00%	95.20%	92.61%
riu2-(16,1-2)+u2-(8,1)	**93.03%**	**94.60%**	**6.97%**	**5.40%**	**95.74%**	**93.71%**

Table 4.2 Experimental results of k-NN classifier

LBP Version	Sen (%)	Spec (%)	FNR (%)	FPR (%)	PPV (%)	Acc (%)
ri-(8,1)	92.96%	92.90%	7.04%	7.10%	94.47%	92.93%
ri-(8,2)	91.96%	92.70%	8.04%	7.30%	94.27%	92.28%
ri-(8,3)	91.65%	92.10%	8.35%	7.90%	93.81%	91.85%
ri-(8,4)	87.44%	89.40%	12.56%	10.60%	91.51%	88.29%
u2-(8,1)	93.03%	94.10%	6.97%	5.90%	95.37%	93.50%
u2-(8,2)	92.04%	93.20%	7.96%	6.80%	94.65%	92.54%
u2-(8,3)	90.12%	92.40%	9.88%	7.60%	93.93%	91.11%
u2-(8,4)	87.37%	88.60%	12.63%	11.40%	90.92%	87.90%
riu2-(8,1)	91.81%	93.00%	8.19%	7.00%	94.48%	92.32%
riu2-(8,2)	91.04%	91.10%	8.96%	8.90%	93.04%	91.07%
riu2-(8,3)	90.89%	91.20%	9.11%	8.80%	93.10%	91.02%
riu2-(8,4)	86.06%	87.50%	13.94%	12.50%	89.99%	86.69%
riu2-(16,1)	92.96%	92.60%	7.04%	7.40%	94.25%	92.80%
riu2-(16,2)	90.89%	93.60%	9.11%	6.40%	94.88%	92.06%
riu2-(16,1-2)	92.96%	95.60%	7.04%	4.40%	96.50%	94.10%
riu2-(16,1-2)+u2-(8,1)	**98.68%**	**94.81%**	**1.32%**	**5.19%**	**94.94%**	**96.73%**

It is also shown that using a combination of LBPs with different versions achieves high of accuracy as compared with each individual LBP version. This is because large windows contain more texture information as regards to LBP^{u2}, and therefore it is easier to differentiate between texture patterns.
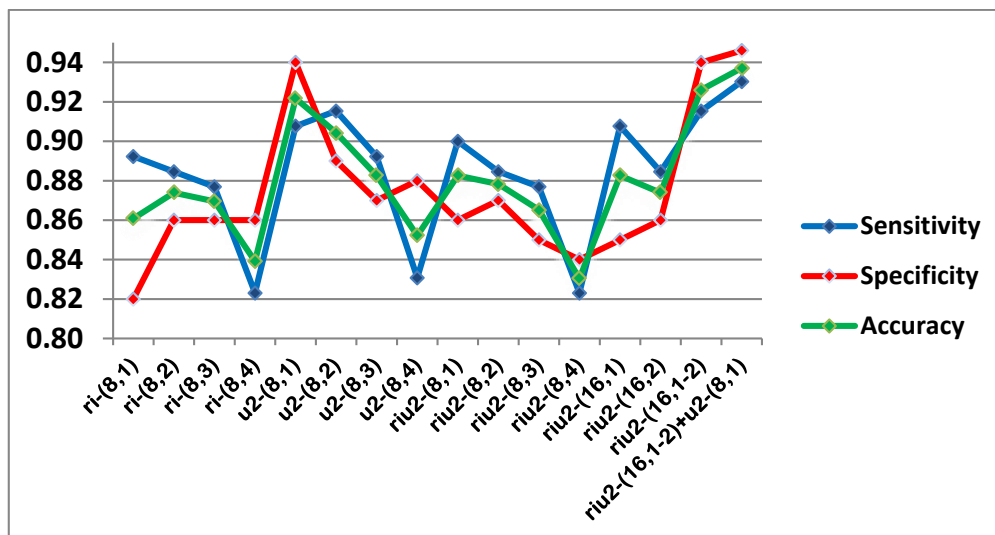
Figure 4.4. Comparison of sensitivity, specificity and accuracy for various forms of LBPs calculated using different radii and samples for k-NN classifier.
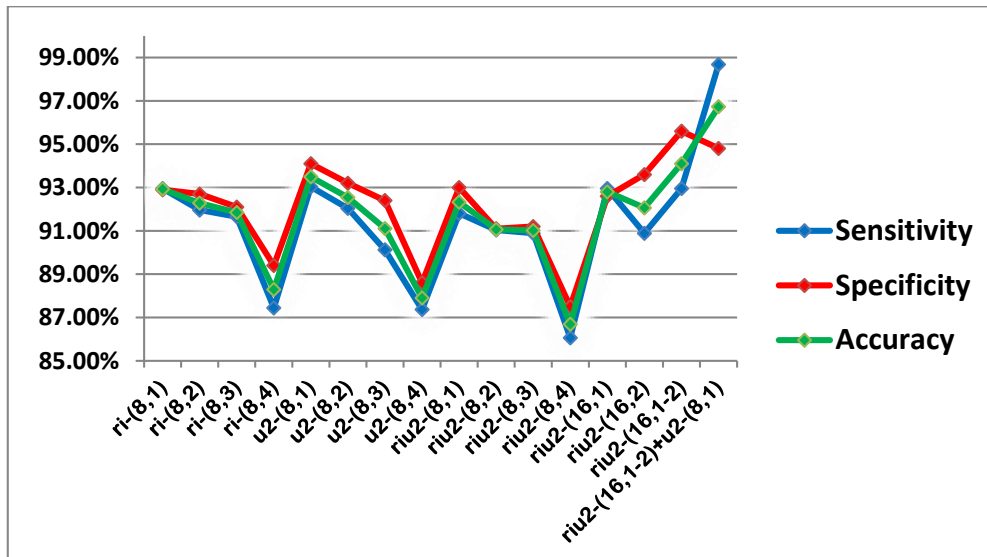
Figure 4.5. Comparison of sensitivity, specificity and accuracy for various forms of LBPs calculated using different radii and samples for RBF neural network.

In this chapter, it has been found that the proposed method has the potential to be used for lesion detection, as measured in terms of sensitivity, specificity, PPV and accuracy. The results obtained for the k-NN classifier were 93.03%, 94.60%, 95.74% and 93.71% for sensitivity,

specificity, PPV and accuracy respectively, while for the RBF neural network the results for
sensitivity, specificity, PPV and accuracy were 98.68%, 94.81%, 94.94% and 96.73%
respectively. Based on these results, the RBF neural network gives better overall performance
than the k-NN classifier. Table 4.3 shows the experimental results in terms of sensitivity,
specificity, PPV, and accuracy.

Table 4.3 Performance of region classification based on classifiers

Classifier	Sen (%)	Spec (%)	FNR (%)	FPR (%)	PPV (%)	Acc (%)
KNN	93.03%	94.60%	6.97%	5.40%	95.74%	93.71%
RBF-NN	98.68%	94.81%	1.32%	5.19%	94.94%	96.73%

For the sake of illustration, a recently published technique for the detection of exudate regions
based on texture information (Akram et al., 2013a) has been implemented and applied on the
same dataset. A comparison has been carried out in terms of sensitivity, specificity and
accuracy. The combination of the $LBP_{8,1}^{u2}$, $LBP_{16,1}^{riu2}$ and $LBP_{16,2}^{riu2}$ of ROIs with different
versions and parameters are extracted for the proposed method. Meanwhile gray-level features
based on gray-level intensities inside the candidate regions combined with statistical features
such as entropy, energy and moments were used in Akram et al. (2013a) work.

The use of the RBF neural network in the present study achieved performance results of
98.68%, 94.81%, and 96.73% respectively as compared to Akram et al. (2013a) who achieved
classification accuracy rates of 81.55%, 81.80%, and 79.27% respectively using SVM and
90.63%, 88.70%, 88.93% with the GMM classifier. The proposed system gives higher values
with the same dataset, which makes it suitable for an automated medical system for grading
exudates in DR (Akram et al., 2013a). Figure 4.6 shows a comparison between the performance
of Akram et al. (2013a) system and the proposed system in terms of sensitivity, specificity and
accuracy.

Since this is a preliminary study of the proposed approach, many improvements could be made
to increase the performance of the algorithm. In feature extraction, only LBP texture features
were applied. A combination of these with other texture features may improve the system.
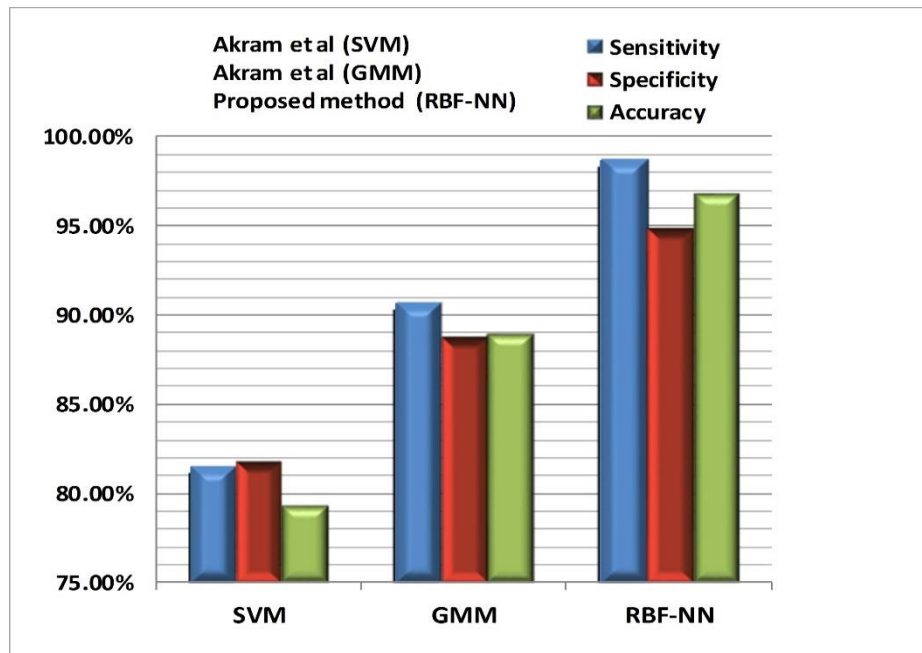
Figure 4.6. Comparison of the sensitivity, specificity and accuracy between Akram et al. (2013a) system and the proposed system

4.4 Summary and Conclusions

In this chapter, a new LBP-based feature extraction technique has been applied for classification. Based on experiments, the system has shown good ability in the detection of abnormalities associated with DR. Exudates are signs of DR and are not easy to detect due to other normal retinal characteristics with similar features such as contrast, intensity levels, colour and shape. When digital fundus images are captured, using cameras with uneven illumination, the detection problem becomes even more difficult. However, it has been revealed that LBP texture features offer an efficient solution to overcome these issues.

The experiments conducted in this study show that the proposed system achieves significant results for sensitivity of 98.68%, specificity of 94.81%, PPV of 94.94% and accuracy of 96.73%. This improvement is due to the LBP-based feature extraction algorithms proposed in this thesis. The algorithm that shows the best results is RBF-NN when used to build the classification model with an accuracy rate of 96.73%. Part of this work has already been published (Omar et al., 2016).

Related work on exudate detection and the classification of multi-label learning models for improving retinal image classification is discussed in detail in the following chapter.

5. A MULTI-LABEL LEARNING MODEL FOR IMPROVING RETINAL IMAGE CLASSIFICATION FOR THE DIAGNOSIS OF DIABETIC RETINOPATHY

5.1 Introduction

Currently the world faces a challenge of an epidemic disease called Diabetic Macular Edema (DME). According to estimates from the World Health Organization, the total number of people in the world with DME will increase to 360 million by the year 2030 (Organization, 2016). DME with extended suffering may lead to diabetes, which involves on the destruction of the blood vessels of the retina. DME is usually one of the main causes of blindness and visual loss (Association, 2007, Control and Prevention, 2011a, Lim et al., 2011, van Ginneken and Novak, 2012). DME is normally detected and diagnosed when fluid leaks from the blood vessels inside the region of the macula. The leak is produced by the breakdown of endothelial junctions in blood vessels or microaneurysms. Lipid deposits stored in the retina resulting from the outflow are termed exudates. Exudates appear as white or yellowish intraregional deposits in retinal images (Wu et al., 2013). Retina has more information provided for instance, the quality and metric ethnicity, patient age, type of lesion and patient gender at image capture.

Segmented retinal images are usually classified as normal and abnormal retinal image by extracting region-based textural characteristics (Akram et al., 2013a). However, almost all of the approaches currently used focus on the correct diagnosis of abnormal and normal images (Omar et al., 2014). However, in real world scenarios, the ophthalmologists request not only the patient experience and knowledge while examining the retina, but also they need to know about patient history such as patient's ethnicity, age and disease stratification.

Analysing retinal fundus images requires enhanced skills and it is also challenging ophthalmologists to distinguish between similar diseases of the retina. Figure 5.1 shows some retinal images from HEI-MED dataset (Giancardo et al., 2012). The present study aims to tackle these difficulties using a relatively recently developed machine learning framework called multi-label classification (Tahir et al., 2016, Montañes et al., 2014). In this approach, each image can be assigned one or more labels. This, however, is extremely challenging due to the fact that multi-label classifiers have to predict a varying number of outputs for each image. In this chapter, an instance-based multi-label learning model (ML-kNN), multi-label

support vector machine (ML-rank SVM), multi-label neural network using radial base function (MLNN-RBF) and back-propagation multi-label learning (BPNN-MLL) are investigated as classification models. To the best of our knowledge, this is the first work to investigate multi-label learning in order to improve retinal image classification in diagnosis of diabetic retinopathy. Experiments are conducted on the HEI-MED dataset, which consists of 169 images and 2 labels where the first label describes normal or abnormal regions and the second label refers to old, medium or young age factors. Six evaluation measures are applied to assess the performance of the proposed technique; namely ranking loss, Hamming loss, coverage, one-error, average precision and classification accuracy. Nevertheless, some important challenges are associated with this process. Firstly, when clinicians examine retinal images in ophthalmic clinics, they only provide a normal textual explanation for the entire retinal image. The explanation contains stratification annotations with additional terms to describe structures revealed in the image. The stratification terms only refer to certain parts instead of the entire retinal image.

In this chapter, a multi-label learning algorithm ML-kNN, is applied to construct a classification model for the diagnosis of DR in retinal images (Omar et al., 2017). ML-kNN produces better results than a k-NN method based on three performance criteria; namely, Hamming loss, average precision, and classification accuracy. The results indicate significant increases in performance when compared with previous approaches.

The chapter is structured as follows. In Section 5.2, relevant work is discussed, followed by a description of multi-label k-nearest neighbour classification in Section 5.3. Section 5.4 presents the details of the experiments and results. Finally, conclusions are given in Section 5.5.
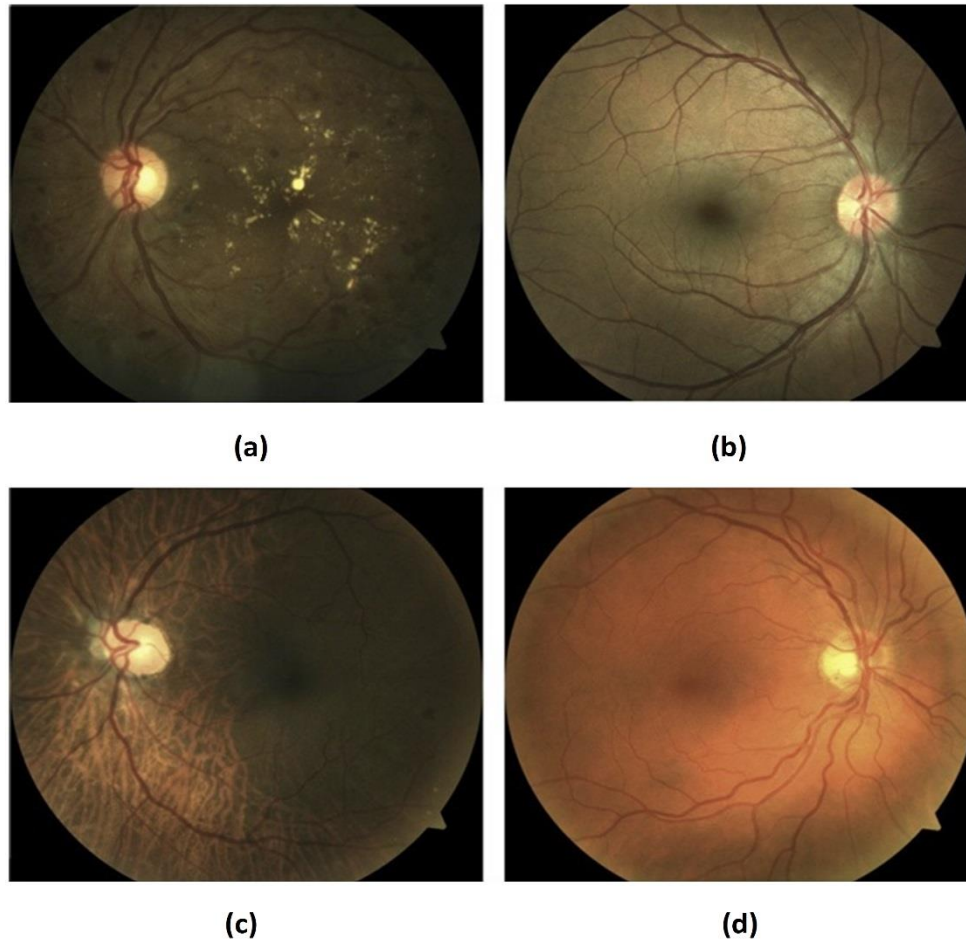
Figure 5.1. Samples of retinal images samples of HEI-MED dataset: (a) African-American patient displaying pure exudate; (b) Hispanic patient without symptoms of diabetic macular edema; (c) African-American patient displaying small exudates and blood vessels under the pigmentation epithelium layer; (d) Caucasian patient with no symptoms of diabetic macular edema (Giancardo et al., 2012).

5.2 Overview of Multi-label Classifier

Little work has been done that applies multi-label learning to the computer-aided diagnosis of diseases. Existing feature selection methods in the literature focuses only on problem transformation; for instance, first transforming multi-label data into a single label, which is then used to select features using traditional single-label feature selection methods (Shao et al., 2013). Liu et al. (2012) combined multi-label learning with feature selection by setting the threshold value to be 0.5 in order to improve the recognition rate of chronic gastritis. Shao et al. (2013) proposed a hybrid optimization multi-label feature selection technique to build diagnostic models using evaluation measures. In their work, simulated hill climbing strategies

and genetic algorithms are combined to select the best feature subset. The medical text in the dataset contains a brief free-text summary of patient histories and diagnose which is also labelled with insurance codes. Each case is represented with a bag-of words of the sign history and is related to a subset of 45 labels (for instance, possible diagnoses). A recent study has reported that the use of ReliefF as a score function for evaluating each feature in a label power (LP) set yields successful classification results (SpolaôR et al., 2013). After transforming a multi-label dataset into binary class dataset by counting the number of true positives/negatives, false positives/negatives, and any feature evaluation measure for binary data can then be applied according to the macro-averaged approach (SpolaôR et al., 2013). However, conventional multi-label feature selection techniques require a pre-processing step where multi-label problems are converted into a single label problem. Moreover, Liu et al. (2010) applied multi-label learning (MLL) to the modelling of the coronary heart disease (CHD) in traditional Chinese medicine (TCM). They compared the performance of multi-label k-NN with a classic k-NN classifier on a coronary heart disease dataset.

Multi-label k-NN shows some interesting results in this work and the k-nearest neighbour (k-NN) has already been deemed quite successful in the biomedical field (Zhang and Zhou, 2007). As an extreme of slight distance classifiers, k-NN is easy to use, efficient and simple. On the other hand, when its label determines a test image, the k-NN can only make predictions on at a time; for instance, classifying an exudate into one category in diabetic disease. However, in the medical domain, more information about patients may be available, such as ethnicity, elliptical local vessel density (ELVD) quality, DME diagnosis, diabetes type and age factors and number of labels such as DME diagnosis and age. In order to achieve this, a multi-label learning model such as ML-kNN can be suggested. To the best of our knowledge, this is the first study to investigate the use of multi-label learning classification for this problem. The results reported in this chapter can be used as baseline results. A multi-label learning problem as suggested by Lee et al. (2016b) to transform problematic skin biopsy features was the first attempt to solve skin biopsy annotation problems.

In the present study, the multi-label learning model, ML-kNN, is used as a classification model to detect the exudate lesions with patient's age factor of retinal images. Moreover, the local binary pattern multi-scale is used to extract the retinal features. The ML-kNN approach proposed here can be used as a baseline results for future comparison with the other algorithms.

The proposed method evaluated with a real dataset from the Hamilton Eye Institute Macular Edema Dataset (HEI-MED) (Giancardo et al., 2012). The results of the evaluation show that the suggested system can efficiently annotate the terms associated with diabetic retinopathy.

5.3 Multi-label Classification for DME Diagnosis and Patients Age Factor

Extending our previous work of disease classification in two-class problem to the multi-label machine learning of classification model problem by considering the diabetic macular edema diagnosis with other factors such as patient ages or races. Therefore it is important to improve techniques in terms of the computation for automatically identifying other important retinal image features such as patient gender, type of diabetes and age of the patient at image capture (Giancardo et al., 2012). Nevertheless, there are some important challenges. Firstly, in ophthalmic clinics, when clinicians examine retinal image, they only provide normal text explanation for the entire retinal image. The explanation contains normal stratification annotation terms and some associated words to express about the structures revealed by retinal image. Though, the stratification terms is only reflecting certain parts of region instead of the entire retinal image.

Additional challenge is that even though for the same term, its corresponding local regions may be meaningfully mixed in shape, size, inner structure, texture, lightening or the correlation between retinal structures with different terms (Visser et al., 2003). With these challenges are creating the task more problematic with traditional machine learning ones.

The hospitals provide effort for the telemedicine system are generally placed in the Mid-South of the USA, where the mix of ethnic groups and the pigment of the retinal image covers the range usually originate in various people. It is significant to highlight those characteristics for the reason that the presence of the retinal image differs significantly based on the coloration of the retinal image pigmentation, which is associated to the retinal colour and ethnic group (Giancardo et al., 2012).

The multiple ocular diseases detection is not yet overcome the problem in context of health imaging analysis. In this proposed work, the suggested system adventures the medical problem of simultaneously identifying the leading multiple ocular diseases depend on ML-kNN multi-label probabilistic multi-label learning (Zhang et al., 2012). After selecting appropriate

features, multi-label classifiers would participate in the classification tasks. In order to eliminate the bias of classifiers, ML-kNN multi-label classifiers, is employed in the experiment.

5.3.1 Pre-processing and Feature Extraction

After image pre-processing and enhancement using a probability map of exudates which described in the pre-processing stage (Giancardo et al., 2012). The technique suggested for the DME is based on a single feature vector classification which is generated for each image, and the features are extracted from LBPs multi-scale texture features (Omar et al., 2016). By combining the LBP multi-scale features, 32 texture features per image are obtained. Figure 5.2 shows the main steps of the proposed system, where the previous approach used for pre-processing and feature extraction was mainly followed (Omar et al., 2016).

5.3.2 Multi-label k-nearest Neighbour (ML-kNN)

This technique originates from the famous k-nearest neighbour (k-NN) algorithm proposed by (Keller et al., 1985). The basis for ML-kNN is that a test instance label can be influenced by the number of neighbours that have similar labels (Chiang et al., 2012). Consider a test instance x with label set $Y(x) \subseteq M$, where $M = \{l_1, \ldots, l_m\}$ denotes the complete set of labels. ML-kNN first finds the k-NN in the training dataset. Afterwards, the algorithm produces a histogram of the total number of neighbours from each class, which is a random variable (R). Lastly, the maximum a *posteriori* principle is utilized to establish the label set for the test sample. The posterior priority of $l_i \in M$ is given by:

$$\frac{P(l_i \in Y(x) \setminus R = r) = P(R = r \setminus l_i \in Y(x)) \times P(i \in Y(x))}{P(R = r)} \qquad 5.1$$

Then, for each label $l_i \in M$, ML-kNN builds a classifier h_i using the rule $h_i(x) = 1, hi(x)$, if $P(l_i \in Y(x) \setminus R = r) > P(l_i \notin Y(x) \setminus R = r)$, and $h_i(x) = 0$ otherwise $h_i(x) = 1$ indicates that l_i is relevant to x, while 0 means that l_i is not relevant. Training data is used in advance to estimate the prior and likelihood probabilities. In summary, ML-kNN consists of two main steps as follows:

1. k-nearest neighbours in the training set are detected for each test instance and then statistical information gained from the set of labels of these neighbouring instances is utilized to obtain a set of labels with maximum a *posteriori* probability.
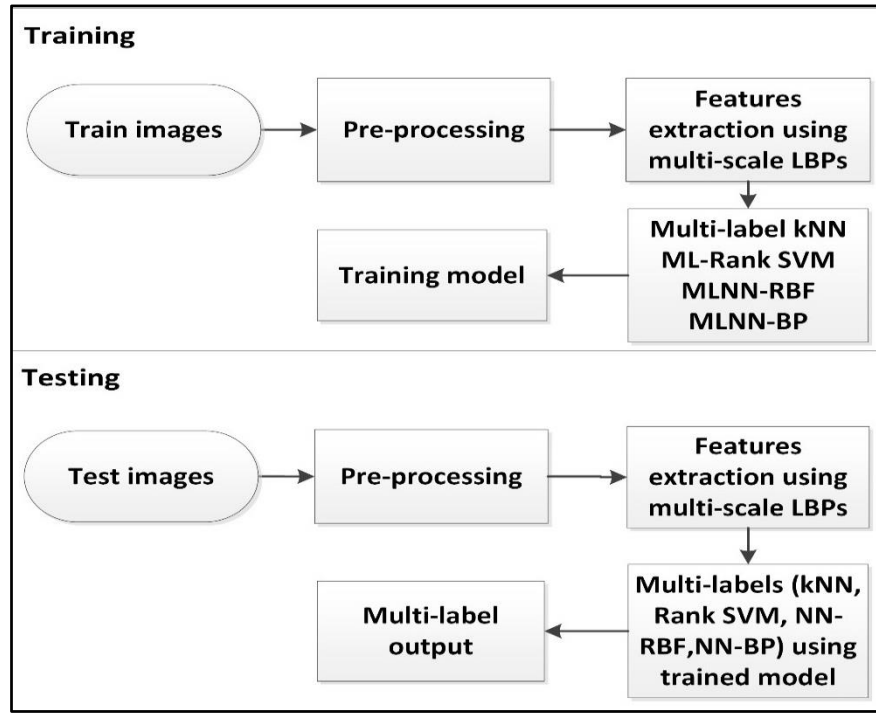
Figure 5.2. Main steps of the proposed system (Here ML-kNN classifier is investigated for proof of concept but any good multi-label classifier can be used).

2. ML-kNN has been shown to perform well in many applications including in bioinformatics, text categorization and music classification (Hiillermeier, 2009, Tahir et al., 2012, Tahir et al., 2016, Lee et al., 2016a).

5.3.3 Comparison of Methods

In this section, ML-kNN and the following multi-label, and other previous methods are also compared to:

- ML-rank SVM (Boutell et al., 2004) is derived from the principle of the famous support vector machine algorithm. This is also a multi-label classifier. As an algorithm adaptation, rank-SVM trains a collection of SVMs, minimizing the ranking loss and

multi-label evaluation criterion. Another common property of SVM is the possibility to use kernels rather than linear dot products.

- A multi-label neural network algorithm named MLNN-RBF multi-label neural network radial basis function is proposed which is derived from the popular traditional radial basis function (NN-RBF) methods (Bishop, 1995).

- MLNN-BP is another classifier investigated in this study is based on the principle of the famous neural network back propagation algorithm (Zhang and Zhou, 2014). The introduction of a new error function based on ranking loss is the main novelty.

Table 5.1 Characteristics of HEI-MED multi-labels dataset. QM = quality metric (Giancardo et al., 2012).

DME		ELVD QM	
Negative	115 (68 %)	Poor (QM < 0.5)	14 (8 %)
Positive	54 (32 %)	Good (0.5 > QM < 0.8)	31 (18 %)
		Excellent (QM > 0.8)	124 (74 %)
Ethnicity		Patient's age	
African	104 (62 %)	Age < 43	25 (15 %)
Caucasian	42 (25 %)	43 < age < 61	105 (62 %)
Hispanic	19 (11 %)	age > 61	39 (23 %)
Unknown	4 (2 %)		

5.4 Experiments and Results

5.4.1 The HEI-MED Dataset

This dataset consists of 169 retinal images along with some other information such as ethnicity, ELVD quality, DME diagnosis, diabetes type and patient age. These characteristics are summarised in Table 5.1. This chapter focuses on DME diagnosis and patient age (see

Table 5.2).

Table 5.2 Multi-labels information for DME diagnosis and patient's age.

Label	Abnormal	Normal	Old	Medium	Young
Normal Old	-1	1	1	-1	-1
Normal Medium	-1	1	-1	1	-1
Normal Young	-1	1	-1	-1	1
Abnormal Old	1	-1	1	-1	-1
Abnormal Medium	1	-1	-1	1	-1
Abnormal Young	1	-1	-1	-1	1

5.4.2 Evaluation Measures

The following six evaluation measures are applied, which are used widely in assessing multi-label classification.

- Hamming loss (HL): This estimates the fraction of labels that are misclassified.
- One error (OE): This calculates the label with the maximum probability of not being predicted.
- Coverage (C): This calculates the mean distance to find the appropriate label for the given image.
- Ranking loss (RL): The average fraction calculation of label pairs which are reversely ordered for a given image.
- Average precision (AP): The average fraction of labels ranked above a particular label $y \in Y$ is calculated, which essentially in Y.
- Classification accuracy (CA): This requires the actual set of labels to be an exact match of the predicted set of labels.

5.5 Results and Discussion

In this section, the results of the multi-label classification of diseases and patient ages are shown and discussed. Four multi-label classifiers are investigated (ML-kNN, ML-rank SVM, MLNN-RBF and MLNN-BP). Five-fold cross-validation is applied for evaluation.

5.5.1 Comparison of Performance of Different Multi-label Learning Algorithms

DME diagnosis and patient age were selected as labels and five classes were used to build the model. Six evaluation parameters obtained using ML-kNN, ML-rank SVM, ML-NNRBF and ML-NNBP algorithms were compared. As indicated in Table 5.3, the highest average precision was 86.1%, obtained by ML-kNN, and the lowest average precision was 74.6%, obtained using ML-rank SVM. Meanwhile the highest classification accuracy was 80.8%, obtained by ML-NNRBF, and the lowest was 69.8%, obtained using ML-NNBP. For the indicators of one-error and ranking loss, the values obtained using the ML-kNN algorithm were lowest at 0.130 and 0.173 respectively, whereas, the lowest value of coverage was 0.151 using the ML-rank SVM algorithm. In summary, the results obtained using the ML-kNN algorithm were the most accurate.

5.5.2 Comparison of Performance of Multi-label Learning and Classic Algorithms

Table 5.3 shows the results using ML-kNN, ML-rank SVM, ML-NNRBF and ML-NNBP which are compared with their classic classifiers using six evaluations metrics. For Hamming loss (HL), which represents the percentage of labels that are misclassified, the results are around 0.195 using ML-kNN and the ranking loss (RL) was 17.3%. It should be noted that, when the values of HL and RL are lower, performance is better. It is observed from the table that values of average precision and classification accuracy of around 86.1% and 75.4% respectively are obtained using ML-kNN, which is significantly superior to the values of Hamming loss of 0.266 and ranking loss of 0.585, whereas the average precision and classification accuracy of around for the classic k-NN classifier were 56.6% and 66.7% respectively. Future work will investigate other state-of-the-art algorithms such as stacked kernel discriminant analysis (KDA) and RAKEL ((RAndom k-labEL) (Caicedo et al., 2009).

CHAPTER 5: A MULTI-LABEL LEARNING MODEL FOR IMPROVING RETINAL IMAGE CLASSIFICATION FOR THE DIAGNOSIS OF DIABETIC RETINOPATHY

Figure 5.3, Figure 5.4 and Figure 5.5 show the performance of the ML-kNN and k-NN classifiers using varying values of k with Hamming loss, average precision and classification accuracy reported. It is observed that best performance is obtained for k = 10. In summary, the results clearly indicate the utility of employing multi-label classifiers for retinal image classification. Significantly enhanced performance results were obtained using the proposed multi-label model.

Table 5.3 Performance of each compared algorithm (mean_std) on HEI-MED dataset.
(A descending arrow means the lower the better, and an ascending arrow the higher the better).

	Compared Algorithms	Evaluation Criteria					
		Hamming Loss ↓	One-error ↓	Coverage ↓	Ranking Loss ↓	Average Precision ↑	Accuracy ↑
Proposed Multi-label Methods	ML-kNN	0.195±0.017	0.130±0.045	0.199±0.106	0.173±0.030	0.861±0.021	0.754±0.005
	ML-rankSVM	0.211±0.009	0.358±0.226	0.151±0.464	0.199±0.030	0.746±0.098	0.725±0.007
	MLNN-RBF	0.196±0.019	0.345±0.209	0.197±0.038	0.197±0.038	0.755±0.089	0.808±0.009
	MLNN-BP	0.170±0.021	0.319±0.003	0.217±0.089	0.275±0.010	0.760±0.004	0.698±0.020
Previous Methods	k-NN Montañes et al. (2014)	0.266±0.047	0.585±0.051	0.201±0.195	0.585±0.051	0.566±0.036	0.667±0.026
	rankSVM Boutell et al. (2004)	0.252±0.056	0.633±0.012	0.225±0.063	0.633±0.012	0.546±0.015	0.684±0.022
	NN-RBF Bishop (1995)	0.220±0.076	0.568±0.033	0.177±0.158	0.231±0.028	0.649±0.023	0.734±0.007
	NN-BP Zhang and Zhou (2014)	0.350±0.004	0.567±0.091	0.567±0.091	0.192±0.022	0.657±0.049	0.677±0.025
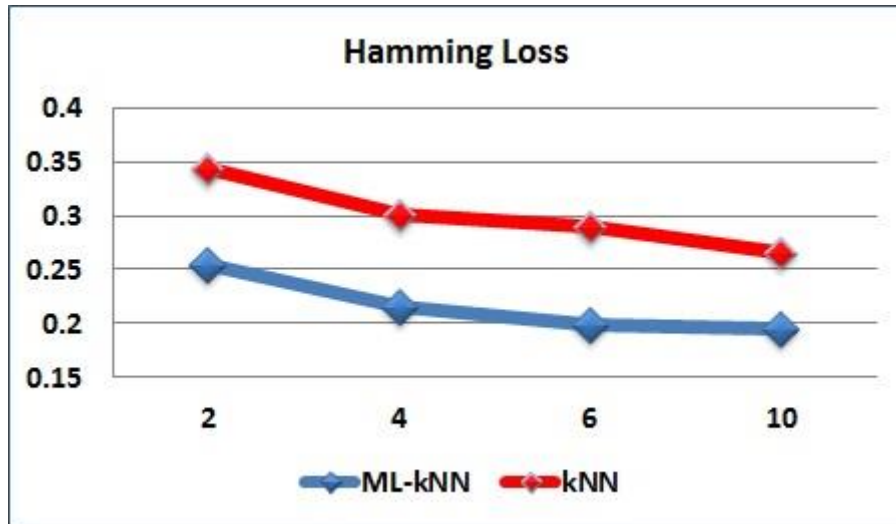
Figure 5.3. ML-kNN and k-NN with different values of k. Hamming loss is used as an evaluation criterion.

5.6 Conclusion

In this chapter, a multi-label model for multiple DME disease diagnosis and patient age identification has been proposed. The proposed multi-label model can learn simultaneously from multiple labels such as DME disease diagnosis and patient age.
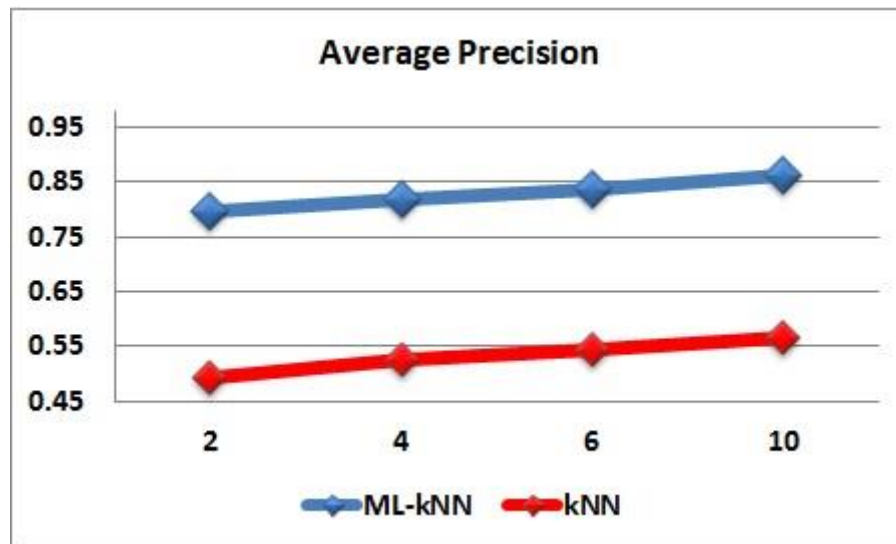
Figure 5.4. ML-kNN and k-NN with different values of k. Average precision is used as an evaluation criterion.
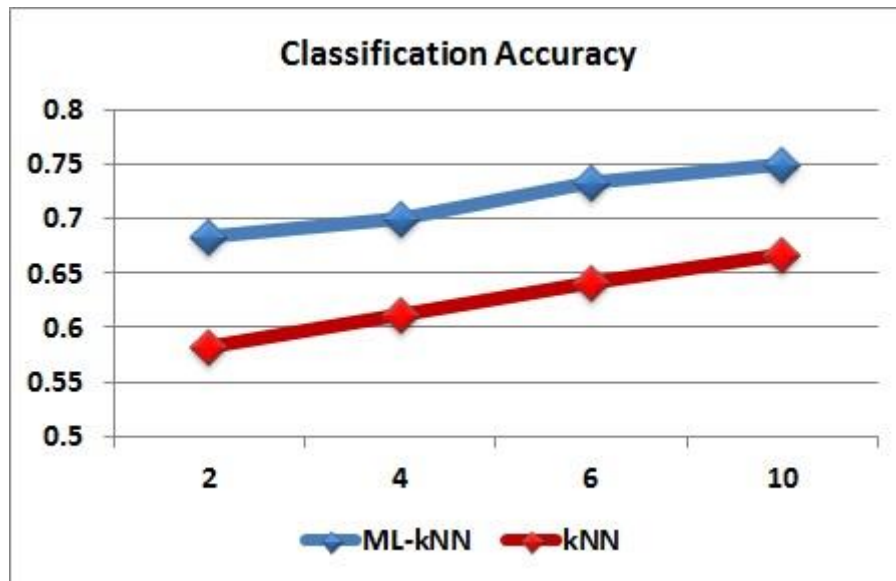
Figure 5.5. Classification accuracy for ML-kNN and k-NN with different values of k.

This type of screening of multiple diseases is highly adapted to the biomedical field diagnosis because patients may possibly have two or three different diseases with its factor in the same time.

The next chapter presents the proposed bag-of-features approach for the detection of multiple classes of exudates and drusen (Omar et al., 2017).

6. EXUDATE AND DRUSEN DETECTION IN RETINAL IMAGES USING BAGGED COLOUR VECTOR ANGLES AND LOCAL BINARY PATTERNS

6.1 Introduction

According to the World Health Organization (WHO), it is expected that around 300 million persons will have diabetes by 2025 (Guariguata et al., 2014, da Rocha Fernandes et al., 2016, Collaboration, 2016). Medical image analysis has a major role in screening for the early stages of different diseases (Kanski and Bowling, 2011). Various computerised care schemes have been developed in the medical field. Age-related macular degeneration (AMD) and diabetic retinopathy (DR) are chronic progressive diseases. In the initial stages, DR is categorised by small bright lesions known as exudates which appear as reflective, yellowish, bright or white-coloured lesions in retinal images (van Grinsven et al., 2013). AMD is mostly categorised by yellowish deposits of variable size in retinal fundus images which are called drusen (van Grinsven et al., 2013). DR and AMD are primary reasons for blindness in developing and developed countries (Sánchez et al., 2008). Permanent damage results to the eyes; therefore, early diagnosis and detection are required to decrease the severity of damage, and degree of vision loss and to save time and number of hospital visits (Nugroho et al., 2015). Exudates and drusen look similar. This is a potential cause of problems for computer-aided diagnosis (CAD) tools and research. CAD is required to support the discrimination between bright lesions (Zheng et al., 2013b, Khalid et al., 2017). Therefore, distinguishing between them is a great concern in automatic CAD systems. To ensure the early detection of these diseases, the diagnosis of both DR and AMD via analysis using colour fundus retinal images is suggested by various national authorities (Karnon et al., 2008, Nagi et al., 2009). The proposed scheme combines intelligent computation systems and pattern recognition technologies with machine learning methods (Osareh et al., 2009b).

In this work, an automatic classification framework is proposed which can distinguish between bright lesions containing exudates or drusen. The technique adopted is the bag of features approach (BoF) in order to classify exudates, drusen and normal characteristics in retinal images. The main advantage of this technique is that the commonly used segmentation stage in traditional techniques, which includes the removal of the optic disc or blood vessel

structures, is not required here. In addition, the proposed technique achieves good performance
when compared with state-of-the-art techniques in the literature. The system relies on bagged
colour and textural features. The rest of the work is organized as follows. Current techniques
of retinal image discrimination and classification are reviewed in section 6.2. Section 6.3
describes the proposed scheme whereas section 6.4 provides a discussion of the experimental
results obtained. Finally, concluding the remarks are provided in section 6.5.

6.2 Related Work

There has been little research devoted to the classification of retinal image lesions into more
than one disease or class, such as exudates and drusen, as shown in Figure 6.2 (van Grinsven
et al., 2013). The most general strategy used in previous techniques was focused on a pre-
processing step, detection of candidate regions feature extraction and retinal lesion
classification into either abnormal or normal using supervised learning classification (Akram
et al., 2013a, Sidibé et al., 2015). In addition, these of AM-FM and statistical features has been
attempted for classification (Agurto et al., 2011). In addition, the features of the macula which
is particularly prone to disease, for example leading to microaneurysms, drusen and exudates,
are of great interest for the automatic diagnosis of eye diseases (Chaum et al., 2008). Research
carried out by Fleming et al. (2007), Niemeijer et al. (2007a), Agurto et al. (2011), Deepak and
Sivaswamy (2012) and Sánchez et al. (2012) explain how bright lesions are extracted when a
segmentation process is applied. However, due to its shape, the fundus image exhibits high
illumination in its central side, whereas the boundaries are dark. Uneven brightness, low
contrast, the small size of lesions and the existence of other objects in the image such as the
optic disc make it challenging to detect lesions such as drusen and exudates accurately.

For this reason, the techniques used still suffer from the absence of precise techniques for
retinal lesion detection. Detecting red and dark lesions in retinal images is still a challenging
task as well. Many of the techniques suggested in previous work focus on the detection of a
specific type of lesion like exudates or drusen (van Grinsven et al., 2016). Candidate regions
which overlap with the location of optic disc are automatically rejected in many previous
methods using automatic optic disc detection or optic disc removal techniques (Abramoff and
Niemeijer, 2006, Niemeijer et al., 2009).

Another method to detect exudate lesions based on a neural network (NN) detection was proposed by Hunter et al. (2000). The neural network was trained to discriminate exudates from drusen using patches of sizes 16×16 pixels. To differentiate between the most significant features, the authors presented a feature selection technique using sensitivity measurement. The results achieved a performance accuracy of 91% using 15 retinal fundus images.

A machine learning algorithm has been developed by Niemeijer et al. (2007a) which has the ability to detect retinal images with bright lesions and to distinguish exudates, drusen and cotton-wool spots. The aim of this work was to design and evaluate a system that distinguishes exudates and cotton-wool spots in retinal images and to discriminate them from other lesions (drusen). However, this method is still not sufficiently accurate for detecting faint or small lesions. Previously proposed methods have not yet achieved wide spread acceptance for the screening of both DR and AMD for a number of reasons.

Giancardo et al. (2012) have suggested a method of exudate detection using RGB retinal fundus images. In the pre-processing stage, the normalization of contrast in the green channel image was subjected to morphological reconstruction operations. Furthermore, a hard threshold method was applied for exudate region detection. Subsequently, the Kirsch's edges of non-exudate structures were compared with exudate edges. Wavelet and colour features were extracted, and subsequently features were fed to the SVM, k-NN, Random Forest and Naive Bayes classifiers. The MESSIDOR dataset was used to evaluate the approach. Their results for area under the curve (AUC) were between 0.88 and 0.94 based on the features and dataset involved using the SVM classifier. van Grinsven et al. (2013) suggested a system to automatically distinguish between exudates and drusen. The algorithm initializes by splitting the image into a fixed number of squared blocks (patches). A set of appropriate features were used to differentiate between normal and abnormal lesions as follows. Features of the colour histogram were extracted from the retinal fundus images in the RGB, YCbCr and HSV colour planes. In addition, the Laplacian of Gaussian (LoG) (Hari et al., 2017), histogram of oriented gradients (HoG), granulometry and LBP features were extracted as well. Furthermore, the ada-Boost technique was used for feature selection, where the selected features were reduced to 24- and 32-dimensional feature vectors separately. Features were selected empirically by adopting a class-validation with 5-fold cross-validation. Then, a BoF method was used for image classification purposes. Similarity measures were used to help retrieve images, such as the L2-

norm, squared chord distance and L1-norm. However, the best results were achieved using the weighted squared chord, whereas the nearest neighbour technique was applied using the distance as a similarity metric for classification purposes. Three different databases including MESSIDOR, STARE, and EUGENDA8 with a total of 415 images were used. They created two sets of databases, each further divided into training and testing sets. The testing set was similar to set A and set B. Precision results of 76% and an area under the curve (AUC) of 9% respectively were achieved for retrieval and classification. From our previous work, results shown that the multi-scale textual features in the LBP approach is beneficial for discriminating exudate lesions (Omar et al., 2016).

Other techniques have focused on the identification of either drusen or exudates such as (Sánchez et al., 2009, Smith et al., 2010, Mora et al., 2011, Agurto et al., 2011, 2012, Akram and Khan, 2012, Sundaresan et al., 2015, Omar et al., 2016). In these approaches, the focus was to discriminate normal retinas from abnormal ones; for example, consisting either of abnormalities associated with AMD or related to DR disease. Moreover, the datasets for this task contained normal and abnormal retinas of either drusen or exudates, but not all together. Features are also required to discriminate between drusen and exudates, and these need to be more robust since these lesions making distinction more and more challenging.

The present study is concerned with automatic classification using the BoF technique to identify and distinguish between normal retinal images, those containing exudates, and finally those with drusen (three-class classification). This is more challenging from a classification point of view as compared with two-class classification. In particular, the most efficient textural and colour features are combined in the BoF approach. New textural and colour features are presented in this area for efficient and accurate retina lesion detection.

It is particularly claimed that the combination of colour vector angles (CVAs) and local binary patterns (LBPs) in a single codebook in the BoF approach can lead to high classification performance as compared to the use of other textural and colour features. Experimental results demonstrate the efficiency of the proposed technique as well as the superiority of the overall system over state-of-the-art retinal disease detection technique as shown in Table 6.1 (Akram et al., 2013a, Sidibé et al., 2015).

CHAPTER 6: EXUDATE AND DRUSEN DETECTION IN RETINAL IMAGES USING BAGGED COLOUR VECTOR ANGLES AND LOCAL BINARY PATTERNS

Table 6.1 Summary of methods used to discriminate exudates and drusen. This table shows results for image-based criteria. However, * represents a lesion-based criteria. The paper uses more than one dataset, and L: the length of the feature, EX: exudates, Dru: drusen, SE: mean sensitivity, SP: mean specificity, AC: mean accuracy, AUC: Area under curve, FCV: fold cross-validation, LOOCV: leave-one-out cross-validation, NNs: neural networks, k-NN: k-nearest neighbour, SVM: support vector machine, LS: least square, LDA: linear discriminant analysis, LBP: local binary pattern.

Authors	Lesions	Pre-processing	Methodology	Features {L}	Classifica-tion	Dataset		Results			
						Train	Test	SE%	SP%	AC%	AUC
Giancardo et al. (2012)	EX	Image normalization	Colour wavelet decomposition [✓]	Statistical features (Avg, Std, Max, Min, Med) {48}	SVM (LOOCV)	169	. . .	…	…	…	0.94
Akram et al. (2013a)*	Dru	Morphological closing and histogram equalization	Gabor filter banks [✗]	Colour and shape features {10}	LS-SVM	400	. . .	95	98.4	97	…
van Grinsven et al. (2013)	Dru & EX	Mean subtraction	Bag of Words approach [✓]	Histograms, LOG, HOG, LBP, and granulometry {58 × no of patches}	k-NN (5 FCV)	225/379	36	…	…	…	0.9

Omar et al. (2016)*	EX	Image normalization	Multiscale LBP Texture Approach [✗]	Combination of texture features	k-NN and RBF-NN (FCV)	1506	800	98.68	94.81	96.73	…	
Niemeijer et al. (2007b)	Dru & EX	Convolution with 14 digital filters	Bright lesions clustering k-NN [✗]	Shape, colour, contrast, and position {83}	LDA	130	300	95	88	…		0.95
Deepak and Sivaswamy (2012)	EX	Not necessary	Create motion patterns of a circular ROI [✓]	Radon based features {36}	PCA (10 FCV)	367	277	…	…	…		0.92

6.3 Proposed DR and AMD Identification System

This work proposes a technique to identify DR-and AMD-related lesions containing exudates and drusen from among healthy retinal images. The framework of the suggested scheme in the training phase is shown in Figure 6.1. The proposed system consists of several stages at the training stage, namely: patch pre-processing, patch extraction, feature extraction, feature concatenation, codebook generation, histogram building, and classification. First, the retinal fundus image is split into small square patches using the area of the optic disk and macula as location coordinates for the region of interest. Then, textural and colour features are extracted automatically from each patch to differentiate between patches with exudates, drusen and normal patches. Two sets of features, namely LBPs and CVAs are extracted from local patches of the fundus images, concatenated and then used to build a codebook. Once a codebook is formed, the patches of each fundus image are used to form a histogram describing the CVA and LBP features in the whole image.
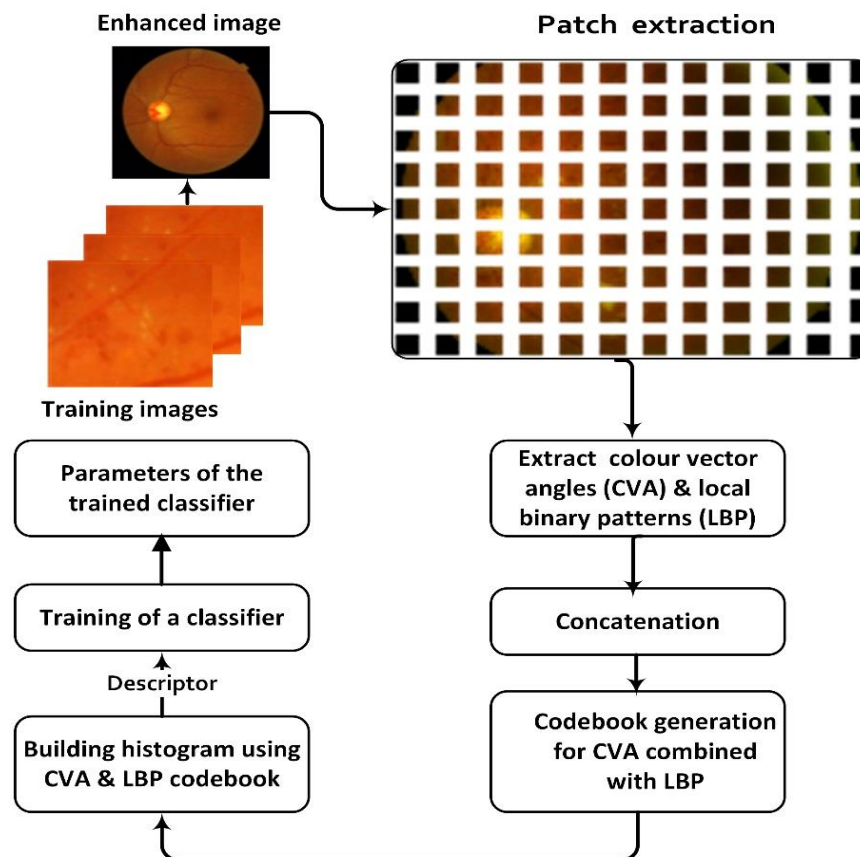
Figure 6.1. Training phase of the proposed system.

6.3.1 Images Used for Patch Extraction

For this work, images were taken from different publically available datasets: DIARETDB0 (Kauppi et al., 2006), DIARETDB1 (Kälviäinen and Uusitalo, 2007), HEI-MED (Giancardo et al., 2012), STARE (Hoover and Goldbaum, 2003), and MESSIDOR (Decencière et al., 2014). The images in the DIARETDB0 and DIARETDB1 datasets were acquired a 50° field of view (FoV) with a resolution of 1500 ×1152 pixels. The images from HEI-MED were acquired by a Zeiss Visucam Pro retinal camera in a resolution of 2196×1958 pixels and with a 45° field of view. Furthermore, images from the STARE dataset were taken with a Top- Con TRV-50 retinal camera at 35° (FoV) and then digitized in a resolution of 605×700 pixels. Images from the MESSIDOR dataset were taken with a Topcon TRC NW6 retinograph at a 45° (FoV) angle and with two resolutions of 1440×960 or 2304×1536 pixels. These images which were of insufficient quality, were macula centred, or had other bright lesions of abnormalities, for instance myelinated nerve fibres or which were not related to the AMD or DR diseases, were discarded from the experiments. The rest of the image set was categorised by experts into one of the group of exudates, drusen and normal images, as shown in Figure 6.2. All images containing either exudates (N=254) or drusen (N=30) as graded by the experts and the normal (N=68) images were randomly selected.
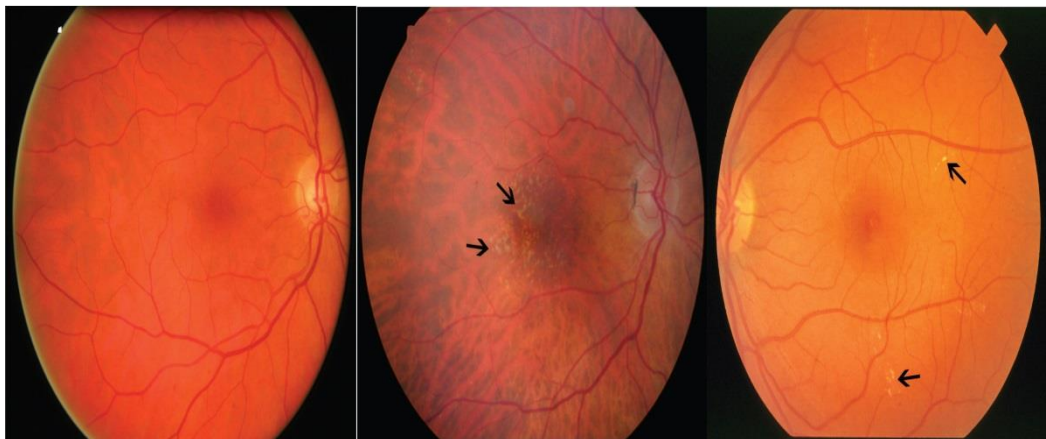
Figure 6.2. Samples of retinal fundus images: (a) normal; (b) with the presence of exudates; and (c) the presence of drusen.

6.3.2 Patch Extraction

Each image is divided into a fixed number of non-overlapping blocks (patches) with a size of 32×32 pixels. Thus, the number of patches may differ from one dataset to another due to differences in resolution. At the training stage, there are two types of patches: the first being normal fundus images, which have been analyzed by optometrists; and the second being abnormal fundus images as marked by four optometrists. In total, 254000 exudate, 900000 drusen and 2040000 normal patches have been used to train the system. This gives an overall total of 3194000 patches used in our experiments.

6.3.3 Patch Level Feature Extraction

In this work, textural and colour features have been extracted from each patch in order to describe retinal lesions efficiently. In particular, it is claimed that a combination of LBP and CVA features in a BoF approach using a single codebook leads to the best classification performance when compared to other features used in the literature in existing state-of-the-art techniques.

6.3.3.1 Local binary patterns (LBPs):

Local binary patterns (LBPs) are used to extract features in different multi-scales such as $LBP_{8,1}^{riu2}$ and $LBP_{8,4}^{riu2}$. The texture descriptor of an LBP is used to extract the features of patches (Pietikäinen et al., 2011). The rotation invariant uniform (riu2) of the LBP is used in this work. The LBP effectively captures small-scale differences in texture and is appropriate for detecting exudates and drusen lesions and the details are described in chapter 4 (Ojala et al., 2002, Omar et al., 2016).

6.3.3.2 Colour vector angle (CVAs):

A vector angle is effective in evaluating colour contrast and can be used for extracting colour features. Colour vector angles (CVAs) have been widely used in edge detection, image hashing and image retrieval (Tang et al., 2013). The CVA is used to identify colour edges because it is insensitive to variations in intensity while being sensitive to differences in hue and saturation, whereas the Euclidean distance fails (Dony and Wesolkowski, 1999).

In this work, CVA is adopted in extracting colour features from retinal fundus images. As the angle calculation needs two colours, a reference colour is generated from $P_{ref} =$

$[R_{ref}, G_{ref}, B_{ref}]^T$, where R_{ref}, G_{ref} and B_{ref} are the means of the red, green and blue components of all pixels. Therefore, for each pixel, the colour vector angle between its RGB vector and P_{ref} is calculated. The advantage of colour vector angle is attributed to its sensitivity to differences in hue. Let $P_1 = [R_1, G_1, B_1]^T$ and $P_2 = [R_2, G_2, B_2]^T$ be the vectors of two colours. The angle Δ between two pixels P_1 and P_2 can be computed by:

$$\Delta = \arcsin \left\{ \left\{ 1 - \frac{(P_1^T P_2)^2}{P_1^T P_1 P_2^T P_2} \right\}^{\frac{1}{2}} \right\}$$

6. 1

where $arcsin$ is the inverse sine operation. Once a matrix of angles Δ is extracted from an image patch, a histogram is built using a certain number of bins. This creates the feature vector corresponding to the CVA.

6.3.4 Codebook Generation and Building the Histogram

At the training stage, a large number of feature vectors are used to generate a codebook, where each feature is extracted from a patch of a training image. The codebook then serves as a dictionary to represent each test image in the form of a histogram, since each patch corresponds to a codeword. The codebook is generated using a concatenation of CVA and LBP features. The K-means method is adopted in this work for generating the centroids (codeword) in this codebook. The idea of codebook generation is that each feature vector extracted from a patch of any training image is used to form a codebook via K-means with a certain number (K) of centroids or codewords (Zhang et al., 2007).

Once the codebook is generated, each patch of a training image is used to extract CVA and LBP features. These features are then concatenated to create a histogram describing the image by using the codebook formed in the training phase. To this end, each patch is assigned a label corresponding to the closest centroid in the codebook according to the Euclidean distance. Based on this codebook, the image is described by the frequency of labels in the form of a histogram. As mentioned earlier, the histogram describes two types of features. Therefore, the final descriptor F_d is a histogram of concatenated CVA and LBP features given by:

$$F_d = [C_{CVA+LBP}]$$

6. 2

where $C_{CVA+LBP}$ represents the combination of CVA and LBP features.

6.3.5 Classification

As mentioned earlier, the input image is represented by a feature vector (descriptor). For the purpose of classification. The retinal images are used in the training stage with assigned labels. Given a number of descriptors, F_d, obtained from medically annotated images, a classifier is trained on three classes: exudates, drusen, and normal. Once trained, the classifier can be used for retinal image diagnosis. Once the codebook is generated and the classifier is trained, the testing phase follows the same steps as shown in Figure 6.3.
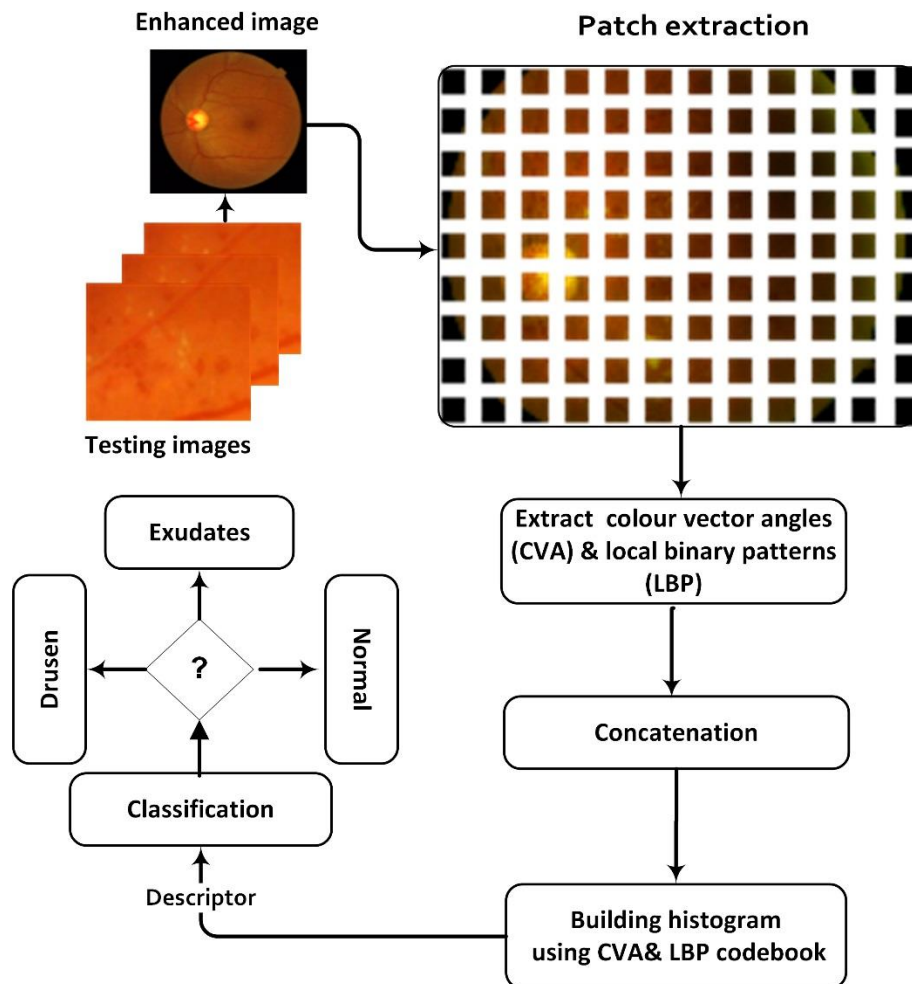
Figure 6.3. The testing phase of the proposed system.

In this study, the k-nearest neighbour (k-NN) classifier is applied at the classification stage using the Euclidean distance as the similarity measure (Niemeijer et al., 2007a). The value of k is set to 4 for the k-NN classifier. Moreover, the support vector machine (SVM)

and neural network (RBF-NN) classifiers have also been used in experiments in the present study (Turnbull and Elkan, 2005, Ricci and Perfetti, 2007).

6.4 Results and Discussion

In this work, 254 images containing exudate lesions, 30 images with drusen and 68 normal images are from five available publicly datasets are tested as displayed in Table 6.2 and as mentioned in section 6.3.1. In this experiments, images were selected from different datasets to evaluate the robustness of the system's performance. Furthermore, the image in the datasets were collected using different cameras, environments and resolutions as shown in Figure 6.2. The images in the three classes are given in Table 6.2.

Table 6.2 Image distribution from public datasets used in the experiments.

Dataset	Exudate	Drusen	Normal
DIARETDB0	50	-	10
DIARETDB1	30	-	4
HEI-MED	30	-	-
STARE	-	30	10
MESSIDOR	144	-	44
Combined	254	30	68

6.4.1 System Analysis

To evaluate the performance of the proposed features for discriminating fundus image lesions using the BoF approach, 10-fold cross-validation is used and it has been chosen because of the possibility of changing its folds. The dataset is divided 10-fold and the dictionaries are learnt with 9 of the folds whereas testing is performed using the remaining fold. To ensure that each retinal image in the dataset is used for training and testing, the classification process is repeated 100 times. As a result, in order to test the system, the average classification performance for 100 different training and testing sessions is stated.

CHAPTER 6: EXUDATE AND DRUSEN DETECTION IN RETINAL IMAGES USING BAGGED COLOUR VECTOR ANGLES AND LOCAL BINARY PATTERNS

The performance of classification for each separate class in a one-vs.-rest method is calculated. Meanwhile, three classes have been used (exudates, drusen and normal images). For instance, all exudate classes are considered as positive labels for the exudate images and all drusen and normal images as negative labels. In the experiments, the size of the multiple dictionaries approach used is varied from 50 to 500. The settings used in the experiments for the process of feature and descriptor extraction are listed in Table 6.3.

Table 6.3 Parameter settings with cross-validation for the system

Features	Parameter	Value
Gran	Codebook size	200
	Patch size	32 × 32
	Bins per patch	15
LBP	Codebook size	200
	Patch size	32 × 32
	Bins per patch	15
CVA	Codebook size	200
	Patch size	32 × 32
	Bins per patch	15
RGB	Codebook size	200
	Patch size	32 × 32
	Bins per patch	15

The proposed system was evaluated by determining the commonly used measures of sensitivity (Sen), specificity (Spec), accuracy (Acc) and area under the curve (AUC), as explained in chapter 3.

6.4.1.1   Experiment I. Exudates -vs.-rest with single features
In this experiment, the performance of the proposed technique in correctly classifying the exudates images is tested. The exudate dataset is used in this experiment as positive

examples, with a total of 254 images, and the rest of the datasets are used as negative examples of drusen and normal images. Here, the performance of each type of features is assessed separately. Other feature that have been adopted in the literature and used the same database that mentioned in section 6.3.1 are also considered, namely: RGB colour features (van Grinsven et al., 2013), granulometry (Ifeachor and Jervis, 2002), and LBP texture features (Omar et al., 2016). The results are given in Table 6.4. It is particularly claimed that the use of colour and textural features leads to high classification performance. This is because the textural features is powerful against monotonic grey-level intensity changes caused by varying illumination and high contrast. Moreover, the colour features is used to identify colour edges because it is insensitive to variations in intensity while being sensitive to differences in hue and saturation whereas Euclidean distance does not have this capability (Dony and Wesolkowski, 1999).

As regards the comparison of different features, the highest sensitivity, specificity and accuracy of 96.29%, 97.71% and 96.86% respectively are achieved using C_{CVA} features at K=200, followed by C_{Gran}, C_{LBP} and C_{RGB} which achieve accuracies of 94.86%, 95.02% and 94.68% respectively. C_{Gran} or C_{RGB} features provide satisfactory results, as expected. In contrast, granulometry gives 94.86%, which is very similar to the results from C_{RGB}. Meanwhile, the removal of the optic disk in a segmentation step is not applied, and it may be confusing for granulometry or C_{RGB} to distinguish between exudates and normal images due to similarity of the optic disk and exudate lesions in terms of intensity characteristics.

As can be seen, the proposed technique using CCVA features appears to be more powerful than those using other features. In addition, it performs well in this experiment in terms of individual features and is able to correctly identify retinal images containing exudates from other images. The results achieved with the proposed bag of features approach using CGran, CLBP, CCVA and CRGB features are given in table 6.4.

6.4.1.2   Experiment II. Drusen-vs.-rest with single features

The second experiment evaluates the performance of the proposed approach in correctly classifying images containing drusen. All 30 drusen images are used as positive instances and all exudate and normal images are used as negative instances. The results achieved

with the proposed C_{Gran}, C_{LBP}, C_{CVA} and C_{RGB} features using the bag-of-features approach are given in Table 6.5.

The C_{LBP} features achieve the highest sensitivity, specificity and accuracy performance of 99.07%, 99.38%, 98.76% respectively at K=200, followed by C_{Gran}, C_{CVA} and C_{RGB} which achieve accuracies of 95.88 %, 97.17 %, and 95.71 % respectively. C_{Gran} and C_{RGB} features achieve reasonably similar satisfactory results as in the first experiment. The results achieved with the proposed bag-of-features approach are given in Table 6.5.

Table 6.4 Exudates-vs-rest classification results with CGran, CLBP, CCVA and CRGB features. The mean and standard deviation measures are used with 10-fold cross-validation.

Measures	C_{Gran}			C_{LBP}			C_{CVA}			C_{RGB}		
	SE%	SP%	AC%	SE%	SP%	AC%	SE%	SP%	AC%	SE%	SP%	AC%
ANN (RBF)	73.44 ±15.47	90.00 ±6.25	91.50 ±4.39	96.83 ±2.52	92.01 ±9.19	95.46 ±3.08	95.82 ±2.68	91.89 ±6.37	96.87 ±2.63	74.78 ±12.41	91.17 ±5.38	91.40 ±6.32
SVM	85.78 ±10.91	83.67 ±16.50	88.84 ±6.44	89.78 ±9.71	91.00 ±6.05	92.78 ±5.37	93.71 ±4.81	95.66 ±3.01	95.87 ±2.63	75.44 ±13.26	78.47 ±11.24	76.56 ±9.65
k-NN	94.63 ±4.63	95.00 ±5.07	94.86 ±3.46	95.85 ±3.65	95.78 ±4.46	95.02 ±3.65	96.29 ±3.00	97.71 ±2.25	96.86 ±2.99	94.04 ±5.91	88.84 ±6.44	94.68 ±3.97

Table 6.5 Drusen-vs-rest classification results with individual CGran, CLBP, CCVA and CRGB features. The mean and standard deviation measures are used with 10-fold cross-validation.

Measures	C_{Gran}			C_{LBP}			C_{CVA}			C_{RGB}		
	SE%	SP%	AC%	SE%	SP%	AC%	SE%	SP%	AC%	SE%	SP%	AC%
ANN (RBF)	73.33 ±26.29	83.57 ±15.81	83.57 ±15.81	94.89 ±4.25	95.87 ±3.01	94.87 ±4.28	92.78 ±7.24	86.67 ±17.21	93.71 ±6.18	73.33 ±30.63	76.67 ±19.00	75.76 ±22.50
SVM	91.70 ±9.04	93.80 ±3.91	90.30 ±5.44	83.33 ±23.57	80.00 ±23.31	86.67 ±17.21	75.10 ±16.35	88.30 ±3.77	92.10 ±4.63	93.50 ±3.63	86.40 ±7.66	88.30 ±2.87
k-NN	95.15 ±4.86	94.89 ±4.25	95.88 ±3.31	99.07 ±1.38	99.38 ±1.18	98.76 ±1.60	96.85 ±2.86	95.46 ±3.96	97.17 ±2.68	93.33 ±7.05	92.78 ±8.24	95.71 ±4.01

6.4.1.3   Experiment III: Normal-vs.-rest with single features

The third experiment investigates the performance of the proposed technique in correctly classifying normal retinal images with no lesions. All 68 normal retinal images are used as positive examples in the dataset and the rest of the exudate and drusen images are used as negative examples. The results accomplished with the proposed bag-of-features approach using C_{Gran}, C_{LBP}, C_{CVA} and C_{RGB} features are given in Table 6.6.

With reference to the comparison of different feature types, the C_{CVA} colour features again achieves the highest levels of sensitivity at 97.40%, specificity at 98.83% and accuracy at 98.21% with K=200, followed by C_{Gran}, C_{LBP} and C_{RGB} which accomplish accuracies of 86.70 %, 97.85%, and 79.64% respectively. The gran and C_{RGB} features achieve not similar results as previously.

Table 6.6 Normal-vs-rest classification results with individual CGran, CLBP, CCVA and CRGB features. The mean and standard deviation measures are used with 10-fold cross-validation.

Measures	C_{Gran}			C_{LBP}			C_{CVA}			C_{RGB}		
	SE%	SP%	AC%	SE%	SP%	AC%	SE%	SP%	AC%	SE%	SP%	AC%
ANN (RBF)	74.67 ±19.15	82.86 ±11.98	87.81 ±20.09	89.74 ±9.22	88.78 ±7.38	85.84 ±13.45	85.84 ±13.45	82.65 ±10.69	87.50 ±21.76	88.30 ±6.27	90.95 ±18.26	90.50 ±12.35
SVM	84.76 ±17.89	86.58 ±10.49	88.43 ±11.36	87.67 ±16.47	87.80 ±12.67	89.67 ±18.08	86.67 ±14.86	91.01 ±5.89	91.43 ±5.05	81.19 ±21.31	83.57 ±15.81	82.38 ±13.05
k-NN	87.68 ±5.89	91.32 ±5.95	86.70 ±12.49	98.87 ±1.96	96.03 ±3.70	97.85 ±2.25	97.40 ±1.98	98.83 ±2.61	98.21 ±1.88	88.50 ±15.96	90.67 ±15.78	79.64 ±32.99

A comparison of the classification results obtained for each of the three classes is shown in Figure 6.4, Figure 6.5 and Figure 6.6. It can be noticed from these figures that the classification performance achieved for the exudate class in Experiment I are slightly lower than those achieved for the drusen class in Experiment II and the normal class in Experiment III.

As an example, for dictionaries with sizes of 50 and 100, it is clear that the accuracy values for the exudate, drusen and normal classes are lower of the three classes compared to the medium dictionary of 200 size. As a result, the method achieves nearly perfect

results for the three classes. However, for larger dictionaries with a size above 200, the results are slightly lower and decreased in terms of accuracy as well as for the means for the three classes, as shown in Table 6.7.

6.4.2 Evaluation of the Proposed Features

In this section, the performance of the different feature types introduced in Section 6.3.3, namely the C_{Gran}, C_{LBP}, C_{CVA} and C_{RGB} features is evaluated. Again, the classification performance using different types of features is evaluated for each individual class as mentioned above. For this comparison, a dictionary of size 200 is used where the higher results are obtained.
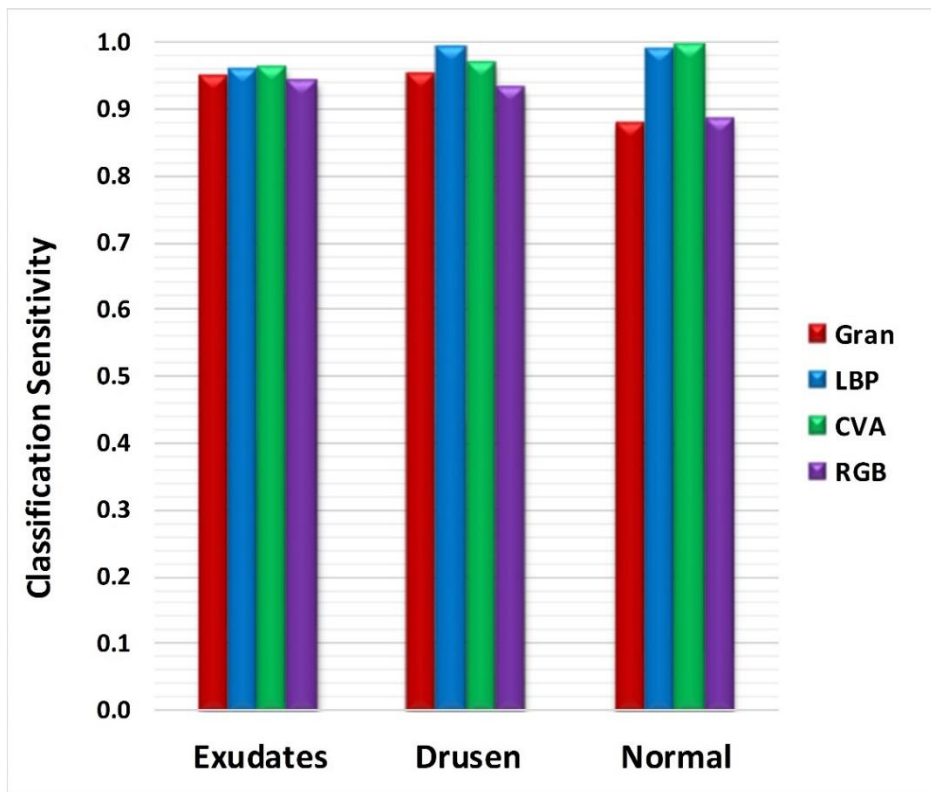
Figure 6.4. Comparison of classification sensitivity with different features.

The results for the experiments are given in Table 6.6 and in Figure 6.4, Figure 6.5 and Figure 6.6. It can be seen from the results that the bag-of-features applied to C_{CVA} colour features performs better than with other feature types. The classification accuracy levels obtained with C_{CVA} colour features are higher than those obtained with other features those their performance are comparable. Accuracy values of 94.86%, 95.02%, 96.86% and 94.68% are obtained with C_{Gran}, C_{LBP}, C_{CVA} and C_{RGB} features respectively for the

exudates class. For the drusen class, the C_{LBP} texture features achieve good results but still slightly below the results obtained with the C_{CVA} colour features. However, for the normal class, the difference is more significant with C_{CVA} colour features. For this class, the use of C_{CVA} features results in a sensitivity of 97.40%, a specificity of 98.83% and an accuracy of 98.21%, while using the C_{LBP} texture features these figures are respectively 98.87 %, 96.03 % and 97.85 %.
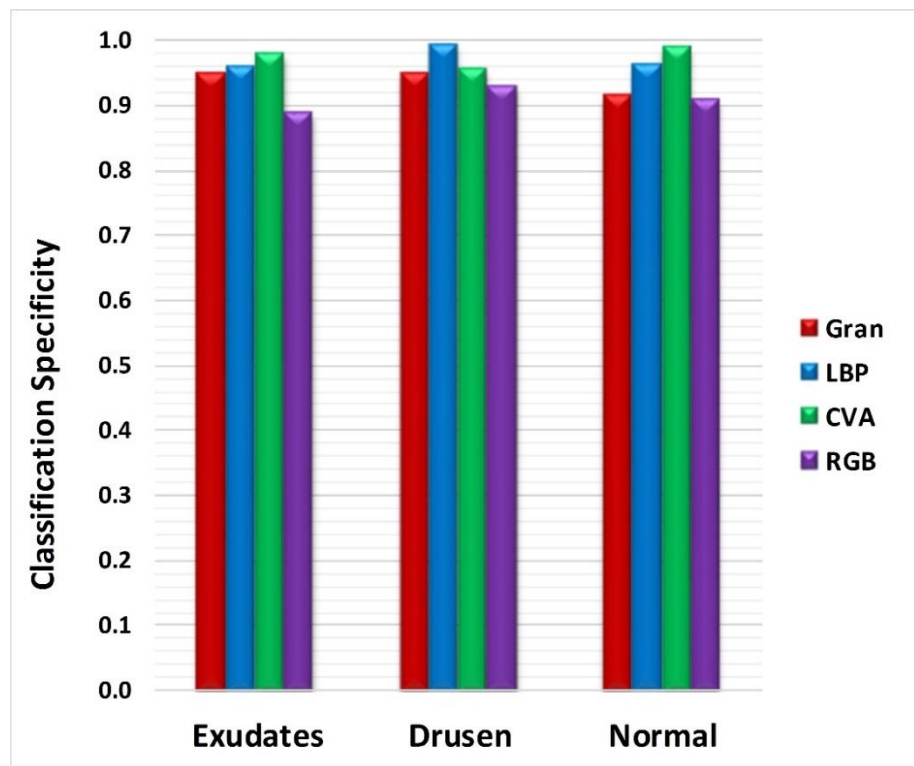
Figure 6.5. Comparison of classification specificity with different features.
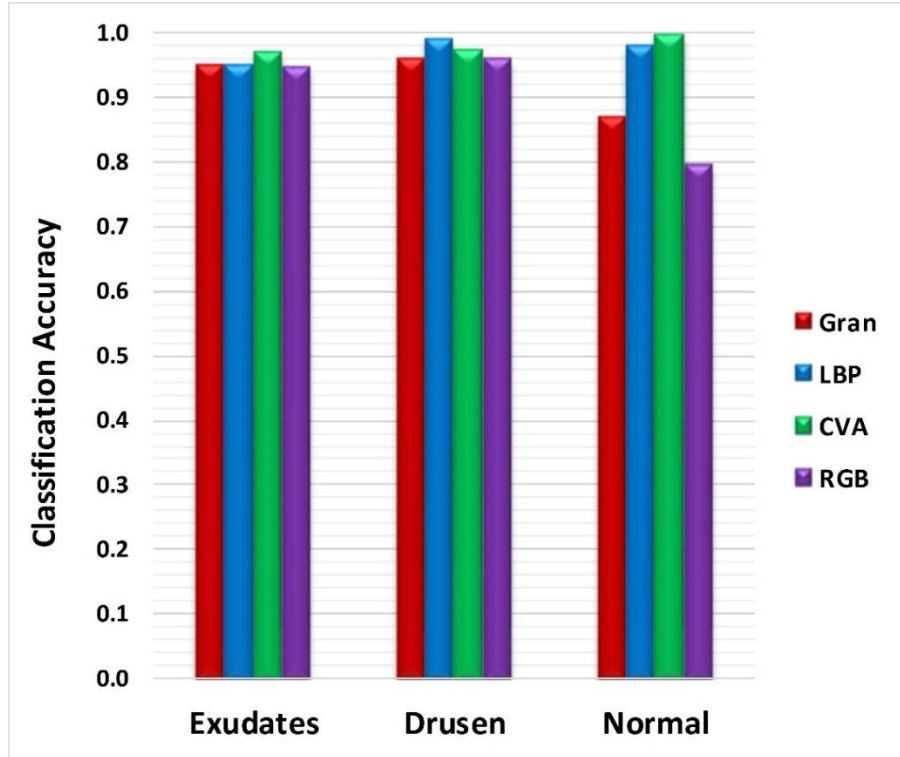
Figure 6.6. Comparison of classification accuracy with different features.

From Figure 6.4, Figure 6.5 and Figure 6.6, it can be concluded that C_{CVA} features perform best among all features types for all three classes. In particular, for the difficult class of exudate images, the C_{CVA} colour features achieve a sensitivity of 96.29%, while the second-best C_{LBP} feature achieve a sensitivity of only 95.85%. We can also see that all features provide slightly better results for the drusen and normal classes in comparison with the exudate class. The results in Table 6.7 also show the standard deviations of the different performance measures for each feature type. As can be seen, the results obtained with the C_{CVA} colour features are more stable than those with other features, as reflected in lower standard deviation values.

Table 6.7 Comparison of different features. For each class, classification sensitivity (Sens), specificity (Spec) and accuracy (Acc) using the k-NN classifier is given. The results indicate the mean value and standard deviation obtained with 10-fold cross-validation.

Class	Measures	Individual Features			
		C_{Gran}	C_{LBP}	C_{CVA}	C_{RGB}
Exudates	Sens	94.63 (±4.63)	95.85 (±3.65)	96.29 (±3.00)	94.04 (±5.91)
	Spec	95.00 (±5.07)	95.78 (±4.46)	97.71 (±2.25)	88.84 (±6.44)

	Acc	94.86 (±3.46)	95.02 (±3.65)	96.86 (±2.99)	94.68 (±3.97)
Drusen	Sens	95.15 (±4.86)	99.07 (±1.38)	96.85 (±2.86)	93.33 (±7.05)
	Spec	94.89 (±4.25)	99.38 (±1.18)	95.46 (±3.96)	92.78 (±8.24)
	Acc	95.88 (±3.31)	98.76 (±1.60)	97.17 (±2.68)	95.71 (±4.01)
Normal	Sens	87.68 (±5.89)	98.87 (±1.96)	97.40 (±1.98)	88.50 (±15.96)
	Spec	91.32 (±5.95)	96.03 (±3.70)	98.83 (±2.61)	90.67 (±15.78)
	Acc	86.70 (±12.49)	97.85 (±2.25)	(98.21 ±1.88)	79.64 (±32.99)

6.4.3 Combination of Features

In this section, different feature types are combined in an attempt to improve classification performance. Based on the results in the previous section, where it was observed that C_{CVA} features give the best classification performance, combinations of C_{CVA} features with other features were also tested. The following combinations were tested $C_{Gran+CVA}$, $C_{LBP+CVA}$, $C_{RGB+CVA}$ and $C_{Gran+LBP+RGB}$.
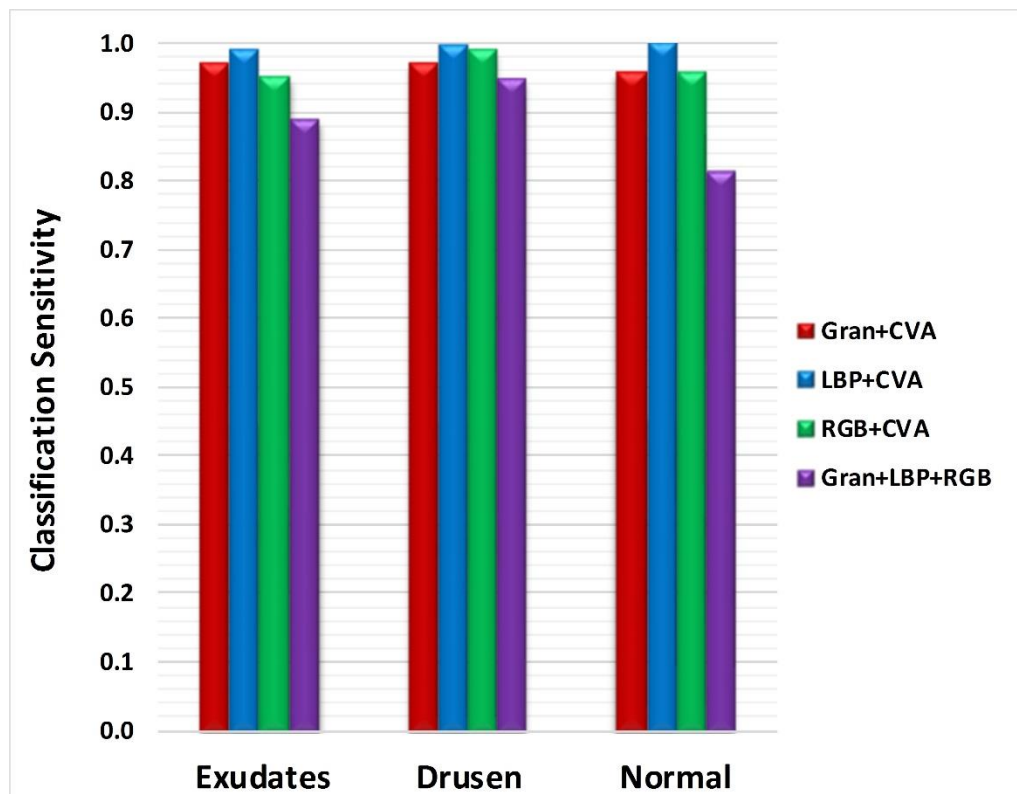
Figure 6.7. Classification sensitivity of feature combinations.
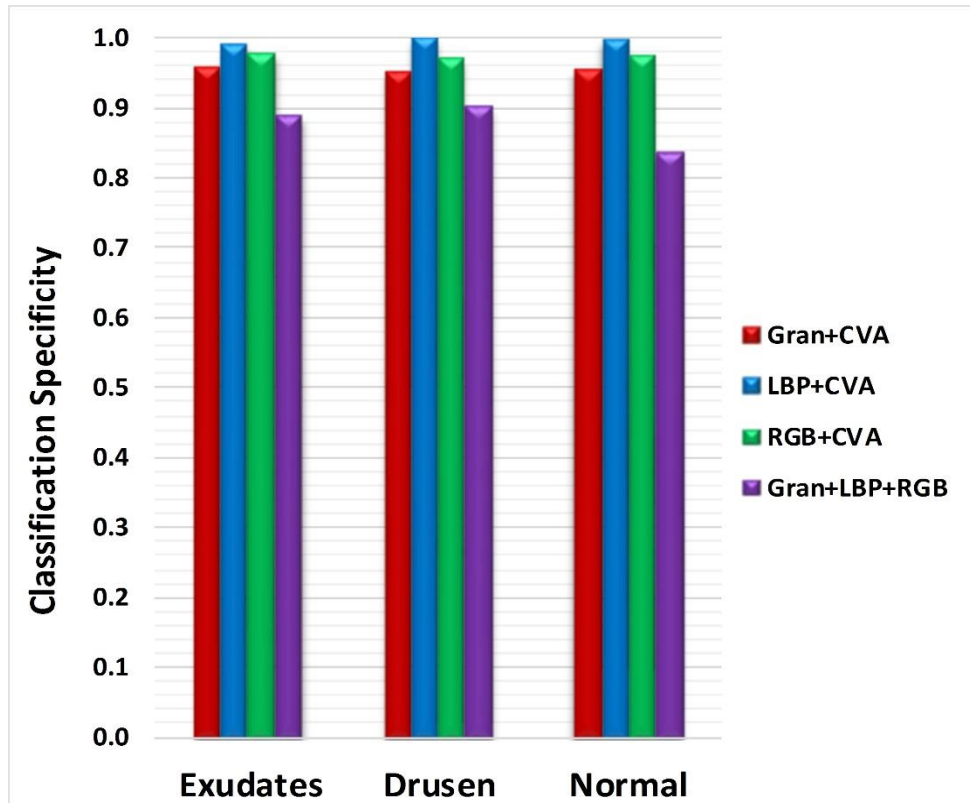
Figure 6.8. Classification specificity of feature combinations.
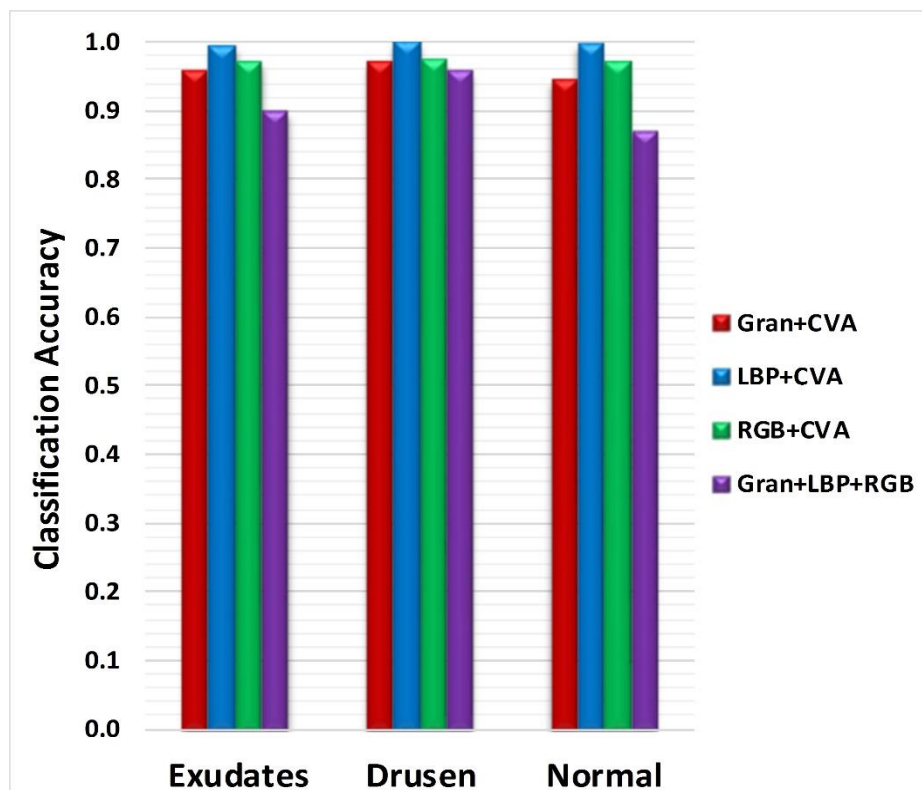
Figure 6.9. Classification accuracy of feature combinations.

The results shown in Figure 6.7, Figure 6.8 and Figure 6.9 show that combining C_{CVA} colour feature with other features types slightly improve the classification results. In particular, a slight improvement is noted when using C_{CVA} colour features combined with C_{LBP} textural features. As can be seen, the classification accuracy increases from 98.21% with C_{CVA} features alone to 99.70% with $C_{CVA+LBP}$ features for the normal class, and from 96.86% to 99.20% for exudates. For the drusen class, the classification accuracy also increases from 97.17% to 100.00%. The combinations $C_{Gran+CVA}$ and $C_{RGB+CVA}$ give similar results compared with C_{CVA} features alone. It is also interesting to observe that the combination $C_{Gran+LBP+RGB}$ performs the worst achieving lower performance than C_{CVA} alone. This is particularly true for the sensitivity measure (see Figure 6.7) as $C_{Gran+LBP+RGB}$ gives a sensitivity of 81.19% for the normal class while C_{CVA} achieves a sensitivity of 97.40% and $C_{LBP+CVA}$ a sensitivity of 100.00%.

Table 6.8 Exudates-vs-rest classification results with the combination of CGran+CVA, CLBP+CVA, CRGB+CVA and CGran+LBP+RGB features. The mean and standard deviation measures are used with 10-fold cross-validation.

Measures	$C_{Gran+CVA}$			$C_{LBP+CVA}$			$C_{RGB+CVA}$			$C_{Gran+LBP+RGB}$		
	SE%	SP%	AC%	SE%	SP%	AC%	SE%	SP%	AC%	SE%	SP%	AC%
ANN (RBF)	91.47 ±3.77	91.50 ±4.39	92.59 ±4.69	95.73 ±2.42	96.86 ±2.46	97.23 ±5.32	92.59 ±4.69	90.00 ±5.05	94.04 ±5.91	76.56 ±9.65	75.44 ±17.24	74.78 ±12.41
SVM	89.89 ±10.55	85.78 ±10.91	89.78 ±9.71	91.89 ±6.37	92.00 ±9.19	94.63 ±4.63	83.67 ±16.50	89.89 ±10.55	88.30 ±3.77	71.44 ±12.25	73.57 ±18.80	78.80 ±11.24
k-NN	96.87 ±2.55	95.46 ±3.08	95.78 ±5.46	98.93 ±2.61	98.85 ±2.65	99.20 ±1.69	95.00 ±7.07	97.60 ±3.86	96.83 ±2.52	88.90 ±3.18	88.84 ±6.44	89.76 ±9.79

Table 6.9 Drusen-vs-rest classification results with the combination of CGran+CVA, CLBP+CVA, CRGB+CVA and CGran+LBP+RGB features. The mean and standard deviation measures are used with 10-fold cross-validation.

Measures	$C_{Gran+CVA}$			$C_{LBP+CVA}$			$C_{RGB+CVA}$			$C_{Gran+LBP+RGB}$		
	SE%	SP%	AC%	SE%	SP%	AC%	SE%	SP%	AC%	SE%	SP%	AC%
ANN (RBF)	86.67 ±17.21	90.00 ±5.05	88.90 ±3.18	98.82 ±2.68	91.89 ±6.37	96.87 ±1.63	92.59 ±4.69	91.47 ±3.77	94.63 ±4.63	73.44 ±17.47	75.44 ±17.24	71.44 ±12.25
SVM	91.50 ±4.39	94.63 ±4.63	91.17 ±4.38	98.05 ±3.33	94.04 ±5.91	95.73 ±3.42	91.89 ±6.37	89.78 ±9.71	95.78 ±5.46	88.84 ±8.44	83.67 ±16.50	85.78 ±10.91
k-NN	96.86 ±2.46	95.00 ±7.07	96.87 ±2.34	99.61 ±0.88	100.00 ±0.00	100.00 ±0.00	98.83 ±2.61	96.78 ±4.24	97.14 ±2.74	94.67 ±6.96	89.89 ±10.55	95.52 ±4.61

The good results obtained when combining $C_{CVA+LBP}$ features can be explained in terms of the fact that C_{CVA} colour features are extracted from the green channel of the colour fundus image, thus ignoring the chromatic information. Therefore, when adding texture feature to C_{CVA} colour information, the descriptor captures more information. However, as seen in the results, combining $C_{Gran+LBP+RGB}$ features does not provide a better performance compared with $C_{CVA+LBP}$ features as shown in Table 6.8, Table 6.9, Table 6.10 and Table 6.11.

Table 6.10 Normal-vs-rest classification results with the combination of CGran+CVA, CLBP+CVA, CRGB+CVA and CGran+LBP+RGB features. The mean and standard deviation measures are used with 10-fold cross-validation.

Measures	$C_{Gran+CVA}$			$C_{LBP+CVA}$			$C_{RGB+CVA}$			$C_{Gran+LBP+RGB}$		
	SE%	SP%	AC%	SE%	SP%	AC%	SE%	SP%	AC%	SE%	SP%	AC%
ANN (RBF)	83.57 ±15.81	80.00 ±23.31	83.33 ±19.57	92.12 ±7.55	92.50 ±16.87	95.48 ±6.94	86.67 ±17.21	88.43 ±11.36	86.58 ±10.49	74.67 ±10.15	79.64 ±32.99	82.38 ±13.05
SVM	87.50 ±21.76	85.84 ±13.45	88.78 ±8.38	89.67 ±12.08	87.80 ±9.67	89.76 ±9.79	88.30 ±6.27	86.67 ±14.86	87.68 ±5.89	74.67 ±10.15	73.57 ±18.80	78.80 ±11.24
k-NN	95.71 ±6.90	95.36 ±6.51	94.33 ±10.91	100.00 ±0.00	99.69 ±0.99	99.70 ±0.96	95.71 ±8.90	97.14 ±4.39	96.90 ±4.55	81.19 ±21.31	83.57 ±15.81	86.70 ±12.49

Table 6.11 Comparison of different combinations of feature types. For each class, the classification sensitivity (Sens), specificity (Spec), accuracy (Acc) and AUC using the k-NN classifier are given. The results indicate the mean value and standard deviation obtained with 10-fold cross-validation.

Class	Measures	Combined Features			
		$C_{Gran+CVA}$	$C_{LBP+CVA}$	$C_{RGB+CVA}$	$C_{Gran+LBP+RGB}$
Exudates	Sens	96.87 ±2.55	98.93 ±2.61	95.00 ±7.07	88.90 ±3.18
	Spec	95.46 ±3.08	98.85 ±2.65	97.60 ±3.86	88.84 ±6.44
	Acc	95.78 ±5.46	99.20 ±1.69	96.83 ±2.52	89.76 ±9.79
	AUC	93.87 (±8.96)	97.33±2.61	82.86 (±19.98)	82.86 (±19.98)
Drusen	Sens	96.86 ±2.46	99.61 ±0.88	98.83 ±2.61	94.67 ±6.96
	Spec	95.00 ±7.07	100.00 ±0.00	96.78 ±4.24	89.89 ±10.55
	Acc	96.87 ±2.34	100.00 ±0.00	97.14 ±2.74	95.52 ±4.61
	AUC	92.03 (±9.70)	99.80±0.79	93.50 (±14.15)	82.86 (±19.98)
Normal	Sens	95.71 ±6.90	100.00 ±0.00	95.71 ±8.90	81.19 ±21.31
	Spec	95.36 ±6.51	99.69 ±0.99	97.14 ±4.39	83.57 ±15.81
	Acc	94.33 ±10.91	99.70 ±0.96	96.90 ±4.55	86.70 ±12.49
	AUC	93.87 (±8.96)	98.65±0.98	95.00 (±10.54)	82.86 (±19.98)

6.4.4 Comparison with Existing Systems

For the sake of illustration, a recently published technique for the detection of exudate regions based on texture information (Akram et al., 2013a) has been implemented and applied to the same dataset. A comparison has been carried out in terms of measurements shown in Table 6.12. The combination of C_{CVA} colour features with different features based on the BoF approach are extracted for the proposed method. Meanwhile gray-level features based on gray level intensities inside the candidate region combined with statistical features such as entropy, energy and moments were used in Akram et al. (2013a) work. Our k-NN classifier achieved good results, and the comparison with other research on classifiers is given in Table 6.12 as compared to Akram et al. (2013a) who achieved good results initially with the GMM classifier, which is fairly good. However, the method proposed in this study gives very good performance when compared with Akram et al. (2013a) work. The proposed system gives higher values with the same

dataset, which makes it suitable for an automated medical system for diagnosing and identifying lesions related to the DR and AMD diseases containing exudates, drusen as well as images with no lesions.

In another study by van Grinsven et al. (2013), an automatic system was proposed to retrieve and classify images with bright lesions, namely exudates and drusen, using the BoF method. The system used a set of features which includes the histogram of oriented gradients (HOG), colour histograms and local binary patterns (LBPs). Afterwards, a codebook dictionary is created using these features and classification is performed with the k-NN classifier. The results obtained using an area under the curve for image classification of 90%.

The proposed method has also been compared with the methods proposed by Giancardo et al. (2012), who presented a new technique for the automatic diagnosis of diabetic macular edema using a set of structures that include colour, wavelet decomposition and automatic lesion segmentation. The method was evaluated against the publicly available HEI-MED and MESSIDOR datasets. The standardized images were additionally improved with morphological reconstruction giving a clear distinction between dark and bright structures. Their method achieved results for area under the curve between 0.88 and 0.93. All of these classification approaches require the accurate manual annotation of the training dataset.

In comparison, the method proposed in previous work by Omar et al. (2016), has high potential and can be used for lesion detection. The results obtained for the k-NN classifier were 93.03%, 94.60% and 93.71% for sensitivity, specificity and accuracy respectively, whereas the RBF neural network results for sensitivity, specificity and accuracy were 98.68%, 94.81% and 96.73% respectively. Table 6.12 shows the experimental results in terms of sensitivity, specificity, accuracy and AUC (Omar et al., 2016). Based on these results, the k-NN classifier gives better overall performance than any other classifier in the proposed method, as shown in Table 6.12.

Although our technique is not directly comparable because it diagnoses DR and AMD diseases which related different lesions, the AUCs presented are comparable or above these two systems.

Table 6.12 Comparison between the proposed method of feature combination using the BoF
approach and the k-NN classifier and five systems proposed in the literature in terms of
sensitivity, specificity, accuracy and AUC.

Measures	Akram et al. (2013a)	van Grinsven et al. (2013)	Giancardo et al. (2012)	Omar et al. (2016)	Khalid et al. (2017)	Proposed method
Sens (%)	90.63	93.01	–	98.68	97.50	99.51
Spec (%)	88.70	91.64	–	94.81	83.00	99.60
Acc (%)	88.93	92.73	–	96.73	95.52	99.63
AUC (%)	–	90.0	88.0	–	–	98.59

6.5   Conclusion

This work proposes an automatic classification scheme to distinguish between retinal images containing different bright lesions, namely exudates and drusen and images with no lesions. The system relies on a bag-of-features approach using codebooks where new colour and textural features are proposed for describing DR and AMD lesions efficiently, namely granulometry morphological (Gran), local binary patterns (LBPs), colour vector angles (CVAs) and RGB colour features. The approach is based on a bag-of-features using the CVA colour features. In particular, the proposed system does not require any segmentation of retinal images; for example, optic disc removal or the segmentation of blood vessels.

Firstly, features are extracted, such as granulometry, LBP, CVA and RGB features, and afterwards a histogram is generated by extracting a set of features from local selected patches extracted from every image. Secondly, three codebook dictionaries (C_{Gran}, and C_{RGB}, $C_{LBP+CVA}$) are generated using the extracted features and histograms are built for each image to be considered as features describing the image. Finally, with respect to the C_{CVA} colour features, a mean accuracy of 97.41% was achieved; however, the best accuracy of all was achieved using the combined $C_{LBP+CVA}$ features with a mean accuracy of 99.63%, which demonstrates the ability of this method.

In conclusion, the proposed automatic classification framework for screening DR and AMD diseases in a biomedicine framework adapts a bag-of-features to discriminate three-

class disease cases of exudates, drusen, and no lesions lasses (normal and two diseases) instead of the two-class classification model that is considered a challenge for any CAD system. In this work, an automatic retinal diagnosis system that combines different colour and textural features is proposed which was applied to five different datasets, namely the DIARETDB0, DIARETDB1, HEI-MED, STARE and MESSIDOR datasets and is shown to achieve efficient and accurate retinal lesion detection. Finally, comparison experiments demonstrate the robustness and superiority of the technique proposed in this work.

7. CONCLUSION AND RECOMMENDATIONS

7.1 Introduction

Diagnosing DR, AMD and DME in its early stages is a challenging task for ophthalmologists given the fact that the chances of a patient's prognosis are better with diagnosis in these early stages. This indicates that the process of analysing retinal fundus images and making decisions should be time-efficient. Today, the diagnosis of DR, AMD and DME diseases using automated and computerised systems is essential. DR and DME are forms of diabetes that are usually treatable if detected and diagnosed early. Whereas, AMD is a problem of the retina when a part of the retina called the macula is damaged. Over time, it leads to a gradual loss of central vision. The early detection of retinal lesions will lead to better outcomes; otherwise, retinal lesions can develop and lead to vision loss. Accordingly, the conditions become difficult to treat and the results can be disastrous. The clinical diagnosis of retinal lesions is subject to human error, and early diagnosis can be improved by using automated procedures. Motivated by this, the present research investigates the development of new approaches to improve the performance of automatic from retinal images diagnosis.

In this thesis, an automated approach to retinal lesion diagnosis using efficient features in publically available retinal fundus images datasets with the aim to improve performance has been proposed to assist ophthalmologists in the accurate detection of retinal lesions. The common techniques for dealing with the early detection of retinal lesions, including several stages of pre-processing, segmentation, feature extraction, and classification, are reviewed in this work. All of these stages play an important role in avoiding any errors in detection, owing to the fact that the output of each stage is the input of the next stage.

This work proposes three different techniques. Firstly, a new LBP-based feature extraction technique has been applied for classification, which can be used to efficiently discriminate between features for exudate detection. Based on experiments, the system has shown good ability for the detection of abnormalities associated with DR. Exudates are signs of DR and are not easy to detect due to other normal retinal characteristics with similar features such as contrast, intensity levels, colour and shape. When digital fundus images are captured using cameras with uneven illumination, the detection problem becomes even more difficult. In contrast to previous methods, the LBP-based feature

extraction is applied after dividing the image into number of blocks instead of using the whole image in the analysis. The extracted features have been applied to both RBF-NN and k-NN classifiers for training and testing purposes. Compared to existing systems, this proposed method shows some improvements in performance.

The second proposed system consists of a technique based on a multi-label model for multiple DME disease diagnosis and the determination of patient age. This is an extension of previous research, which was concerned with changing disease classification as a two-class problem in to a multi-label machine learning classification problem by combining the diagnosis of diabetic macular edema (DME) with other factors such as patient age. The LBP-based feature extraction technique has been applied for classification. Four multi-label classifiers are investigated (ML-kNN, ML-rank SVM, MLNN-RBF and MLNN-BP) and 5-fold cross-validation is applied for evaluation. The proposed multi-label model can learn simultaneously from multiple labels such as DME disease diagnosis and patient age. This type of multiple disease screening is highly appropriate for real-world diagnostic situations because patients may possibly have two or three different diseases. Finally, the results obtained have shown that system performance can be improved with such combined features.

In the third proposed technique, it is particularly claimed that the use of colour vector angles (CVAs) and local binary patterns (LBPs) leads to high classification performance as compared to other textural and colour features, hence making it appropriate in the analysis and classification of retinal images. This is because the LBP is powerful against monotonic grey-level intensity changes caused by varying illumination and high contrast. Moreover, the CVA is used to identify colour edges because it is insensitive to variations in intensity while being sensitive to differences in hue and saturation, whereas Euclidean distance does not have this capability (Dony and Wesolkowski, 1999).

A codebook is generated using a combination of local binary pattern (LBP) and colour vector angle (CVA) features to exploit colour and textural information. The overall system has been assessed through extensive experiments using different classifiers on five datasets: DIARETDB0 (Kauppi et al., 2006), DIARETDB1 (Kälviäinen and Uusitalo, 2007), HEI-MED (Giancardo et al., 2012), STARE (Hoover and Goldbaum, 2003), and MESSIDOR (Decencière et al., 2014). Correct classification has been reported with an average sensitivity of 99.51%, specificity of 99.60% and accuracy of 99.63% and an

overall average of area under the curve of 98.59%. This represents the best performance achieved so far when compared to existing state-of-the-art retinal lesion detection and diagnosis systems.

As a result, several significant outcomes concerning the features and environment of retinal lesion detection have been achieved and a number of methodologies have been proposed for the diagnosis of diabetes. Moreover, physicians can explore reliable features that would ensure the detection of retinal lesion and lead to treatment as early as possible in order to reduce the chance of vision loss. To conclude, the proposed bag-of-features technique can play a significant role in the classification of abnormal and normal fundus images with bright lesions, and it can help ophthalmologists in the early stages of retinal lesion diagnosis.

7.2 Project Evaluation

Although months were spent during my first year looking for a new supervisor after my previous principal supervisor left the university, and this caused a delay in the progress of the work, the objectives of this work have been retained when working with my current principal supervisor. One of the difeculties faced in, experiments was that datasets did not include large numbers of images that are medically annotated in terms of lesions and this has led to the adoption of a cross-validation approach in this project to overcome the issue of the limited size of datasets and to make the measurements more reasonable.

7.3 Future Work and Recommendations

In practice, it would be wise to use large numbers of medically annotated images in the training and validation phases to ensure the reliability of a retinal diagnosis system. For the sake of an optimal automated diagnosis system, it is recommended that more texture and colour descriptors should be investigated with local and global features. The proposed method could be extended to deal with more challenging spot lesions, namely microaneurysms, haemorrhages and soft drusen with very low intensity values and to subsequently include a feature extraction process that combines colour with texture information. In addition, efficient feature projection techniques such as linear discriminant analysis (LDA) and kernel discriminant analysis (KDA) could enhance the feature representation space prior to training the classifier. Furthermore, an exploration of geometric features might enhance the bag-of-features approach, since these features

have been proven efficient in discriminating between normal and abnormal retinal images especially when combined with colour and texture features. Finally, recent progress in machine learning offers new prospects for the computer-aided of diagnosis DR, DME and AMD. Major recent developments are partially due to the success of deep learning techniques, which have attracted attention from both academic researchers and the commercial application communities. Deep learning is currently the fastest growing field in machine learning and might contribute significantly to the field of retinal lesion detection and diagnosis. Recent research has demonstrated that deep learning can significantly enhance the classification accuracy with sophisticated image operations at various levels of a deep convolutional neural network. Thus, deep learning techniques might offer good alternatives for the diagnosis of DR, DME and AMD.

REFERENCES

ABRÀMOFF, M. D., GARVIN, M. K. & SONKA, M. 2010. Retinal imaging and image analysis. *IEEE reviews in biomedical engineering,* 3**,** 169-208.

ABRAMOFF, M. D. & NIEMEIJER, M. The automatic detection of the optic disc location in retinal images using optic disc location regression. Engineering in Medicine and Biology Society, 2006. EMBS'06. 28th Annual International Conference of the IEEE, 2006. IEEE, 4432-4435.

ABRAMOFF, M. D., NIEMEIJER, M. & RUSSELL, S. R. 2010. Automated detection of diabetic retinopathy: barriers to translation into clinical practice. *Expert review of medical devices,* 7**,** 287-296.

ACHARYA, U. R., LIM, C. M., NG, E. Y. K., CHEE, C. & TAMURA, T. 2009. Computer-based detection of diabetes retinopathy stages using digital fundus images. *Proceedings of the Institution of Mechanical Engineers, Part H: Journal of Engineering in Medicine,* 223**,** 545-553.

ACTON, S. T., SOLIZ, P., RUSSELL, S. & PATTICHIS, M. S. Content based image retrieval: The foundation for future case-based and evidence-based ophthalmology. 2008 IEEE International Conference on Multimedia and Expo, 2008. IEEE, 541-544.

AGURTO, C., BARRIGA, E. S., MURRAY, V., NEMETH, S., CRAMMER, R., BAUMAN, W., ZAMORA, G., PATTICHIS, M. S. & SOLIZ, P. 2011. Automatic detection of diabetic retinopathy and age-related macular degeneration in digital fundus images. *Investigative ophthalmology & visual science,* 52**,** 5862-5871.

AGURTO, C., YU, H., MURRAY, V., PATTICHIS, M. S., BARRIGA, S. & SOLIZ, P. Detection of hard exudates and red lesions in the macula using a multiscale approach. Image Analysis and Interpretation (SSIAI), 2012 IEEE Southwest Symposium on, 2012. IEEE, 13-16.

AKRAM, M. U., KHALID, S. & KHAN, S. A. 2013a. Identification and classification of microaneurysms for early detection of diabetic retinopathy. *Pattern Recognition,* 46**,** 107-116.

AKRAM, M. U., MUJTABA, S. & TARIQ, A. Automated drusen segmentation in fundus images for diagnosing age related macular degeneration. Electronics, Computer and Computation (ICECCO), 2013 International Conference on, 2013b. IEEE, 17-20.

AKRAM, U. M. & KHAN, S. A. 2012. Automated detection of dark and bright lesions in retinal images for early detection of diabetic retinopathy. *Journal of medical systems,* 36**,** 3151-3162.

ALGHADYAN, A. A. 2011. Diabetic retinopathy–An update. *Saudi Journal of Ophthalmology,* 25**,** 99-111.

ALY, Z., TAJ, F. & KAMAL, A. K. 2009. Evaluating ischemic stroke subtypes: does the retinal microvasculature hold clues to what lies beneath? *Stroke,* 40**,** e400-e400.

ASSOCIATION, A. D. 2007. The dangerous toll of diabetes [ADA Web site].

ATTIA, J. 2003. Moving beyond sensitivity and specificity: using likelihood ratios to help interpret diagnostic tests. *Issues***,** 1.

BISHOP, C. M. 1995. *Neural networks for pattern recognition*, Oxford university press.

BOLSTER, N. M., GIARDINI, M. E. & BASTAWROUS, A. 2016. The diabetic retinopathy screening workflow: potential for smartphone imaging. *Journal of diabetes science and technology,* 10**,** 318-324.

BOUTELL, M. R., LUO, J., SHEN, X. & BROWN, C. M. 2004. Learning multi-label scene classification. *Pattern recognition,* 37**,** 1757-1771.

BRESNICK, G. H., MUKAMEL, D. B., DICKINSON, J. C. & COLE, D. R. 2000. A screening approach to the surveillance of patients with diabetes for the presence of vision-threatening retinopathy. *Ophthalmology,* 107**,** 19-24.

BROECKER, E. H. & DUNBAR, M. T. 2005. Optical coherence tomography: its clinical use for the diagnosis, pathogenesis, and management of macular conditions. *Optometry-Journal of the American Optometric Association,* 76**,** 79-101.

BUCCA, B., 2014. *Ophthalmology |School of Medicine |University of Colorado Denver* [Online]. Available: http://www.ucdenver.edu/academics/colleges/medicalschool/centers/BarbaraDav is/Clinical/Pages/Ophthalmology.aspx [Accessed 04 Apr. 2017]. [Accessed [online] Ucdenver.edu.].

CADE, W. T. 2008. *Diabetes-related microvascular and macrovascular diseases in the physical therapy setting* [Online]. [Accessed 11 88].

CAICEDO, J. C., CRUZ, A. & GONZALEZ, F. A. 2009. Histopathology image classification using bag of features and kernel functions. *Artificial intelligence in medicine.* Springer.

CAPRETTE, C. L., LEE, M. S., SHINE, R., MOKANY, A. & DOWNHOWER, J. F. 2004. The origin of snakes (Serpentes) as seen through eye anatomy. *Biological Journal of the Linnean Society,* 81**,** 469-482.

CHAUM, E., KARNOWSKI, T. P., GOVINDASAMY, V. P., ABDELRAHMAN, M. & TOBIN, K. W. 2008. Automated diagnosis of retinopathy by content-based image retrieval. *Retina,* 28**,** 1463-1477.

CHENG, Q., SAADDINE, J. B., KLEIN, R., ROTHENBERG, R., CHOU, C.-F. & IL'YASOVA, D. 2017. Early Age-related Macular Degeneration with Cardiovascular and Renal Comorbidities: An Analysis of the National Health and Nutrition Examination Survey, 2005–2008. *Ophthalmic epidemiology,* 24**,** 413-419.

CHIANG, T.-H., LO, H.-Y. & LIN, S.-D. 2012. A Ranking-based KNN Approach for Multi-Label Classification. *ACML,* 25**,** 81-96.

COHEN, S. R. & GARDNER, T. W. 2015. Diabetic Retinopathy and Diabetic Macular Edema. *Retinal Pharmacotherapeutics.* Karger Publishers.

COLLABORATION, N. R. F. 2016. Worldwide trends in diabetes since 1980: a pooled analysis of 751 population-based studies with 4· 4 million participants. *The Lancet,* 387**,** 1513-1530.

CONTROL, C. F. D. & PREVENTION 2011a. National diabetes fact sheet: national estimates and general information on diabetes and prediabetes in the United States, 2010. *http://www. caldiabetes. org/content_display. cfm? FontSize= normal&contentID= 562&CategoriesID= 31*.

CONTROL, C. F. D. & PREVENTION 2011b. National diabetes fact sheet: national estimates and general information on diabetes and prediabetes in the United States, 2011. *Atlanta, GA: US Department of Health and Human Services, Centers for Disease Control and Prevention,* 201.

COUDRAY, N., BUESSLER, J., KIHL, H. & URBAN, J. 2007. TEM images of membranes: A multiresolution edge-detection approach for watershed segmentation. *Physics in Signal and Image Processing (PSIP),* 6.

CREE, M. J., GAMBLE, E. & CORNFORTH, D. J. 2005. Colour normalisation to reduce inter-patient and intra-patient variability in microaneurysm detection in colour retinal images.

CSAKY, K., FERRIS, F., CHEW, E. Y., NAIR, P., CHEETHAM, J. K. & DUNCAN, J. L. 2017. Report From the NEI/FDA Endpoints Workshop on Age-Related Macular Degeneration and Inherited Retinal Diseases. *Investigative ophthalmology & visual science,* 58**,** 3456-3463.

DA ROCHA FERNANDES, J., OGURTSOVA, K., LINNENKAMP, U., GUARIGUATA, L., SEURING, T., ZHANG, P., CAVAN, D. & MAKAROFF, L. E. 2016. IDF Diabetes Atlas estimates of 2014 global health expenditures on diabetes. *Diabetes research and clinical practice,* 117**,** 48-54.

DALAL, N. & TRIGGS, B. Histograms of oriented gradients for human detection. 2005 IEEE Computer Society Conference on Computer Vision and Pattern Recognition (CVPR'05), 2005. IEEE, 886-893.

DECENCIÈRE, E., ZHANG, X., CAZUGUEL, G., LAY, B., COCHENER, B., TRONE, C., GAIN, P., ORDONEZ, R., MASSIN, P., ERGINAY, A., CHARTON, B. & KLEIN, J.-C. 2014. FEEDBACK ON A PUBLICLY DISTRIBUTED IMAGE DATABASE: THE MESSIDOR DATABASE. *2014,* 33*,* 4.

DEEPAK, K. S., CHAKRAVARTY, A. & SIVASWAMY, J. Visual saliency based bright lesion detection and discrimination in retinal images. Biomedical Imaging (ISBI), 2013 IEEE 10th International Symposium on, 2013. IEEE, 1436-1439.

DEEPAK, K. S. & SIVASWAMY, J. 2012. Automatic assessment of macular edema from color retinal images. *Medical Imaging, IEEE Transactions on,* 31**,** 766-776.

DING, J. & WONG, T. Y. 2012. Current epidemiology of diabetic retinopathy and diabetic macular edema. *Current diabetes reports,* 12**,** 346-354.

DOI, K. 2007. Computer-aided diagnosis in medical imaging: historical review, current status and future potential. *Computerized medical imaging and graphics,* 31**,** 198-211.

DONY, R. & WESOLKOWSKI, S. Edge detection on color images using RGB vector angles. Electrical and Computer Engineering, 1999 IEEE Canadian Conference on, 1999. IEEE, 687-692.

EADGAHI, M. G. F. & POURREZA, H. Localization of hard exudates in retinal fundus image by mathematical morphology operations. Computer and Knowledge Engineering (ICCKE), 2012 2nd International eConference on, 2012. IEEE, 185-189.

EGE, B. M., HEJLESEN, O. K., LARSEN, O. V., MØLLER, K., JENNINGS, B., KERR, D. & CAVAN, D. A. 2000. Screening for diabetic retinopathy using computer based image analysis and statistical classification. *Computer methods and programs in biomedicine,* 62**,** 165-175.

ENDLER, J. A. 1993. The color of light in forests and its implications. *Ecological monographs,* 63**,** 1-27.

FATHI, A. & NAGHSH-NILCHI, A. R. 2013. Integrating adaptive neuro-fuzzy inference system and local binary pattern operator for robust retinal blood vessels segmentation. *Neural Computing and Applications,* 22**,** 163-174.

FLEMING, A. D., PHILIP, S., GOATMAN, K. A., WILLIAMS, G. J., OLSON, J. A. & SHARP, P. F. 2007. Automated detection of exudates for diabetic retinopathy screening. *Physics in medicine and biology,* 52**,** 7385.

FONG, D. S., AIELLO, L., GARDNER, T. W., KING, G. L., BLANKENSHIP, G., CAVALLERANO, J. D., FERRIS, F. L. & KLEIN, R. 2004. Retinopathy in diabetes. *Diabetes care,* 27**,** s84-s87.

FORACCHIA, M., GRISAN, E. & RUGGERI, A. 2005. Luminosity and contrast normalization in retinal images. *Medical Image Analysis,* 9**,** 179-190.

GARCÍA, M., SÁNCHEZ, C. I., LÓPEZ, M. I., ABÁSOLO, D. & HORNERO, R. 2009. Neural network based detection of hard exudates in retinal images. *Computer Methods and programs in biomedicine,* 93**,** 9-19.

GARCIA, T. B., PANNICKE, T., VOGLER, S., BERK, B. A., GROSCHE, A., WIEDEMANN, P., SEEGER, J., REICHENBACH, A., HERCULANO, A. M. & BRINGMANN, A. 2014. Nerve growth factor inhibits osmotic swelling of rat retinal glial (Müller) and bipolar cells by inducing glial cytokine release. *Journal of neurochemistry,* 131**,** 303-313.

GIANCARDO, L., MERIAUDEAU, F., KARNOWSKI, T. P., LI, Y., GARG, S., TOBIN, K. W. & CHAUM, E. 2012. Exudate-based diabetic macular edema detection in fundus images using publicly available datasets. *Medical image analysis,* 16**,** 216-226.

GONZALEZ, M. & BALLARIN, V. 2009. Automatic marker determination algorithm for watershed segmentation using clustering. *Latin American applied research,* 39**,** 225-229.

GONZALEZ, R. C., WOODS, R. & EDDINS, S. 2008. Morphological reconstruction from digital image processing using MATLAB. *MATLAB Digest–Academic Edition*.

GREGORY, R. L. 2015. *Eye and brain: The psychology of seeing*, Princeton university press.

GROUP, E. T. D. R. S. R. 1991. Early photocoagulation for diabetic retinopathy: ETDRS report number 9. *Ophthalmology,* 98**,** 766-785.

GUARIGUATA, L., WHITING, D. R., HAMBLETON, I., BEAGLEY, J., LINNENKAMP, U. & SHAW, J. E. 2014. Global estimates of diabetes prevalence for 2013 and projections for 2035. *Diabetes research and clinical practice,* 103**,** 137-149.

HARI, V., RAJ, V. J. & GOPIKAKUMARI, R. 2017. Quadratic filter for the enhancement of edges in retinal images for the efficient detection and localization of diabetic retinopathy. *Pattern Analysis and Applications,* 20**,** 145-165.

HEIMANN, H., KELLNER, U. & FOERSTER, M. H. 2006. *Atlas of fundus angiography*, Thieme.

HIILLERMEIER, W. C.-E. 2009. Combining instance-based learning and logistic regression for multilabel classification. *Mach Learn,* 76**,** 211-225.

HIJAZI, M., JIANG, C., COENEN, F. & ZHENG, Y. 2011a. Image classification for age-related macular degeneration screening using hierarchical image decompositions and graph mining. *Machine Learning and Knowledge Discovery in Databases***,** 65-80.

HIJAZI, M. H. A., COENEN, F. & ZHENG, Y. 2011b. Retinal image classification for the screening of age-related macular degeneration. *Research and Development in Intelligent Systems XXVII.* Springer.

HOOVER, A. & GOLDBAUM, M. 2003. Locating the optic nerve in a retinal image using the fuzzy convergence of the blood vessels. *IEEE transactions on medical imaging,* 22**,** 951-958.

HUANG, D.-S., GUPTA, P., WANG, L. & GROMIHA, M. 2009. Emerging intelligent computing technology and applications.

HUNTER, A., LOWELL, J., OWENS, J., KENNEDY, L. & STEELE, D. 2000. Quantification of diabetic retinopathy using neural networks and sensitivity analysis. *Artificial Neural Networks in Medicine and Biology.* Springer.

IFEACHOR, E. C. & JERVIS, B. W. 2002. *Digital signal processing: a practical approach*, Pearson Education.

JAYAKUMARI, C. & SANTHANAM, T. 2007. Retinal blood vessel segmentation for assessment of diabetic retinopathy using a two-dimensional model. *Asian J. Inf. Technol,* 6**,** 1205-1211.

JOUSSEN, A. M., GARDNER, T. W., KIRCHHOF, B. & RYAN, S. J. 2007. *Retinal vascular disease*, Springer.

KALLERGI, M. 2005. 12 Evaluation Strategies for Medical-Image Analysis and Processing Methodologies. *Medical image analysis methods***,** 433.

KÄLVIÄINEN, R. V. J. P. H. & UUSITALO, H. 2007. DIARETDB1 diabetic retinopathy database and evaluation protocol. *Medical Image Understanding and Analysis 2007***,** 61.

KANSKI, J. J. & BOWLING, B. 2011. *Clinical ophthalmology: a systematic approach*, Elsevier Health Sciences.

KAREGOWDA, A. G., NASIHA, A., JAYARAM, M. & MANJUNATH, A. 2011. Exudates detection in retinal images using back propagation neural network. *International Journal of Computer Applications,* 25**,** 25-31.

KARNON, J., CZOSKI-MURRAY, C., SMITH, K., BRAND, C., CHAKRAVARTHY, U., DAVIS, S., BANSBACK, N., BEVERLEY, C., BIRD, A. & HARDING, S. 2008. A preliminary model-based assessment of the cost–utility of a screening programme for early age-related macular degeneration.

KAUPPI, T., KALESNYKIENE, V., KAMARAINEN, J.-K., LENSU, L., SORRI, I., RANINEN, A., VOUTILAINEN, R., UUSITALO, H., KÄLVIÄINEN, H. & PIETILÄ, J. The DIARETDB1 Diabetic Retinopathy Database and Evaluation Protocol. BMVC, 2007. 1-10.

KAUPPI, T., KALESNYKIENE, V., KAMARAINEN, J.-K., LENSU, L., SORRI, I., UUSITALO, H., KÄLVIÄINEN, H. & PIETILÄ, J. 2006. DIARETDB0: Evaluation database and methodology for diabetic retinopathy algorithms. *Machine Vision and Pattern Recognition Research Group, Lappeenranta University of Technology, Finland.*

KAVITHA, S. & DURAISWAMY, K. 2011. Automatic detection of hard and soft exudates in fundus images using color histogram thresholding. *European Journal of Scientific Research,* 48**,** 493-504.

KELLER, J. M., GRAY, M. R. & GIVENS, J. A. 1985. A fuzzy k-nearest neighbor algorithm. *IEEE transactions on systems, man, and cybernetics***,** 580-585.

KHALID, S., AKRAM, M. U. & KHALIL, T. Hybrid textural feature set based automated diagnosis system for Age Related Macular Degeneration using fundus images. Communication, Computing and Digital Systems (C-CODE), International Conference on, 2017. IEEE, 390-395.

KIRCHNER, M. & FRIDRICH, J. On detection of median filtering in digital images. IS&T/SPIE Electronic Imaging, 2010. International Society for Optics and Photonics, 754110-754110-12.

KLEIN, R., KLEIN, B. E., MOSS, S. E., DAVIS, M. D. & DEMETS, D. L. 1984a. The Wisconsin Epidemiologic Study of Diabetic Retinopathy: II. Prevalence and risk

of diabetic retinopathy when age at diagnosis is less than 30 years. *Archives of ophthalmology,* 102**,** 520-526.

KLEIN, R., KLEIN, B. E., MOSS, S. E., DAVIS, M. D. & DEMETS, D. L. 1984b. The Wisconsin Epidemiologic Study of Diabetic Retinopathy: III. Prevalence and risk of diabetic retinopathy when age at diagnosis is 30 or more years. *Archives of ophthalmology,* 102**,** 527-532.

KLEIN, R. J., ZEISS, C., CHEW, E. Y., TSAI, J.-Y., SACKLER, R. S., HAYNES, C., HENNING, A. K., SANGIOVANNI, J. P., MANE, S. M. & MAYNE, S. T. 2005. Complement factor H polymorphism in age-related macular degeneration. *Science,* 308**,** 385-389.

KUBAT, M. 1999. Neural networks: a comprehensive foundation by Simon Haykin, Macmillan, 1994, ISBN 0-02-352781-7. Cambridge Univ Press.

KUMARI, V. V., SURIYAHARAYANANM, N. & SARANYA, C. T. Feature extraction for early detection of diabetic retinopathy. Recent Trends in Information, Telecommunication and Computing (ITC), 2010 International Conference on, 2010. IEEE, 359-361.

LAVINSKY, F., WOLLSTEIN, G., TAUBER, J. & SCHUMAN, J. S. 2017. The future of imaging in detecting glaucoma progression. *Ophthalmology,* 124**,** S76-S82.

LEE, J., KIM, H., KIM, N.-R. & LEE, J.-H. 2016a. An Approach for Multi-Label Classification by Directed Acyclic Graph with Label Correlation Maximization. *Information Sciences*.

LEE, J., KIM, H., KIM, N.-R. & LEE, J.-H. 2016b. An approach for multi-label classification by directed acyclic graph with label correlation maximization. *Information Sciences,* 351**,** 101-114.

LI, J., LI, B., XU, Y., LU, K., YAN, K. & FEI, L. 2014. Disguised face detection and recognition under the complex background. Computational Intelligence in Biometrics and Identity Management (CIBIM), 2014 IEEE Symposium on, 2014. IEEE, 87-93.

LIM, S., ZAKI, W. M. D. W., HUSSAIN, A., LIM, S. & KUSALAVAN, S. Automatic classification of diabetic macular edema in digital fundus images. Humanities, Science and Engineering (CHUSER), 2011 IEEE Colloquium on, 2011. IEEE, 265-269.

LIU, G.-P., LI, G.-Z., WANG, Y.-L. & WANG, Y.-Q. 2010. Modelling of inquiry diagnosis for coronary heart disease in traditional Chinese medicine by using multi-label learning. *BMC complementary and alternative medicine,* 10**,** 1.

LIU, G.-P., YAN, J.-J., WANG, Y.-Q., FU, J.-J., XU, Z.-X., GUO, R. & QIAN, P. 2012. Application of multilabel learning using the relevant feature for each label in chronic gastritis syndrome diagnosis. *Evidence-Based Complementary and Alternative Medicine,* 2012.

LJUBIMOV, A. V. 2017. Cell Therapy for Age-Related Macular Degeneration: A New Vision for the Bone Marrow? *Molecular Therapy,* 25**,** 832-833.

LOEWENSTEIN, A. 2007. The significance of early detection of age-related macular degeneration: Richard & Hinda Rosenthal Foundation lecture, The Macula Society 29th annual meeting. *Retina,* 27**,** 873-878.

LUO, J. 2012. *Soft computing in information communication technology*, Springer.

MARAGOS, P. & SCHAFER, R. W. 1990. Morphological systems for multidimensional signal processing. *Proceedings of the IEEE,* 78**,** 690-710.

MONTAÑES, E., SENGE, R., BARRANQUERO, J., QUEVEDO, J. R., DEL COZ, J. J. & HÜLLERMEIER, E. 2014. Dependent binary relevance models for multi-label classification. *Pattern Recognition,* 47**,** 1494-1508.

MOODY, J. 1994. Prediction risk and architecture selection for neural networks. *From Statistics to Neural Networks.* Springer.

MOOKIAH, M. R. K., ACHARYA, U. R., CHUA, C. K., LIM, C. M., NG, E. & LAUDE, A. 2013. Computer-aided diagnosis of diabetic retinopathy: A review. *Computers in biology and medicine,* 43**,** 2136-2155.

MORA, A. D., VIEIRA, P. M., MANIVANNAN, A. & FONSECA, J. M. 2011. Automated drusen detection in retinal images using analytical modelling algorithms. *Biomedical engineering online,* 10**,** 1.

NAGI, D., GOSDEN, C., WALTON, C., WINOCOUR, P., TURNER, B., WILLIAMS, R., JAMES, J. & HOLT, R. 2009. A national survey of the current state of screening services for diabetic retinopathy: ABCD–Diabetes UK survey of specialist diabetes services 2006. *Diabetic Medicine,* 26**,** 1301-1305.

NIEMEIJER, M., ABRÀMOFF, M. D. & VAN GINNEKEN, B. 2009. Fast detection of the optic disc and fovea in color fundus photographs. *Medical image analysis,* 13**,** 859-870.

NIEMEIJER, M., VAN GINNEKEN, B., RUSSELL, S. R., SUTTORP-SCHULTEN, M. S. & ABRAMOFF, M. D. 2007a. Automated detection and differentiation of drusen, exudates, and cotton-wool spots in digital color fundus photographs for diabetic retinopathy diagnosis. *Investigative ophthalmology & visual science,* 48**,** 2260-2267.

NIEMEIJER, M., VAN GINNEKEN, B., RUSSELL, S. R., SUTTORP-SCHULTEN, M. S. & ABRAMOFF, M. D. 2007b. Automated Detection and Differentiation of Drusen, Exudates, and Cotton-wool Spots in Digital Color Fundus Photographs for Early Diagnosis of Diabetic Retinopathy IOVS-06-0996 accepted version. *Investigative ophthalmology & visual science,* 48**,** 2260.

NOWOZIN, S., TSUDA, K., UNO, T., KUDO, T. & BAKIR, G. Weighted substructure mining for image analysis. Computer Vision and Pattern Recognition, 2007. CVPR'07. IEEE Conference on, 2007. IEEE, 1-8.

NUGROHO, H. A., OKTOEBERZA, K. W., ADJI, T. B. & NAJAMUDDIN, F. 2015. Detection of Exudates on Color Fundus Images using Texture Based Feature Extraction. *International Journal of Technology,* 6**,** 04.

OJALA, T., PIETIKÄINEN, M. & MÄENPÄÄ, T. 2002. Multiresolution gray-scale and rotation invariant texture classification with local binary patterns. *Pattern Analysis and Machine Intelligence, IEEE Transactions on,* 24**,** 971-987.

OMAR, M., HOSSAIN, A., ZHANG, L. & SHUM, H. An intelligent mobile-based automatic diagnostic system to identify retinal diseases using mathematical morphological operations. Software, Knowledge, Information Management and Applications (SKIMA), 2014 8th International Conference on, 2014. IEEE, 1-5.

OMAR, M., KHELIFI, F. & TAHIR, M. A. Detection and classification of retinal fundus images exudates using region based multiscale LBP texture approach. Control, Decision and Information Technologies (CoDIT), 2016 International Conference on, 2016. Malta: IEEE, 227-232.

OMAR, M., TAHIR, M. A. & KHELIFI, F. 2017. Multi-Label Learning Model for Improving Retinal Image Classification in Diabetic Retinopathy *Control, Decision and Information Technologies (CoDIT), 2017 International Conference on.* IEEE.

ORGANIZATION, W. H. 2004. Diabetes action now: an initiative of the World Health Organization and the International Diabetes Federation.

ORGANIZATION, W. H. 2016. Global report on diabetes: World Health Organization.

OSAREH, A. 2004. *Automated identification of diabetic retinal exudates and the optic disc.* University of Bristol.

OSAREH, A. 2006. Automated identification of diabetic retinal exudates in digital color images. *Color Image Processing: Methods and Applications.* CRC Press.

OSAREH, A., SHADGAR, B. & MARKHAM, R. 2009a. A computational-intelligence-based approach for detection of exudates in diabetic retinopathy images. *Information Technology in Biomedicine, IEEE Transactions on,* 13**,** 535-545.

OSAREH, A., SHADGAR, B. & MARKHAM, R. 2009b. A computational-intelligence-based approach for detection of exudates in diabetic retinopathy images. *IEEE Transactions on Information Technology in Biomedicine,* 13**,** 535-545.

PIETIKÄINEN, M., HADID, A., ZHAO, G. & AHONEN, T. 2011. Computer Vision Using Local Binary Patterns. *Computer Vision Using Local Binary Patterns.* Springer London.

RAPANTZIKOS, K., ZERVAKIS, M. & BALAS, K. 2003. Detection and segmentation of drusen deposits on human retina: Potential in the diagnosis of age-related macular degeneration. *Medical image analysis,* 7**,** 95-108.

RAVISHANKAR, S., JAIN, A. & MITTAL, A. Automated feature extraction for early detection of diabetic retinopathy in fundus images. Computer Vision and Pattern Recognition, 2009. CVPR 2009. IEEE Conference on, 2009. IEEE, 210-217.

REMA, M. & PRADEEPA, R. 2007. Diabetic retinopathy: an Indian perspective. *Indian journal of medical research,* 125**,** 297-310.

RICCI, E. & PERFETTI, R. 2007. Retinal blood vessel segmentation using line operators and support vector classification. *IEEE transactions on medical imaging,* 26**,** 1357-1365.

RUSS, J. C. 2016. *The image processing handbook*, CRC press.

SADEK, I., SIDIBÉ, D. & MERIAUDEAU, F. Automatic discrimination of color retinal images using the bag of words approach. Medical Imaging 2015: Computer-Aided Diagnosis, 2015. International Society for Optics and Photonics, 94141J.

SAINE, P. 1984. Errors in fundus photography. *J. Ophtalmic Photogr,* 7**,** 120-122.

SAINE, P. J. & TYLER, M. E. 2002. *Ophthalmic photography: retinal photography, angiography, and electronic imaging*, Butterworth-Heinemann Boston.

SÁNCHEZ, C. I., GARCÍA, M., MAYO, A., LÓPEZ, M. I. & HORNERO, R. 2009. Retinal image analysis based on mixture models to detect hard exudates. *Medical Image Analysis,* 13**,** 650-658.

SÁNCHEZ, C. I., HORNERO, R., LÓPEZ, M. I., ABOY, M., POZA, J. & ABÁSOLO, D. 2008. A novel automatic image processing algorithm for detection of hard exudates based on retinal image analysis. *Medical engineering & physics,* 30**,** 350-357.

SÁNCHEZ, C. I., NIEMEIJER, M., IŠGUM, I., DUMITRESCU, A., SUTTORP-SCHULTEN, M. S., ABRÀMOFF, M. D. & VAN GINNEKEN, B. 2012. Contextual computer-aided detection: Improving bright lesion detection in retinal images and coronary calcification identification in CT scans. *Medical image analysis,* 16**,** 50-62.

SÁNCHEZ, C. I., NIEMEIJER, M., SCHULTEN, M. S., ABRÀMOFF, M. & VAN GINNEKEN, B. Improving hard exudate detection in retinal images through a

combination of local and contextual information. Biomedical Imaging: From Nano to Macro, 2010 IEEE International Symposium on, 2010. IEEE, 5-8.

SEKHAR, S., AL-NUAIMY, W. & NANDI, A. K. Automated localisation of retinal optic disk using Hough transform. Biomedical Imaging: From Nano to Macro, 2008. ISBI 2008. 5th IEEE International Symposium on, 2008. IEEE, 1577-1580.

SHAH, C. A. 2008. Diabetic retinopathy: A comprehensive review. *Indian journal of medical sciences,* 62**,** 500.

SHAMSHIRBAND, S., PETKOVIĆ, D., AMINI, A., ANUAR, N. B., NIKOLIĆ, V., ĆOJBAŠIĆ, Ž., KIAH, M. L. M. & GANI, A. 2014a. Support vector regression methodology for wind turbine reaction torque prediction with power-split hydrostatic continuous variable transmission. *Energy,* 67**,** 623-630.

SHAMSHIRBAND, S., PETKOVIĆ, D., ĆOJBAŠIĆ, Ž., NIKOLIĆ, V., ANUAR, N. B., SHUIB, N. L. M., KIAH, M. L. M. & AKIB, S. 2014b. Adaptive neuro-fuzzy optimization of wind farm project net profit. *Energy Conversion and Management,* 80**,** 229-237.

SHAMSHIRBAND, S., PETKOVIĆ, D., SABOOHI, H., ANUAR, N. B., INAYAT, I., AKIB, S., ĆOJBAŠIĆ, Ž., NIKOLIĆ, V., KIAH, M. L. M. & GANI, A. 2014c. Wind turbine power coefficient estimation by soft computing methodologies: comparative study. *Energy Conversion and Management,* 81**,** 520-526.

SHAO, H., LI, G., LIU, G. & WANG, Y. 2013. Symptom selection for multi-label data of inquiry diagnosis in traditional Chinese medicine. *Science China Information Sciences,* 56**,** 1-13.

SHAW, J. E., SICREE, R. A. & ZIMMET, P. Z. 2010. Global estimates of the prevalence of diabetes for 2010 and 2030. *Diabetes research and clinical practice,* 87**,** 4-14.

SIDIBÉ, D., SADEK, I. & MÉRIAUDEAU, F. 2015. Discrimination of retinal images containing bright lesions using sparse coded features and SVM. *Computers in biology and medicine,* 62**,** 175-184.

SINGH, N. & TRIPATHI, R. C. 2010. Automated early detection of diabetic retinopathy using image analysis techniques. *International Journal of Computer Applications,* 8**,** 18-23.

SMITH, R. T., SOHRAB, M. A., PUMARIEGA, N., CHEN, Y., CHEN, J., LEE, N. & LAINE, A. 2010. Dynamic soft drusen remodelling in age-related macular degeneration. *British Journal of Ophthalmology,* 94**,** 1618-1623.

SMITH, S. W. 1997. The scientist and engineer's guide to digital signal processing.

SNELL, R. S. & LEMP, M. A. 2013. *Clinical anatomy of the eye*, John Wiley & Sons.

SOPHARAK, A., DAILEY, M. N., UYYANONVARA, B., BARMAN, S., WILLIAMSON, T., NWE, K. T. & MOE, Y. A. 2010. Machine learning approach to automatic exudate detection in retinal images from diabetic patients. *Journal of Modern optics,* 57**,** 124-135.

SOPHARAK, A., NEW, K. T., MOE, Y. A., DAILEY, M. N. & UYYANONVARA, B. Automatic exudate detection with a naive Bayes classifier. International Conference on Embedded Systems and Intelligent Technology, 2008. 139-142.

SOPHARAK, A., UYYANONVARA, B. & BARMAN, S. 2009. Automatic exudate detection from non-dilated diabetic retinopathy retinal images using fuzzy c-means clustering. *Sensors,* 9**,** 2148-2161.

SPAETH, G. L., DANESH-MEYER, H., GOLDBERG, I. & KAMPIK, A. 2011. *Ophthalmic surgery: principles and practice*, Elsevier Health Sciences.

SPOLAÔR, N., CHERMAN, E. A., MONARD, M. C. & LEE, H. D. 2013. A comparison of multi-label feature selection methods using the problem transformation approach. *Electronic Notes in Theoretical Computer Science,* 292**,** 135-151.

SRISUKKHAM, W., LEPCHA, P., HOSSAIN, M., ZHANG, L., JIANG, R. & LIM, H. A mobile enabled intelligent scheme to identify blood cancer for remote areas- cell membrane segmentation using marker controlled watershed segmentation phase. 7th international conference on Software, Knowledge, Intelligent Management and Applications, Thailand, 2013.

STEIN, H. A., STEIN, R. M. & FREEMAN, M. I. 2012. *The ophthalmic assistant*, Elsevier Health Sciences.

STRINGA, F., TSAMIS, E., PAPAYANNIS, A., CHWIEJCZAK, K., JALIL, A., BISWAS, S., AHMAD, H. & STANGA, P. E. 2017. segmented swept source optical coherence tomography angiography assessment of the perifoveal vasculature in patients with X-linked juvenile retinoschisis: a serial case report. *International medical case reports journal,* 10**,** 329.

SUN, H. & LUO, Y. 2009. Adaptive watershed segmentation of binary particle image. *Journal of microscopy,* 233**,** 326-330.

SUNDARESAN, V., RAM, K., SELVARAJ, K., JOSHI, N. & SIVAPRAKASAM, M. 2015. Adaptive super-candidate based approach for detection and classification of drusen on retinal fundus images.

SZABÓ, D., FIEDLER, O., SOMOGYI, A., SOMFAI, G. M., BÍRÓ, Z., ÖLVEDY, V., HARGITAI, Z. & NÉMETH, J. 2015. Telemedical diabetic retinopathy screening in Hungary: a pilot programme. *Journal of telemedicine and telecare***,** 1357633X15572712.

TAHIR, M. A., KITTLER, J. & BOURIDANE, A. 2012. Multilabel classification using heterogeneous ensemble of multi-label classifiers. *Pattern Recognition Letters,* 33**,** 513-523.

TAHIR, M. A., KITTLER, J. & BOURIDANE, A. 2016. Multi-label classification using stacked spectral kernel discriminant analysis. *Neurocomputing,* 171**,** 127-137.

TANG, Z., DAI, Y., ZHANG, X., HUANG, L. & YANG, F. 2013. Robust image hashing via colour vector angles and discrete wavelet transform. *IET Image Processing,* 8**,** 142-149.

TORTORA, G. J. & DERRICKSON, B. H. 2008. *Principles of anatomy and physiology*, John Wiley & Sons.

TURNBULL, D. & ELKAN, C. 2005. Fast recognition of musical genres using RBF networks. *Knowledge and Data Engineering, IEEE Transactions on,* 17**,** 580-584.

VAN GINNEKEN, B. & NOVAK, C. L. Computer-Aided Diagnosis. Proc. of SPIE Vol, 2012. 831501-1.

VAN GRINSVEN, M. J., CHAKRAVARTY, A., SIVASWAMY, J., THEELEN, T., VAN GINNEKEN, B. & SÁNCHEZ, C. I. A bag of words approach for discriminating between retinal images containing exudates or drusen. Biomedical Imaging (ISBI), 2013 IEEE 10th International Symposium on, 2013. IEEE, 1444-1447.

VAN GRINSVEN, M. J., THEELEN, T., WITKAMP, L., VAN DER HEIJDEN, J., VAN DE VEN, J. P., HOYNG, C. B., VAN GINNEKEN, B. & SÁNCHEZ, C. I. 2016. Automatic differentiation of color fundus images containing drusen or exudates using a contextual spatial pyramid approach. *Biomedical optics express,* 7**,** 709-725.

VIJ, K. & SINGH, Y. 2009. Enhancement of images using histogram processing techniques. *Int. J. Comp. Tech. Appl,* 2**,** 309-313.

VINCENT, L. Morphological grayscale reconstruction: definition, efficient algorithm and applications in image analysis. Computer Vision and Pattern Recognition, 1992. Proceedings CVPR'92., 1992 IEEE Computer Society Conference on, 1992. IEEE, 633-635.

VISSER, M., PAHOR, M., TYLAVSKY, F., KRITCHEVSKY, S. B., CAULEY, J. A., NEWMAN, A. B., BLUNT, B. A. & HARRIS, T. B. 2003. One-and two-year change in body composition as measured by DXA in a population-based cohort of older men and women. *Journal of applied physiology,* 94**,** 2368-2374.

WALTER, T., KLEIN, J.-C., MASSIN, P. & ERGINAY, A. 2002. A contribution of image processing to the diagnosis of diabetic retinopathy-detection of exudates in color fundus images of the human retina. *Medical Imaging, IEEE Transactions on,* 21**,** 1236-1243.

WELFER, D., SCHARCANSKI, J. & MARINHO, D. R. 2010. A coarse-to-fine strategy for automatically detecting exudates in color eye fundus images. *Computerized Medical Imaging and Graphics,* 34**,** 228-235.

WU, L., FERNANDEZ-LOAIZA, P., SAUMA, J., HERNANDEZ-BOGANTES, E. & MASIS, M. 2013. Classification of diabetic retinopathy and diabetic macular edema. *World J diabetes,* 4**,** 290-294.

YEN, G. G. & LEONG, W.-F. 2008. A sorting system for hierarchical grading of diabetic fundus images: A preliminary study. *IEEE Transactions on Information Technology in Biomedicine,* 12**,** 118-130.

YOUSSEF, D., SOLOUMA, N., EL-DIB, A., MABROUK, M. & YOUSSEF, A.-B. 2010. New feature-based detection of blood vessels and exudates in color fundus images. Image Processing Theory Tools and Applications (IPTA), 2010 2nd International Conference on, 2010. IEEE, 294-299.

ZHANG, G., SHU, X., LIANG, Z., LIANG, Y., CHEN, S. & YIN, J. Multi-instance learning for skin biopsy image features recognition. Bioinformatics and Biomedicine (BIBM), 2012 IEEE International Conference on, 2012. IEEE, 1-6.

ZHANG, J., MARSZAŁEK, M., LAZEBNIK, S. & SCHMID, C. 2007. Local features and kernels for classification of texture and object categories: A comprehensive study. *International journal of computer vision,* 73**,** 213-238.

ZHANG, M.-L. & ZHOU, Z.-H. 2007. ML-KNN: A lazy learning approach to multi-label learning. *Pattern recognition,* 40**,** 2038-2048.

ZHANG, M.-L. & ZHOU, Z.-H. 2014. A review on multi-label learning algorithms. *Knowledge and Data Engineering, IEEE Transactions on,* 26**,** 1819-1837.

ZHENG, Y., VANDERBEEK, B., DANIEL, E., STAMBOLIAN, D., MAGUIRE, M., BRAINARD, D. & GEE, J. An automated drusen detection system for classifying age-related macular degeneration with color fundus photographs. Biomedical Imaging (ISBI), 2013 IEEE 10th International Symposium on, 2013a. IEEE, 1448-1451.

ZHENG, Y., VANDERBEEK, B., DANIEL, E., STAMBOLIAN, D., MAGUIRE, M., BRAINARD, D. & GEE, J. An automated drusen detection system for classifying age-related macular degeneration with color fundus photographs. 2013 IEEE 10th International Symposium on Biomedical Imaging, 2013b. IEEE, 1448-1451.

APPENDICES

Appendix A

Evaluation of an intelligent mobile-based automatic diagnostic system to identify retinal diseases using mathematical morphological operations (Segmentation Part). The retina images in DR usually contain some unwanted features such as noisy, poorly contrasted and also the illumination is not uniform. These features are not considered as part of the hard exudates lesions and may affect the precision of the system's outputs. Techniques are required to enhance the contrast, sharpness and reducing noise of the fundus images to help human interpretation and as first step toward automatic analysis. Image processing techniques are very significant to overcome these problems. A block diagram of the retinal diagnosis system is shown in Fig 1.
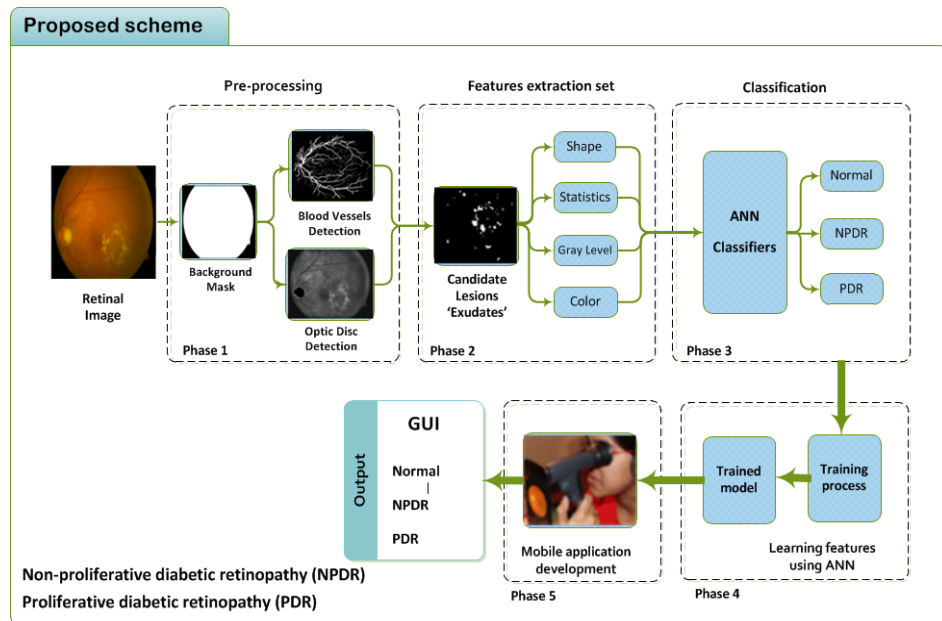
Figure A 1 Framework diagram of the retinal diagnosis system

A combination of morphological operations is used to detect the exudates in this proposed method. At this current stage of the work, the exudates are detected using mathematical morphology and reconstruction techniques. An important step in the extraction process is to remove prominent structures in the retina, such as blood vessels and the optic disc. This stage can be separated into three steps: pre-processing, optic disc removal and exudate extraction as metioned in litercture review chapter in more details.

Appendix B

Evaluation of automatic exudate detection using a combination of texture features, extracted from different local binary pattern (LBP) variants, with an artificial neural network (ANN), RBF-NN and ANN classifiers.

LBP Version	Sensitivity Mean	Specificity Mean	Accuracy Mean	PPV	TP	TN	FP	FN	AUC
ri-(8,1)	92.80%	93.81%	92.45%	93.81%	1212	920	80	94	0.98
ri-(8,2)	91.96%	92.67%	91.33%	92.67%	1201	905	95	105	0.97
ri-(8,3)	92.27%	93.70%	92.11%	93.70%	1205	919	81	101	0.97
ri-(8,4)	87.98%	91.26%	88.42%	91.26%	1149	890	110	157	0.95
ri-(8,5)	85.38%	88.56%	85.47%	88.56%	1115	856	144	191	0.92
ri-(8,6)	81.70%	85.57%	81.83%	85.57%	1067	820	180	239	0.89
ri-(8,7)	77.49%	84.47%	79.18%	84.47%	1012	814	186	294	0.86
ri-(8,8)	75.50%	81.09%	76.15%	81.09%	986	770	230	320	0.83
u2-(8,1)	93.42%	94.94%	93.45%	94.94%	1220	935	65	86	0.98
u2-(8,2)	92.11%	94.95%	92.76%	94.95%	1203	936	64	103	0.97
u2-(8,3)	90.66%	94.12%	91.50%	94.12%	1184	926	74	122	0.97
u2-(8,4)	87.75%	91.53%	88.46%	91.53%	1146	894	106	160	0.95
riu2-(8,1)	92.19%	94.43%	92.50%	94.43%	1204	929	71	102	0.97
riu2-(8,2)	90.74%	93.23%	91.02%	93.23%	1185	914	86	121	0.97
riu2-(8,3)	91.04%	93.84%	91.54%	93.84%	1189	922	78	117	0.97
riu2-(8,4)	85.99%	90.42%	86.90%	90.42%	1123	881	119	183	0.94
riu2-(16,1)	93.26%	94.27%	92.97%	94.27%	1218	926	74	88	0.98
riu2-(16,2)	91.50%	94.47%	92.15%	94.47%	1195	930	70	111	0.97
riu2-(16,1-2)	93.57%	96.83%	94.62%	96.83%	1222	960	40	84	0.98
riu2-(16,1-2)+u2-(8,1)	93.34%	97.13%	94.67%	97.13%	1219	964	36	87	0.98

Figure B.1 LBP texture features with different versions using RBF-NN classifier

LBP Version	Sensitivity Mean	Specificity Mean	Accuracy Mean	PPV	TP	TN	FP	FN	AUC
ri-(8,1)	89.74%	89.88%	88.46%	89.88%	1172	868	132	134	0.93
ri-(8,2)	89.28%	88.80%	87.55%	88.80%	1166	853	147	140	0.93
ri-(8,3)	90.43%	90.36%	89.12%	90.36%	1181	874	126	125	0.92
ri-(8,4)	86.91%	85.66%	84.35%	85.66%	1135	810	190	171	0.90
ri-(8,5)	80.70%	82.67%	79.49%	82.67%	1054	779	221	252	0.86
ri-(8,6)	78.10%	79.56%	76.24%	79.56%	1020	738	262	286	0.83
ri-(8,7)	74.66%	77.69%	73.50%	77.69%	975	720	280	331	0.80
ri-(8,8)	73.51%	76.92%	72.51%	76.92%	960	712	288	346	0.78
u2-(8,1)	91.58%	90.54%	89.81%	90.54%	1196	875	125	110	0.94
u2-(8,2)	90.05%	90.05%	88.73%	90.05%	1176	870	130	130	0.94
u2-(8,3)	88.82%	89.03%	87.47%	89.03%	1160	857	143	146	0.92
u2-(8,4)	86.37%	87.17%	85.08%	87.17%	1128	834	166	178	0.91
riu2-(8,1)	90.20%	93.12%	90.68%	93.12%	1178	913	87	128	0.95
riu2-(8,2)	88.67%	92.12%	89.29%	92.12%	1158	901	99	148	0.95
riu2-(8,3)	89.59%	92.05%	89.72%	92.05%	1170	899	101	136	0.94
riu2-(8,4)	83.46%	89.49%	85.08%	89.49%	1090	872	128	216	0.91
riu2-(16,1)	91.12%	90.84%	89.77%	90.84%	1190	880	120	116	0.95
riu2-(16,2)	90.81%	91.94%	90.29%	91.94%	1186	896	104	120	0.95
riu2-(16,1-2)	93.34%	92.42%	91.89%	92.42%	1219	900	100	87	0.96
riu2-(16,1-2)+u2-(8,1)	93.87%	92.81%	92.41%	92.81%	1226	905	95	80	0.96

Figure B.2 LBP texture features using ANN classifier

119

LBP Version	Sensitivity Mean	Specificity Mean	Accuracy Mean	PPV	TP	TN	FP	FN	AUC
ri-(8,1)	89.74%	89.88%	88.46%	89.88%	1172	868	132	134	0.93
ri-(8,2)	89.28%	88.80%	87.55%	88.80%	1166	853	147	140	0.93
ri-(8,3)	90.43%	90.36%	89.12%	90.36%	1181	874	126	125	0.92
ri-(8,4)	86.91%	85.66%	84.35%	85.66%	1135	810	190	171	0.90
ri-(8,5)	80.70%	82.67%	79.49%	82.67%	1054	779	221	252	0.86
ri-(8,6)	78.10%	79.56%	76.24%	79.56%	1020	738	262	286	0.83
ri-(8,7)	74.66%	77.69%	73.50%	77.69%	975	720	280	331	0.80
ri-(8,8)	73.51%	76.92%	72.51%	76.92%	960	712	288	346	0.78
u2-(8,1)	91.58%	90.54%	89.81%	90.54%	1196	875	125	110	0.94
u2-(8,2)	90.05%	90.05%	88.73%	90.05%	1176	870	130	130	0.94
u2-(8,3)	88.82%	89.03%	87.47%	89.03%	1160	857	143	146	0.92
u2-(8,4)	86.37%	87.17%	85.08%	87.17%	1128	834	166	178	0.91
riu2-(8,1)	**90.20%**	**93.12%**	**90.68%**	**93.12%**	**1178**	**913**	**87**	**128**	**0.95**
riu2-(8,2)	88.67%	92.12%	89.29%	92.12%	1158	901	99	148	0.95
riu2-(8,3)	89.59%	92.05%	89.72%	92.05%	1170	899	101	136	0.94
riu2-(8,4)	83.46%	89.49%	85.08%	89.49%	1090	872	128	216	0.91
riu2-(16,1)	91.12%	90.84%	89.77%	90.84%	1190	880	120	116	0.95
riu2-(16,2)	90.81%	91.94%	90.29%	91.94%	1186	896	104	120	0.95
riu2-(16,1-2)	93.34%	92.42%	91.89%	92.42%	1219	900	100	87	0.96
riu2-(16,1-2)+u2-(8,1)	**93.87%**	**92.81%**	**92.41%**	**92.81%**	**1226**	**905**	**95**	**80**	**0.96**

Figure B.3 LBP texture features using ANN classifier

Experiments on retinal image patches:

1. Block extraction:

The total of 30 RGB images is divided to two groups to be used in our experiments and validation as training phase:

1- 20 images are abnormal and 10 images are normal (DIARETDB0 and DIARETDB1 datasets).

2- The 30 images are used (DIARETDB0 and DIARETDB1 datasets) and 2970 block of sizes 128×128 are extracted after every image is divided into 99 blocks.

The total 20 of abnormal image are diagnosed manually for different stages of Diabetic Retinopathy (DR) disease based on the database which analysed by experts as whole image. The blocks are labelled manually as follows:

N: Normal

A: Abnormal (Red Small Dots)

B: Abnormal (Haemorrhage)

C: Abnormal (Exudate)

2. Texture features extraction:

Texture features of blocks are extracted by using Local Binary Pattern (LBP) and the Segmentation-based Fractal Texture Analysis (SFTA) as texture features descriptors of total 71 features. The feature set of texture features are computed for each block of an image. The texture features set of blocks are used for clustering and classification stage as feature vector.

3. Features selection:

In order to get an important texture features, the Decision Tree (DT) and ReliefF function are used. Before they are used the ksdensity function has also used for testing where the feature has good scale.

4. Block reduction:

In order to remove the image borders as considered of noises, the k-means clustering technique is used. The k-means divided all blocks into 10 groups (k=10). The most of all blocks borders signed into two groups and the total of blocks borders are 923 among 2970 normal and abnormal blocks. The dark blocks are also labelled for both normal and abnormal blocks which are 613 blocks and the rest of the dataset is considered as light (1434 block). The blocks have reduced from 2970 blocks to 1434 block (manually).

5. Thresholding techniques:

In order to isolate all borders and dark blocks, the general tools of thresholding technique (if statement based on specific features) are used to discard them as follow:

Min and max for each feature is compared and matched between two features of dark and light blocks based on range distribution. Feature 14 (F14) found the best result to distinguish between the borders blocks and other blocks. The second method, DT (CART) is used for best feature.

The second threshold is used to distinguish between the dark blocks and light blocks using same technique and different features.

Ksdensity function is used to estimate the probability density between two features of dark and light blocks.
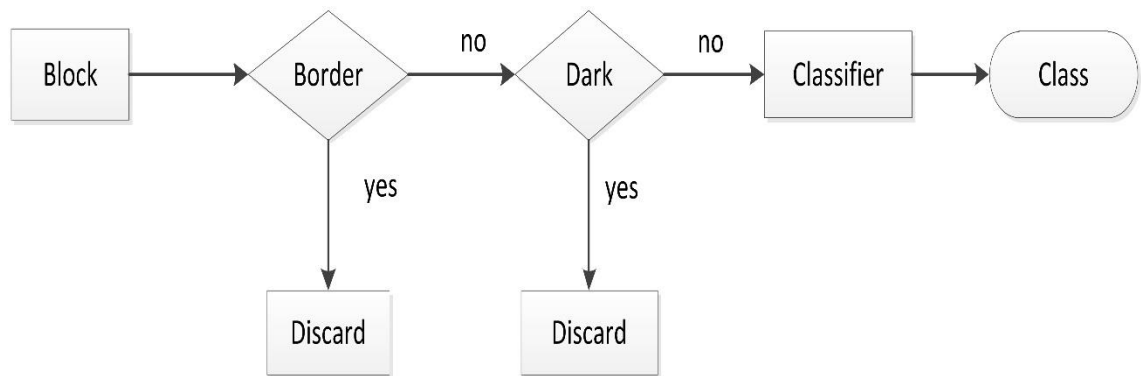
Figure B.4 Block diagram for thresholding
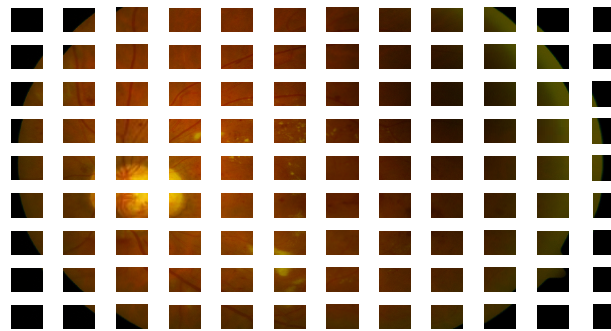
Figure B.5 Block (patch) extraction
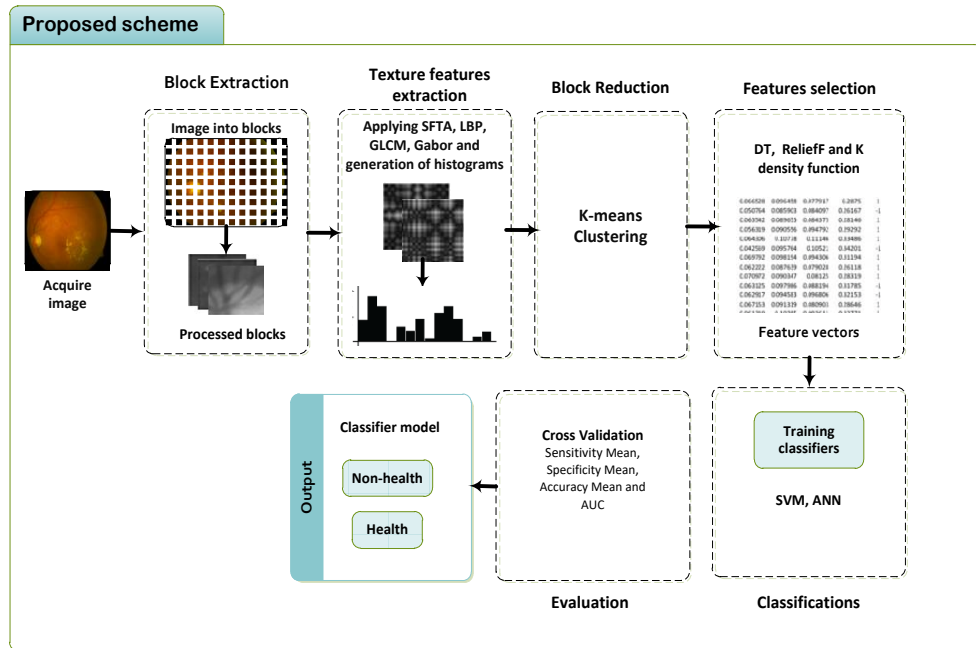
Figure B.6 Proposed framework model for training and classification of from DR diagnosis

6. Classification:

For this stage we classified our data to two classes, abnormal and normal blocks. The Neural Network and Support Vector Machine (SVM) with different function are used.

7. System evaluation:

The Cross Validation method is used to test all dataset and other measurements tools (Sensitivity Mean, Specificity Mean, Accuracy Mean and AUC).

Appendix C

List of experiments

Multi-label learning model for improving the classification of exudate lesions.

Table C.1 Multi-labels information for DME diagnosis and patient's age and along with the classification of normal / abnormal regions, other information needs to be simultaneously classified such as patient's age, ethnicity, race and diabetic's type etc.

ImageName	AGE			Multi4 label						PatientRace		Image Quility		
	DoB	Age	Label	DME	Age	DA	P_Gender	Label	Label			QualityValue	L_Q	D_Type
(00000003).jpg	12/28/1955	61	OLD	A	O	AO	F	FA	A	CAUCASIAN	CA	0.3293741	C	TYPE II
(00000052).jpg	04/12/1942	74	OLD	A	O	AO	F	FA	A	AFRICAN	AF	0.4071071	C	TYPE II
(00000053).jpg	04/12/1942	74	OLD	A	O	AO	F	FA	A	AFRICAN	AF	0.6259186	B	TYPE II
(00000054).jpg	12/29/1954	62	OLD	A	O	AO	F	FA	A	HISPANIC	HI	0.7528505	B	TYPE II
(00000055).jpg	12/29/1954	62	OLD	A	O	AO	F	FA	A	HISPANIC	HI	0.4627067	C	TYPE II
(00000060).jpg	08/05/1946	70	OLD	N	O	NO	F	FN	B	AFRICAN	AF	0.8834876	A	TYPE II
(00000061).jpg	08/05/1946	70	OLD	N	O	NO	F	FN	B	AFRICAN	AF	0.6788735	B	TYPE II
(00000074).jpg	04/11/1961	55	MED	N	M	NM	F	FN	B	AFRICAN	AF	0.5460845	B	TYPE II
(00000094).jpg	01/01/2007	9	YOUNG	N	Y	NY	UNKNOWN	FN	B	UNKNOWN	UN	0.8764083	A	UNKNOWN
(00000101).jpg	12/07/1952	64	OLD	A	O	AO	F	FA	A	AFRICAN	AF	0.3449203	C	TYPE II
(00000105).jpg	8/31/1947	69	OLD	A	O	AO	F	FA	A	AFRICAN	AF	0.08960439	C	TYPE II
(00000120).jpg	12/07/1952	64	OLD	N	O	NO	F	FN	B	AFRICAN	AF	0.3559083	C	TYPE II
(00000122).jpg	7/23/1959	57	MED	N	M	NM	M	MN	D	AFRICAN	AF	0.5	B	TYPE II
(00000128).jpg	5/24/1964	52	MED	N	M	NM	M	MN	D	AFRICAN	AF	0.8342063	A	TYPE II
(00000131).jpg	6/22/1949	67	OLD	N	O	NO	F	FN	B	AFRICAN	AF	0.4534312	C	TYPE II
(00000137).jpg	1/14/1968	48	MED	N	M	NM	F	FN	B	AFRICAN	AF	0.8863549	A	TYPE II
(00000138).jpg	1/14/1968	48	MED	N	M	NM	F	FN	B	AFRICAN	AF	0.8301352	A	TYPE II
(00000139).jpg	10/27/1951	65	OLD	A	O	AO	F	FA	A	AFRICAN	AF	0.8482556	A	TYPE II
(00000140).jpg	10/27/1951	65	OLD	N	O	NO	F	FN	B	AFRICAN	AF	0.7195595	B	TYPE II
(00000162).jpg	9/23/1948	68	OLD	N	O	NO	F	FN	B	AFRICAN	AF	0.8347169	A	TYPE II
(00000166).jpg	1/26/1954	62	OLD	N	O	NO	F	FN	B	AFRICAN	AF	0.6340579	B	TYPE II
(00000167).jpg	1/26/1954	62	OLD	A	O	AO	F	FA	A	AFRICAN	AF	0.6081741	B	TYPE II
(00000168).jpg	10/21/1954	62	OLD	N	O	NO	F	FN	B	CAUCASIAN	CA	0.839159	A	TYPE II
(00000173).jpg	10/09/1952	64	OLD	N	O	NO	M	MN	D	CAUCASIAN	CA	0.591688	B	TYPE II
(00000174).jpg	8/16/1962	54	MED	N	M	NM	F	FN	B	CAUCASIAN	CA	0.9203732	A	TYPE II
(00000175).jpg	8/16/1962	54	MED	N	M	NM	F	FN	B	CAUCASIAN	CA	0.8652307	A	TYPE II
(00000180).jpg	7/25/1951	65	OLD	N	O	NO	F	FN	B	AFRICAN	AF	0.8495176	A	TYPE II
(00000181).jpg	7/25/1951	65	OLD	N	O	NO	F	FN	B	AFRICAN	AF	0.826749	A	TYPE II
(00000182).jpg	6/18/1976	40	YOUNG	N	Y	NY	F	FN	B	CAUCASIAN	CA	0.9045187	A	TYPE II
(00000187).jpg	09/07/1951	65	OLD	N	O	NO	F	FN	B	AFRICAN	AF	0.8725173	A	TYPE II
(00000188).jpg	03/12/1966	50	MED	N	M	NM	M	MN	D	AFRICAN	AF	0.9280866	A	TYPE II
(00000192).jpg	04/05/1961	55	MED	A	M	AM	F	FA	A	AFRICAN	AF	0.3854902	C	TYPE II
(00000197).jpg	8/23/1963	53	MED	N	M	NM	F	FN	B	AFRICAN	AF	0.8494051	A	TYPE II
(00000198).jpg	8/23/1963	53	MED	N	M	NM	F	FN	B	AFRICAN	AF	0.8443481	A	TYPE II
(00000199).jpg	12/17/1942	74	OLD	N	O	NO	F	FN	B	AFRICAN	AF	0.5090251	B	TYPE II
(00000200).jpg	12/17/1942	74	OLD	N	O	NO	F	FN	B	AFRICAN	AF	0.8237622	A	TYPE II
(00000203).jpg	3/27/1955	61	OLD	N	O	NO	F	FN	B	AFRICAN	AF	0.7090696	B	TYPE II
(00000205).jpg	9/18/1960	56	MED	N	M	NM	F	FN	B	CAUCASIAN	CA	0.8796144	A	TYPE II
(00000217).jpg	11/20/1946	70	OLD	A	O	AO	F	FA	A	AFRICAN	AF	0.5	B	TYPE II
(00000218).jpg	11/20/1946	70	OLD	A	O	AO	F	FA	A	AFRICAN	AF	0.3476995	C	TYPE II
(00000230).jpg	1/16/1960	56	MED	A	M	AM	F	FA	A	AFRICAN	AF	0.9897866	A	TYPE II
(00000235).jpg	7/23/1947	69	OLD	A	O	AO	F	FA	A	UNKNOWN	UN	0.6939882	B	UNKNOWN
(00000256).jpg	05/08/1959	57	MED	A	M	AM	F	FA	A	UNKNOWN	UN	0.9792975	A	UNKNOWN
(00000257).jpg	05/08/1959	57	MED	A	M	AM	F	FA	A	UNKNOWN	UN	0.9804057	A	UNKNOWN
(00000274).jpg	1/15/1949	67	OLD	A	O	AO	F	FA	A	AFRICAN	AF	0.7830119	B	TYPE II
(00000294).jpg	07/06/1958	58	MED	A	M	AM	F	FA	A	AFRICAN	AF	0.9879127	A	TYPE II
(00000296).jpg	9/28/1953	63	OLD	A	O	AO	F	FA	A	AFRICAN	AF	0.9784871	A	TYPE II
(00000347).jpg	12/30/1971	45	MED	A	M	AM	M	MA	C	AFRICAN	AF	0.9980842	A	TYPE II
(00000348).jpg	12/30/1971	45	MED	A	M	AM	M	MA	C	AFRICAN	AF	0.9162074	A	TYPE II
(00000419).jpg	09/07/1945	71	OLD	A	O	AO	F	FA	A	AFRICAN	AF	0.9729797	A	TYPE II
(00000444).jpg	5/24/1963	53	MED	A	M	AM	F	FA	A	AFRICAN	AF	0.9493758	A	TYPE II
(00000544).jpg	4/27/1988	28	YOUNG	A	Y	AY	M	MA	C	AFRICAN	AF	0.9956906	A	TYPE I
(00000552).jpg	10/05/1945	71	OLD	A	O	AO	F	FA	A	AFRICAN	AF	0.7040951	B	TYPE II
(00000553).jpg	10/05/1945	71	OLD	A	O	AO	F	FA	A	AFRICAN	AF	0.8003945	A	TYPE II

Table C.2 Multi-labels information for DME diagnosis and patient's age and along with the classification of normal / abnormal regions, other information needs to be simultaneously classified such as patient's age, ethnicity, race and diabetic's type etc.

Filename	Date	Age					Sex			Ethnicity		Score		Type
(00000566).jpg	6/21/1966	50	MED	A	M	AM	F	FA	A	AFRICAN	AF	0.9766268	A	TYPE II
(00000567).jpg	6/21/1966	50	MED	A	M	AM	F	FA	A	AFRICAN	AF	0.9887199	A	TYPE II
(00000582).jpg	09/06/1947	69	OLD	A	O	AO	M	MA	C	AFRICAN	AF	0.9824499	A	TYPE II
(00000583).jpg	09/06/1947	69	OLD	A	O	AO	M	MA	C	AFRICAN	AF	0.9774827	A	TYPE II
(00000584).jpg	09/06/1955	61	OLD	A	O	AO	F	FA	A	AFRICAN	AF	0.990162	A	TYPE II
(00000585).jpg	09/06/1955	61	OLD	A	O	AO	F	FA	A	AFRICAN	AF	0.9730111	A	TYPE II
(00000588).jpg	5/16/1966	50	MED	A	M	AM	M	MA	C	AFRICAN	AF	0.9730111	A	TYPE II
(00000589).jpg	5/16/1966	50	MED	A	M	AM	M	MA	C	AFRICAN	AF	0.9043152	A	TYPE II
(00000611).jpg	07/12/1951	65	OLD	A	O	AO	M	MA	C	AFRICAN	AF	0.903686	A	TYPE II
(00000612).jpg	11/20/1955	61	OLD	A	O	AO	F	FA	A	AFRICAN	AF	0.6800889	B	TYPE II
(00000613).jpg	11/20/1955	61	OLD	A	O	AO	F	FA	A	AFRICAN	AF	0.9216646	A	TYPE II
(00000641).jpg	02/04/1954	62	OLD	A	O	AO	F	FA	A	CAUCASIAN	CA	0.9433835	A	TYPE II
(00000669).jpg	08/08/1956	60	MED	A	M	AM	F	FA	A	AFRICAN	AF	0.985441	A	TYPE II
(00000670).jpg	08/08/1956	60	MED	A	M	AM	F	FA	A	AFRICAN	AF	0.9542806	A	TYPE II
(00000686).jpg	03/04/1960	56	MED	A	M	AM	F	FA	A	AFRICAN	AF	0.9818598	A	TYPE II
(00000736).jpg	01/01/1951	65	OLD	A	O	AO	F	FA	A	HISPANIC	HI	0.7821038	B	TYPE II
(00000753).jpg	9/19/1962	54	MED	A	M	AM	F	FA	A	CAUCASIAN	CA	0.9936741	A	TYPE II
(00000754).jpg	9/19/1962	54	MED	A	M	AM	F	FA	A	CAUCASIAN	CA	0.9078147	A	TYPE II
(00000799).jpg	2/13/1977	39	YOUNG	A	Y	AY	M	MA	C	AFRICAN	AF	0.9983922	A	TYPE II
(00000800).jpg	2/13/1977	39	YOUNG	A	Y	AY	M	MA	C	AFRICAN	AF	0.9951381	A	TYPE II
(00000849).jpg	5/22/1957	59	MED	A	M	AM	M	MA	C	AFRICAN	AF	0.9617285	A	TYPE II
(00000850).jpg	5/22/1957	59	MED	A	M	AM	M	MA	C	AFRICAN	AF	0.7732166	B	TYPE II
(00000941).jpg	10/24/1944	72	OLD	A	O	AO	F	FA	A	AFRICAN	AF	0.9875435	A	TYPE II
(00001044).jpg	02/02/1948	68	OLD	A	O	AO	M	MA	C	CAUCASIAN	CA	0.9521276	A	TYPE II
(00001058).jpg	07/06/1950	66	OLD	A	O	AO	F	FA	A	AFRICAN	AF	0.9979925	A	TYPE II
(00001107).jpg	06/09/1963	53	MED	A	M	AM	M	MA	C	AFRICAN	AF	0.872302	A	TYPE II
(00001187).jpg	11/17/1955	61	OLD	N	O	NO	F	FN	B	AFRICAN	AF	0.9686624	C	UNKNOWN
(00001188).jpg	4/18/1957	59	MED	A	M	AM	F	FA	A	CAUCASIAN	CA	0.3828208	C	UNKNOWN
(00001189).jpg	4/18/1957	59	MED	A	M	AM	F	FA	A	CAUCASIAN	CA	0.5915843	B	UNKNOWN
23_(2308).dcm.jpg	10/14/1932	84	OLD	N	O	NO	F	FN	B	CAUCASIAN	CA	0.9884302	A	TYPE II
87_(2034).dcm.jpg	08/11/1958	58	MED	N	M	NM	F	FN	B	AFRICAN	AF	0.8745093	A	TYPE II
9140_(1754).dcm.jpg	02/09/1948	68	OLD	N	O	NO	F	FN	B	CAUCASIAN	CA	0.9969707	A	TYPE II
15507_(1635).dcm.jpg	01/02/1948	68	OLD	N	O	NO	F	FN	B	AFRICAN	AF	0.9486094	A	TYPE II
16878_(1620).dcm.jpg	7/17/1943	73	OLD	N	O	NO	F	FN	B	AFRICAN	AF	0.9533157	A	TYPE II
17376_(2614).dcm.jpg	08/11/1964	52	MED	N	M	NM	F	FN	B	AFRICAN	AF	0.9103783	A	TYPE II
19486_(2380).dcm.jpg	7/18/1950	66	OLD	N	O	NO	M	MN	D	CAUCASIAN	CA	0.9664872	A	TYPE II
22410_(1616).dcm.jpg	10/26/1951	65	OLD	N	O	NO	F	FN	B	AFRICAN	AF	0.9472724	A	TYPE II
23135_(1728).dcm.jpg	3/26/1962	54	MED	N	M	NM	M	MN	D	CAUCASIAN	CA	0.9972376	A	TYPE II
24842_(1939).dcm.jpg	10/08/1960	56	MED	N	M	NM	M	MN	D	HISPANIC	HI	0.9955804	A	TYPE II
25025_(1972).dcm.jpg	06/11/1962	54	MED	N	M	NM	F	FN	B	AFRICAN	AF	0.9916813	A	TYPE II
26168_(1839).dcm.jpg	10/10/1962	54	MED	N	M	NM	F	FN	B	CAUCASIAN	CA	0.9925817	A	TYPE II
26866_(1732).dcm.jpg	08/04/1933	83	OLD	N	O	NO	M	MN	D	AFRICAN	AF	0.52598	B	TYPE II
28076_(2084).dcm.jpg	08/09/1954	62	OLD	N	O	NO	M	MN	D	HISPANIC	HI	0.9983478	A	TYPE II
30140_(2702).dcm.jpg	7/15/1967	49	MED	N	M	NM	M	MN	D	HISPANIC	HI	0.9961552	A	TYPE II
30268_(1804).dcm.jpg	9/18/1948	68	OLD	N	O	NO	F	FN	B	CAUCASIAN	CA	0.9296027	A	TYPE II
30302_(2442).dcm.jpg	8/27/1969	47	MED	N	M	NM	F	FN	B	HISPANIC	HI	0.996019	A	TYPE II
34285_(2724).dcm.jpg	10/07/1943	73	OLD	N	O	NO	F	FN	B	AFRICAN	AF	0.9864125	A	TYPE II
35077_(1673).dcm.jpg	7/28/1949	67	OLD	N	O	NO	F	FN	B	AFRICAN	AF	0.9983461	A	TYPE II
35486_(1708).dcm.jpg	8/28/1954	62	OLD	N	O	NO	F	FN	B	AFRICAN	AF	0.9563344	A	TYPE II
35565_(2747).dcm.jpg	10/23/1958	58	MED	N	M	NM	F	FN	B	AFRICAN	AF	0.9828484	A	TYPE II
35716_(1884).dcm.jpg	03/04/1947	69	OLD	N	O	NO	F	FN	B	CAUCASIAN	CA	0.9808916	A	TYPE II
37576_(894).dcm.jpg	10/09/1952	64	OLD	N	O	NO	M	MN	D	CAUCASIAN	CA	0.7838046	B	TYPE II
38178_(2295).dcm.jpg	06/05/1973	43	MED	N	M	NM	M	MN	D	AFRICAN	AF	0.9908862	A	TYPE II
38929_(1816).dcm.jpg	8/30/1967	49	MED	N	M	NM	UNKNOWN	FN	B	HISPANIC	HI	0.8871614	A	TYPE II
41090_(1916).dcm.jpg	10/01/1956	60	MED	N	M	NM	F	FN	B	AFRICAN	AF	0.9881037	A	TYPE II
41472_(2437).dcm.jpg	1/16/1956	60	MED	N	M	NM	M	MN	D	AFRICAN	AF	0.9918954	A	TYPE II

Confusion Matrix

| Output Class	Target Class 1	Target Class 2	
1	**209** 21.7%	**141** 14.6%	59.7% 40.3%
2	**148** 15.3%	**467** 48.4%	75.9% 24.1%
	58.5% 41.5%	76.8% 23.2%	**70.1%** **29.9%**

125
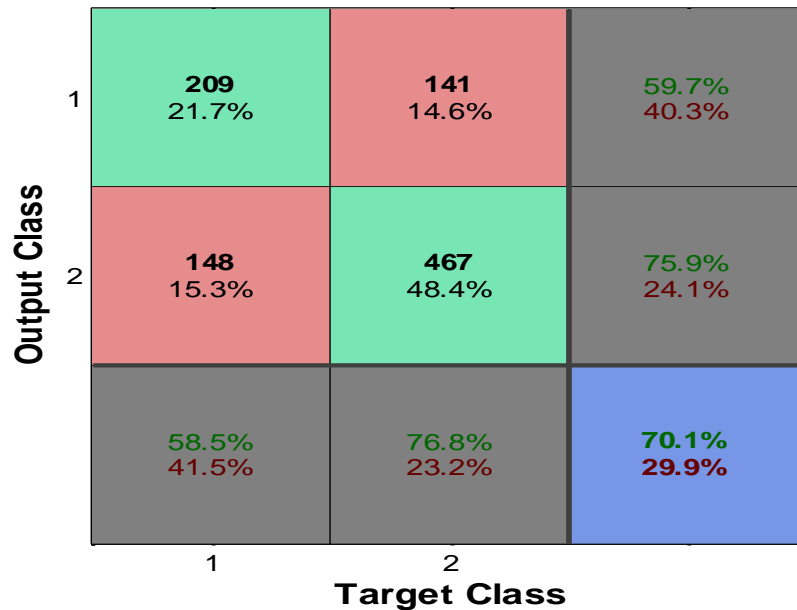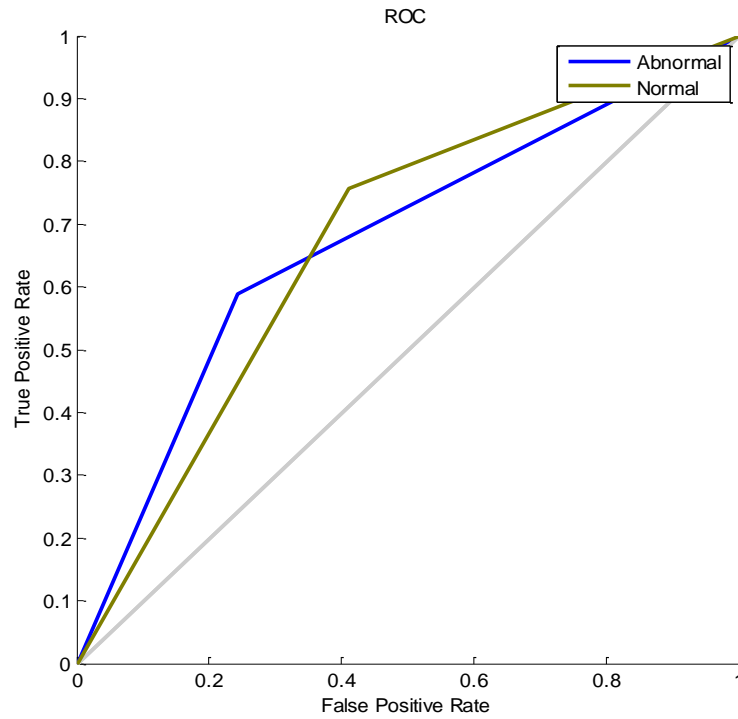
Figure C1 104 samples for training 104 (88+16) & testing 26 (22+4) and results of k-NN classifier

Table C.3 104 samples for training 104 (88+16) & testing 26 (22+4) and results of k-NN classifier

no	training	testing	neurons	Error
1	96.2	84.6	14	1.3888
2	95.2	84.6	12	0
3	94.2	84.6	10	1.3888
4	97.1	80.8	16	2.3888
5	93.3	80.8	12	1.3888

Figure D.2 104 samples with 12 neurons:
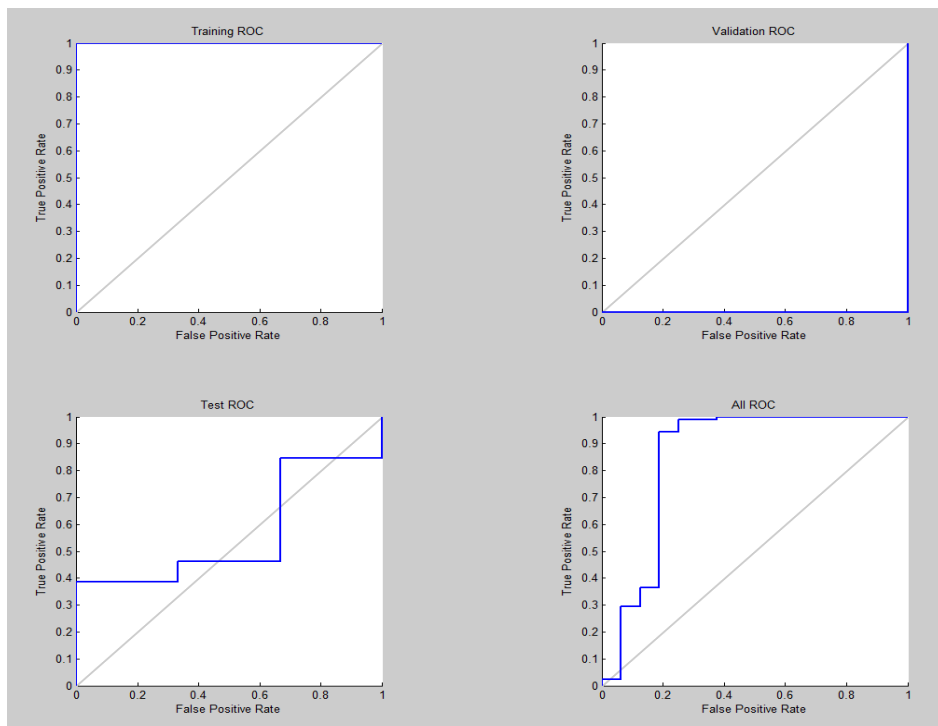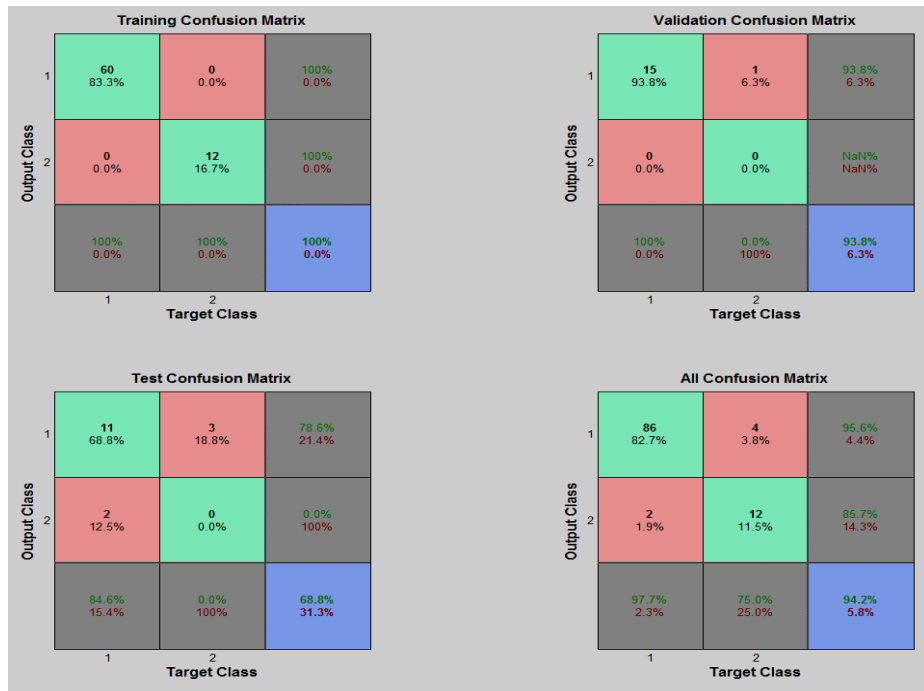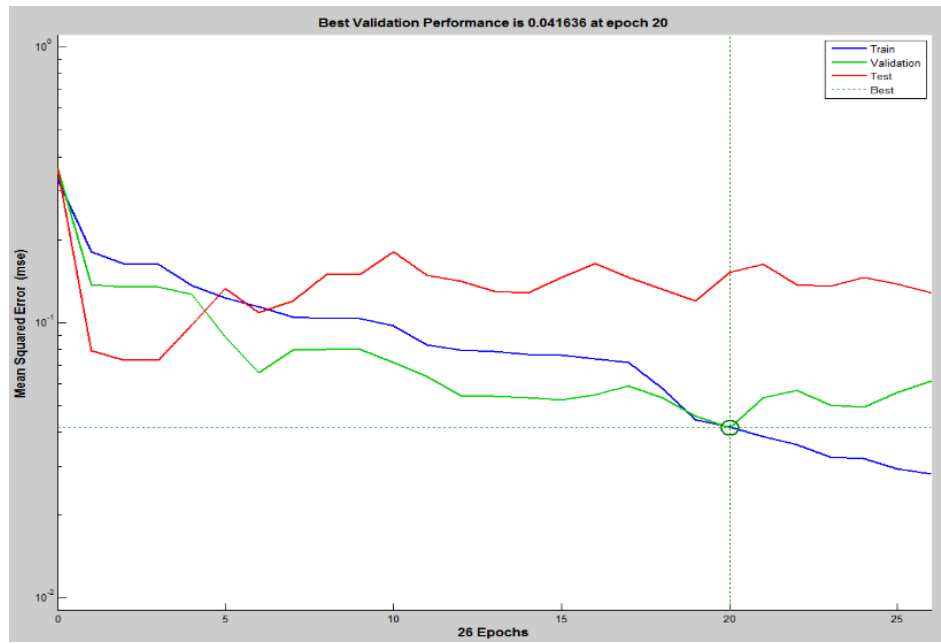
Figure C.2 104 samples with 10 neurons:

Appendix D

Publications

1. OMAR, M., KHELIFI, F. & TAHIR, M. A. Detection and classification of retinal fundus images exudates using region based multiscale LBP texture approach. Control, Decision and Information Technologies (CoDIT), 2016 International Conference on, 2016. Malta: IEEE, 227-232.

2. OMAR, M., TAHIR, M. A. & KHELIFI, F. 2017. Multi-Label Learning Model for Improving Retinal Image Classification in Diabetic Retinopathy Control, Decision and Information Technologies (CoDIT), 2017 International Conference on. IEEE.

3. OMAR, M., KHELIFI, F. & TAHIR, M. A. Exudate and Drusen Detection in Retinal Images Using Bagged Colour Vector Angles and Local Binary Patterns (Submitted to Arab Economic and Business Journal - Elsevier).